TECHNISCHE UNIVERSITÄT MÜNCHEN
Physik-Department E11

Ultrafast Spin Dynamics in Semiconductors: A Comparative Optical Analysis of Direct and Indirect Materials

Dipl.-Phys. Univ. Christine Hautmann

Vollständiger Abdruck der von der Fakultät für Physik
der Technischen Universität München zur Erlangung des akademischen Grades eines
Doktors der Naturwissenschaften
genehmigten Dissertation.

Vorsitzender: Univ.-Prof. Dr. M. Zacharias
Prüfer der Dissertation:
1. Univ.-Prof. Dr. Dr. h. c. A. Laubereau, em.
2. apl. Prof. Dr. M. S. Brandt

Die Dissertation wurde am 19.07.2012 bei der
Technischen Universität München eingereicht und durch die
Fakultät für Physik am 07.08.2012 angenommen.

Abstract

Magneto-optical pump-probe spectroscopy is a convenient and widely-used method to investigate electron spin dynamics in direct-gap semiconductors. The primary concern of the present work is to examine carrier spin dynamics in an indirect-gap semiconductor with this method, where the material of choice is germanium. An important aspect associated with such an investigation is the comparison of spin dynamics in direct- and indirect-gap bulk semiconductors. To this end, electron spin dynamics in gallium antimonide and indium gallium arsenide is addressed as a first point. The investigations support the present good understanding of spin dynamics of free conduction band electrons in direct-gap semiconductors, in particular, the decay of spin coherence via the D'yakonov-Perel' mechanism. In this context, it is specifically worth mentioning that the impact of spin-orbit coupling on electron spin coherence becomes evident when comparing gallium antimonide and indium gallium arsenide. Moreover, the present selection of direct-gap semiconductors is suited to detect electron spin dynamics in the telecom wavelength band around $1.55\,\mu$m. This wavelength range is interesting from the point of view of device applications, however, it has not been addressed via magneto-optical pump-probe spectroscopy so far. The ultrafast magneto-optical examinations of carrier spin dynamics in germanium address fundamental questions on orientation and readout of carrier spins via indirect optical transitions. Furthermore, the data represent the first comprehensive investigation of the dynamics of photogenerated electron and hole spin polarisations in an indirect-gap semiconductor, where the key results are the following. Compared to literature values on hole spin coherence times in direct-gap semiconductors, hole spin coherence in germanium is long-lived. In addition, the multivalley structure of the indirect conduction band minimum is mapped in the coherent precession of photogenerated electron spins in external magnetic fields. The investigations allow to extract the Landé tensor in the indirect conduction band minima of germanium, and indicate that the Elliott-Yafet mechanism impacts the decay of electron spin coherence.

Kurzfassung

Die Messmethode der magneto-optischen Anrege-Abfrage-Spektroskopie wird verbreitet genutzt, um die Dynamik von Elektronenspins in Halbleitern mit direkter Bandlücke zu untersuchen. Hauptanliegen der vorliegenden Arbeit ist es, diese Messmethode auf Germanium – also einen Halbleiter mit indirekter Bandlücke – anzuwenden. Interessant ist in diesem Zusammenhang auch ein Vergleich der Spindynamik in Volumenhalbleitern mit direkter und indirekter Bandlücke. Dazu werden zunächst Gallium-Antimonid und Indium-Gallium-Arsenid untersucht. Diese Untersuchungen bestätigen das heutige gute Verständnis der Dynamik spinpolarisierter Elektronen in direkten Halbleitern, wonach die Spinrelaxation freier Leitungsbandelektronen durch den D'yakonov-Perel'-Mechanismus dominiert wird. Der Vergleich der gewählten Materialien zeigt insbesondere den Einfluss der Spin-Bahn-Kopplung auf die Relaxation der elektronischen Spinpolarisation in Volumenhalbleitern mit direkter Bandlücke. Neu ist, dass, bedingt durch die Bandlückenenergie der gewählten Materialien, die Dynamik von Elektronenspins in dem für Anwendungen interessanten Bereich der Telekomwellenlängen um $1.55\,\mu$m vermessen wird. Die im Rahmen dieser Arbeit durchgeführten zeitaufgelösten magneto-optischen Untersuchungen an Germanium klären fundamentale Fragen bezüglich der Orientierung und des Auslesens von Ladungsträger-Spins über indirekte optische Übergänge. Außerdem wird zum ersten Mal die Dynamik optisch induzierter Elektronen- und Lochspin-Polarisationen in einem Halbleiter mit indirekter Bandlücke umfassend untersucht. Hierbei werden die, verglichen mit Literaturwerten in direkten Halbleitern, langen Kohärenzzeiten von Lochspins in Germanium deutlich. Weiter zeigt sich der Einfluss der Viel-Tal-Struktur des indirekten Leitungsbandminimums auf die kohärente Präzession optisch induzierter Elektronenspins in äußeren Magnetfeldern. Die Untersuchungen erlauben insbesondere die Extraktion des Landé-Tensors in den indirekten Leitungsbandminima von Germanium und verdeutlichen, dass der Elliott-Yafet-Mechanismus für den Zerfall der elektronischen Spinpolarisation eine Rolle spielt.

Contents

1 Introduction 1

2 Optical orientation and spin dynamics 5

2.1 Crystal structure and energy dispersion . . . 6

2.2 Spin orientation via direct and indirect optical transitions . . . 11

2.3 Carrier spin relaxation and decoherence . . . 14

2.4 Optical readout of carrier spins . . . 18

3 Experimental setup and measuring technique 23

3.1 Magneto-optical pump-probe setup . . . 23

3.2 Temperature and magnetic field control . . . 30

4 Electron spin dynamics in direct-gap semiconductors 31

4.1 Gallium antimonide – GaSb . . . 32

4.1.1 Circular dichroism versus Faraday rotation . . . 34

4.1.2 Temperature and doping density dependences of the coherence time . . . 37

4.1.3 Influence of optically induced carrier density . . . 42

4.1.4 Spin precession at room temperature . . . 42

4.2 Indium gallium arsenide – $In_{0.53}Ga_{0.47}As$ . . . 44

4.2.1 Spin dynamics around room temperature – influences of magnetic field, temperature and optically induced carrier density . . . 45

4.2.2 Spin dynamics at low temperature – dependences on optically induced carrier density and magnetic field . . . 53

4.3 Summary . . . 59

5 Spin dynamics in the indirect-gap semiconductor germanium 61

5.1 Spin-dependent optical response . . . 63

5.2 Hole spin dynamics . . . 68

5.2.1 Effective Landé factor . . . 69

5.2.2 Coherence time – dependences on magnetic field, excitation conditions and temperature . . . 71

5.3 Electron spin precession in the L-valleys . . . 74

5.3.1 Analysis of the Landé tensor . . . 75

5.3.2 Temperature dependences of Landé tensor and spin coherence 81
5.3.3 A rate equation model for the decay of spin decoherence 87
5.3.4 Magnetic field dependence of the decay time 90
5.3.5 Crystallographic anisotropy of the decay time 91
5.4 Summary 94

6 Comparative summary and outlook **95**

Appendix **97**

A Ohmic heating of $In_{0.53}Ga_{0.47}As$ **97**

B Geometrical considerations on the L-valley electron g factors in germanium **101**
B.1 Surface orientation $\langle 100 \rangle$ 102
B.2 Surface orientation $\langle 111 \rangle$ 103

Bibliography **105**

1 Introduction

Structure size and integration density of conventional electronics approach natural limits. Therefore, spintronics – i.e. the utilisation of the spin degree of freedom in solid state systems for information processing and data storage – is a topical field of research [Wol01, Win04, Žut04, Wu10]. While storage devices based on magnetoresistance effects such as giant magneto resistance (GMR) or spin valves are commercially available, information processing in nowadays' CPUs is solely based on the electron charge. A spin transistor, as proposed by Datta and Das [Dat90], would instead use the electron spin as information carrier. Prerequisites for the realisation of spin transistors are (i) efficient spin injection and readout and (ii) controllable spin transport in semiconducting materials. Closely related, hence somewhat ambivalent, is the coupling between spin and orbital angular momentum. On the one hand, the coupling facilitates spin manipulation via electric fields. On the other hand, it causes spin relaxation in semiconductor crystals without inversion center. Consequently, the inversion-symmetric elementary semiconductors silicon and germanium in general exhibit longer spin relaxation times than inversion-asymmetric compound semiconductors, which is a definite advantage for device applications [Wu10]. Specifically, electron spin relaxation in (weakly) n-doped samples at room temperature occurs within 100 ps in the prototypical gallium arsenide (GaAs) [Hoh06], whereas in silicon roughly 10 ns are observed [Che10]. Turning the focus to spin injection and readout, it can be noted that electrical methods are favourable in view of device applications [Žut04]. Optical (spin) orientation, however, offers efficient and relatively simple spin injection [Mei84]. The research towards spintronic devices has increased focus on this possibility of photon-to-spin conversion that, at the same time, provides the basis for optical readout of carrier spins. In particular, magneto-optical pump-probe spectroscopy is a convenient technique to investigate coherent carrier spin dynamics. It is widely applied to many direct-gap semiconductors and their nanostructures, where the best researched material is certainly GaAs [Žut04, Wu10]. In contrast, optical orientation and optical spin readout in the indirect-gap semiconductors silicon and germanium is relatively unexplored, although indirect evidence of optical orientation of conduction band electrons was historically first established in silicon [Lam68][1]. As indicated above, both silicon and germanium are interesting with regard to future spintronic devices. Germanium, however, provides advantages with regard to optical properties. In contrast to silicon, the direct gap is close in energy to the (fundamental) indirect gap. Moreover, its character compares to the fundamental bandgap of typical direct-gap

[1] Lampel observed nuclear spin polarisation subsequent to optical orientation of electron spins. His and further work in the field of optically pumped nuclear magnetic resonance is reviewed in [Hay08].

semiconductors. As a result, optical orientation via direct optical transitions in germanium is as efficient as in typical direct-gap semiconductors, as is evident from spin-polarised electrons ejected via photo-ionisation [All83, Bot11]. In addition, spin currents as well as electron and hole spin polarisations have been generated and detected all-optically at the direct absorption edge of germanium [Lor09, Lor11]. These measurements reveal that both hole spin relaxation and electron scattering into the indirect conduction band minima occur within less than 1 ps at room temperature. The results are particularly interesting since they indicate that, in contrast to direct-gap semiconductors, hole spin dynamics in indirect-gap semiconductors can be accessed via interband transitions. Spin orientation and/or detection involving indirect optical transitions, however, is more complex and/or less efficient as compared to direct-gap semiconductors, since (i) the efficiency of optical orientation may be reduced due to phonon participation and (ii) the ratio of radiative and carrier spin lifetime in indirect-gap semiconductors is in general unfavourable for carrier spin readout via polarised luminescence [Ẑut04]. Nevertheless, recently, partially polarised luminescence under optical pumping conditions [Rou06], and subsequent to electrical spin injection [Jon07, Gre09] have been observed for phonon-assisted transitions in silicon. In addition, theoretical investigations on both optical orientation [Che11] and spin-dependent luminescence [Li10] associated with indirect optical transitions have been reported. Complementary to the experimental investigations described above, magneto-optical pump-probe spectroscopy at the fundamental absorption edge of indirect-gap semiconductors potentially provides direct information on the efficiency of optical orientation involving phonon-assisted transitions. In addition, electron spin dynamics in indirect conduction band minima may be observed, which is generally more sophisticated than electron spin dynamics in the conduction band minimum of direct-gap semiconductors [Rot60, Wil61, Wil64, Hal75].

Objective In the present work, the method of magneto-optical pump-probe spectroscopy is transferred to an indirect-gap semiconductor – the materials of choice is germanium (Ge) – to clarify fundamental questions on carrier spin injection and readout via phonon-assisted transitions. These questions concern specifically (i) the relative efficiency of carrier spin orientation via direct and indirect optical transitions, (ii) the possibility to detect hole spins, (iii) coherence times of optically induced carrier spin polarisations, and (iv) the impact of the multivalley structure of the indirect conduction band minimum on coherent precession of optically induced electron spins in external magnetic fields. For comparison, selected direct-gap semiconductors are investigated, namely indium gallium arsenide ($In_{0.53}Ga_{0.47}As$) and gallium antimonide (GaSb). Additionally, these materials are well suited to improve and/or confirm the present understanding of electron spin relaxation and decoherence in direct-gap semiconductors. In particular, theoretical predictions on the impact of spin-orbit coupling can be examined, since the coupling strength is considerably stronger in GaSb than in $In_{0.53}Ga_{0.47}As$ or the prototypical GaAs. Moreover, the selected materials allow for optical detection of spin coherence in the telecom wavelength band around $1.55\,\mu$m.

Outline The thesis is organised as follows. The basic concepts of optical spin orientation, dynamics and readout are presented in chapter 2. As a starting point, the situation for direct-gap semiconductors is recapitulated. In addition, expectations for indirect-gap semiconductors are discussed. In chapter 3, the magneto-optical pump-probe setup is described and the equipment for temperature and magnetic-field control is presented. The experimental results are discussed in chapters 4 and 5. Chapter 4 focusses on electron spin dynamics in GaSb and $In_{0.53}Ga_{0.47}As$. Results on optical orientation and carrier spin readout in Ge are detailed in chapter 5. The chapter provides comprehensive analyses of hole spin dynamics as well as electron spin dynamics in the multivalley conduction band of Ge. The main findings are summarised at the end of each chapter of results. A comparative presentation of optical orientation, carrier spin readout and carrier spin dynamics in direct-gap semiconductors and Ge is given in chapter 6, where in addition proposals for future magneto-optical pump-probe investigations on carrier spin dynamics in indirect-gap semiconductors are presented.

2 Optical orientation and spin dynamics

The concept of spin angular momentum was suggested by Uhlenbeck and Goudsmit in 1925 to explain the deviations of experimentally observed atomic spectral lines from the Bohr-Sommerfeld model of the atom [Pai89]. The spin angular momentum is an intrinsic property of all elementary particles. While bosons are characterized by integer spin quantum numbers, fermions carry half-integer spin. Electrons are spin-1/2 particles. Choosing the z-axis as the quantisation direction, the spin operator takes the form $\boldsymbol{S} = \hbar\boldsymbol{\sigma}/2$ with the vector of Pauli matrices $\boldsymbol{\sigma} = (\sigma_x, \sigma_y, \sigma_z)^T$ [1]. The eigenvalues of the z-component of $\boldsymbol{S}$ are $S_z = \hbar m_s = \pm\hbar/2$. The respective spin eigenstates are commonly labelled as $\langle\uparrow|$ or spin up and $\langle\downarrow|$ or spin down. The spin angular momentum of the electron gives rise to the spin magnetic moment

$$\boldsymbol{\mu}_S = -g\frac{\mu_B}{\hbar}\boldsymbol{S}, \tag{2.1}$$

where $\mu_B = e\hbar/\,2mc$ with the elementary charge e and the electron rest mass m. $g = 2$ is the Landé factor according to the Dirac equation for a free spin-$1/2$ particle [2]. The Zeeman Hamiltonian for a free electron spin in a static magnetic field oriented in z-direction, $\boldsymbol{B} = B\boldsymbol{z}$, is

$$\mathscr{H}_Z = -\boldsymbol{\mu}_S \cdot B\boldsymbol{z} = \boldsymbol{\omega}_L \cdot \boldsymbol{S}, \tag{2.2}$$

where

$$\boldsymbol{\omega}_L = \frac{g\mu_B B}{\hbar}\boldsymbol{z} \tag{2.3}$$

denotes the Larmor frequency with the Bohr magneton $\mu_B = e\hbar/(2m)$. The corresponding time-dependent Schrödinger equation for the expectation value of the spin operator $\langle\boldsymbol{S}\rangle$ simplifies to the differential equation

$$\langle\dot{\boldsymbol{S}}\rangle = \boldsymbol{\omega}_L \times \langle\boldsymbol{S}\rangle. \tag{2.4}$$

The component of $\langle\boldsymbol{S}\rangle$ parallel to the magnetic-field direction is thus independent of time, whereas the perpendicular components precess along the magnetic-field direction at the Larmor frequency.

---

[1] These are explicitly $\sigma_x = \begin{pmatrix} 0 & 1 \\ 1 & 0 \end{pmatrix}$, $\sigma_y = \begin{pmatrix} 0 & -i \\ i & 0 \end{pmatrix}$ and $\sigma_z = \begin{pmatrix} 1 & 0 \\ 0 & -1 \end{pmatrix}$.

[2] Today, the most precise experimental value for the Landé factor of free electrons is $g = 2.00231930436153(53)$[Odo06]. The difference from the value of 2 arises from quantum electrodynamic corrections.

Spin dynamics of electron and hole spin ensembles in semiconductors is more complex. The carriers are exposed to the periodic crystal potential and undergo spin-orbit interaction. The result is an energy band structure specific to the respective material. The precession of carriers in the vicinity of extrema in the band structure can, however, be described in analogy to the precession of a free electron spin using an effective Landé factor. The basics for such a description are recapitulated in section 2.1. Absorption of circularly polarised light can induce macroscopic spin polarisation in the presence of spin-orbit interaction. The phenomenon known as optical (spin) orientation is reviewed in section 2.2. The optically induced spin polarisation as a non-equilibrium state interacting with its environment is subject to decoherence and relaxation. Section 2.3 gives an overview over the relevant mechanisms. A phenomenological explanation for the Faraday effect as the basis for optical readout of carrier spins is given in section 2.4, where in addition the introduced concepts are related to magneto-optical pump-probe spectroscopy. Parts of the presentation follow textbooks and/or review articles connected to the current subjects [Yu10, Mei84, Žut04, Sug00].

2.1 Crystal structure and energy dispersion

The crystal structures relevant for the present work are the diamond and the zinc-blende structure. Ge crystallises in the former structure, GaSb and $In_{0.53}Ga_{0.47}As$ in the latter. As is illustrated in figure 2.1, both crystals are characterised by a face-centred cubic lattice with a basis of two atoms located at $(0,0,0)$ and $(1/4,1/4,1/4)$ within the unit cell. In contrast to the inversion symmetric diamond structure, the basis of the zinc-blende structure consists of two different atoms ($In_{0.53}Ga_{0.47}As$ is derived from GaAs by replacing 53 % of the gallium atoms by indium). The semiconductor lattice is formed by 10^{23} atoms per cm^{-3}, the lattice constant is typically a few Ångstroms. The outer s- and p-orbitals of neighbouring atoms are occupied by three (Ga and In), four (Ge) or five (As and Sb) electrons and hybridise to form tetrahedral bonds. In accordance to the Pauli exclusion principle, the bonding and anti-bonding orbitals form occupied valence and unoccupied conduction bands. In the absence of an external magnetic field, the Schrödinger equation for a charge carrier in the crystal environment is

$$\mathscr{H}_c \Psi_{n\boldsymbol{k}}(\boldsymbol{r}) = \left[\frac{\boldsymbol{p}^2}{2m} + V(\boldsymbol{r}) + \mathscr{H}_{SO}\right] \Psi_{n\boldsymbol{k}}(\boldsymbol{r}) = E_{n\boldsymbol{k}} \Psi_{n\boldsymbol{k}}, \tag{2.5}$$

where $\boldsymbol{p}$ is the canonical momentum of the carrier, $V(\boldsymbol{r})$ denotes the periodic potential stemming from the ion cores, and n is the band index. The spin-orbit Hamiltonian

$$\mathscr{H}_{SO} = \frac{\hbar}{4m^2c^2} [\nabla V \times \boldsymbol{p}] \cdot \boldsymbol{\sigma} \tag{2.6}$$

is motivated as follows. A charge carrier of velocity $\boldsymbol{v}$ moving in the electric field $\boldsymbol{E} = \nabla V$ of the ion cores experiences a related magnetic field $\boldsymbol{B}_{SO} = 1/c\,(\boldsymbol{E} \times \boldsymbol{v})$, where c denotes the velocity of light. The spin magnetic moment of the charge carrier interacts with $\boldsymbol{B}_{SO}$ according to $\mathscr{H}_{SO} = -\boldsymbol{\mu}_S \cdot \boldsymbol{B}_{SO}$.

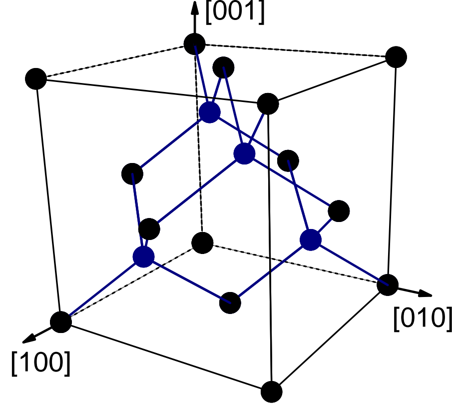

FIGURE 2.1 *Crystal structure of GaSb, $In_{0.53}Ga_{0.47}As$ (zinc-blende lattice) and Ge (diamond lattice). Both lattice types are characterised by a face-centred cubic lattice with two atoms per lattice site, i.e. located at $(0,0,0)$ and $(1/4,1/4,1/4)$. The basis in diamond-type crystals consist of two atoms of the same chemical species, whereas in zinc-blende structured crystals the basis atoms are of different type.*

Equation (2.6) is recovered with $\boldsymbol{v} = \boldsymbol{p}/m$. The eigenfunctions of $\mathscr{H}_c$ are the Bloch functions

$$\Psi_{n\boldsymbol{k}}(\boldsymbol{r}) = \exp(i\boldsymbol{k}\cdot\boldsymbol{r})\, u_{n\boldsymbol{k}}(\boldsymbol{r}),$$

where the $u_{n\boldsymbol{k}}(\boldsymbol{r})$ have the same periodicity as the lattice. The wavevector $\boldsymbol{k}$ is restricted to the first Brillouin zone without loss of information on the energy dispersions $E_{n\boldsymbol{k}}$. Within the $\boldsymbol{k}\cdot\boldsymbol{p}$-method the energy dispersions as well as the wavefunctions satisfying the Schrödinger equation (2.5) are expanded in second order perturbation theory at an assigned point $\boldsymbol{k}'$, at which the band energies $E_{n\boldsymbol{k}'}$ and the wavefunctions $u_{n\boldsymbol{k}'}$ are known.

In typical zinc-blende structured semiconductors and in Ge the wavefunction of the lowest conduction band state at $k = 0$ – commonly denoted Γ-point – corresponds to the atomic s-orbital $|S\rangle$. The valence band states are linear combinations of the p-orbitals $|X\rangle$, $|Y\rangle$ and $|Z\rangle$. The orbital angular momentum quantum number is $l = 0$ for the conduction band and $l = 1$ for the valence band. The respective projections of the orbital momentum $\boldsymbol{L}$ onto the z-axis are $m_l = 0$ and $m_l = -1, 0, +1$. Since the spin-orbit Hamiltonian (2.6) is proportional to

$$\boldsymbol{L}\cdot\boldsymbol{S} = 1/2\left(\boldsymbol{J}^2 - \boldsymbol{L}^2 - \boldsymbol{S}^2\right) = 1/2\,[j(j+1) - l(l+1) - s(s+1)],$$

the valence band with $m_l = 0$ is separated in energy from the two degenerate $m_l = \pm 1$ valence bands by the spin-orbit splitting energy Δ.The conduction band is characterised by the quantum number of total angular momentum $j = 1/2$. The projection of $\boldsymbol{J}$ onto the z-axis is $m_j = \pm 1/2$. The quantum numbers for the valence bands are $j = 3/2$ with $m_j = \pm 3/2$ for the heavy holes (hh) or $m_j = \pm 1/2$ for the light holes (lh) and $j = 1/2$ with $m_j = \pm 1/2$ for the split-off holes (so). All

bands are two-fold spin degenerate. The respective wavefunctions are listed in table 2.1.

Figure 2.2 illustrates exemplarily the band structure of Ge. The fundamental bandgap is indirect: the valence band maximum is located at $k = 0$ whereas the global minimum of the conduction band is found at the edge of the first Brillouin zone in [111]-direction, that is denoted L-point. According to the eight [111]-directions of the cubic unit cell, $8/2 = 4$ equivalent L-valleys exist. In contrast, GaSb and $In_{0.53}Ga_{0.47}As$ are direct-gap semiconductors with both the global minimum of the conduction band and the maximum of the valence band located at the Γ-point. The minimum energy difference of valence- and conduction band is denoted fundamental bandgap or E_g. Table 2.2 summarises band parameters of the semiconductors investigated in the present work. The energy differences between the conduction band minima at the Γ- or L-point and the valence band maximum are denoted E_Γ and E_L, respectively. The parameters are valid below approximately $T = 100\,\mathrm{K}$ except for the split-off energy, that is not markedly affected by temperature up to room temperature (cf. e.g. [Lau87]). At temperatures above 100 K the bandgap decreases linearly with temperature due to interactions of electrons with lattice vibrations – or phonons – as well as due to thermal expansion. The temperature dependence of the energy gap is phenomenologically described by

$$E_g(T) = E_g(0) + \frac{AT^2}{B+T} \tag{2.7}$$

with A and B tabulated for many cubic semiconductors (in the present work, the parameters from [Vur01] are used).

Starting from a non-degenerate band extremum in an arbitrary direction the $\boldsymbol{k}\cdot\boldsymbol{p}$-expansion results in the parabolic dispersion

$$E_{\boldsymbol{k}} = E_{\boldsymbol{k}'} + \frac{\hbar^2(\boldsymbol{k}-\boldsymbol{k}')^2}{2m^*},$$

where the band index n is omitted, since only the minima of the lowest conduction band are of interest. The motion of a conduction band electron is thus analogue to the motion of a free electron with the effective mass m^*. The effective mass is in general direction-dependent, i.e. a tensor, reflecting the symmetry representation of the examined band extremum. In proximity to the Γ-point, the effective mass in the conduction band m_c is independent of the direction of motion. This corresponds to spherical surfaces of constant energy. At the L-point, the band curvature depends on the direction in $\boldsymbol{k}$-space as is reflected by ellipsoidal surfaces of constant energy. The effective mass tensor consists of two independent components m_l and m_t. The effective masses in the global conduction band minima of Ge, GaSb and $In_{0.53}Ga_{0.47}As$ are included in table 2.2. The values are again valid at temperatures below approximately 100 K. The temperature dependence of the effective mass is closely related to that of the bandgap. However, m_c solely depends on the thermal expansion of the bandgap [Ehr57, Zaw08]. The $\boldsymbol{k}\cdot\boldsymbol{p}$-expansion for the valence band maximum in cubic semiconductors is somewhat more complicated due to degeneracy. As a result, the effective heavy- and light-hole masses feature a direction dependence that is not appropriately described by a symmetric tensor. In many cases it is, however, sufficient to approximate the

	wavefunction	j	m_j
conduction band	$\|S\uparrow\rangle$	1/2	1/2
	$\|S\downarrow\rangle$		−1/2
heavy holes	$\left\|\sqrt{1/2}\,(X+iY)\uparrow\right\rangle$	3/2	3/2
	$\left\|\sqrt{1/2}\,(X-iY)\downarrow\right\rangle$		−3/2
light holes	$\left\|\sqrt{1/6}\,[(X+iY)\downarrow+2Z\uparrow]\right\rangle$		1/2
	$\left\|-\sqrt{1/6}\,[(X-iY)\uparrow-2Z\downarrow]\right\rangle$		−1/2
split-off	$\left\|-\sqrt{1/3}\,[(X+iY)\downarrow-Z\uparrow]\right\rangle$	1/2	1/2
	$\left\|\sqrt{1/3}\,[(X-iY)\uparrow+Z\downarrow]\right\rangle$		−1/2

TABLE 2.1 *Electronic wavefunctions at the Γ-point according to [Žut04] together with the total angular momentum j and its projection onto the z-direction m_j.*

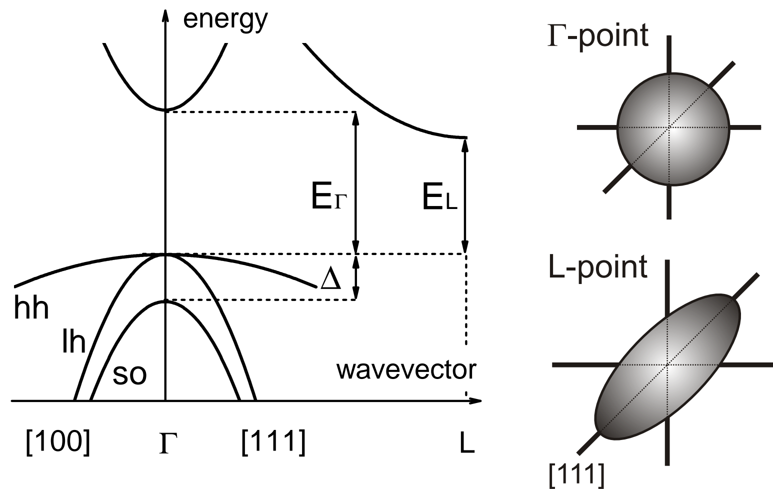

FIGURE 2.2 *Schematic representation of the band structure of Ge. The valence band consists of heavy-hole, light-hole and split-off band. The global minima of the conduction band are located at the L-point. The surfaces of constant energy are spheres in the Γ-valley and ellipsoids in the L-valleys. The band structures of GaSb and $In_{0.53}Ga_{0.47}As$ are similar except for the global conduction band minimum being located at the Γ-point.*

	E_Γ (eV)	E_L (eV)	Δ	m_c
GaSb	0.812 (E_g)	0.875	0.76	0.039
$In_{0.53}Ga_{0.47}As$	0.816 (E_g)	1.37	0.35	0.043
Ge	0.89	0.742 (E_g)	0.29	$m_l = 1.59$ / $m_t = 0.0815$

TABLE 2.2 *Band parameters of the investigated semiconductors. Gap energies and effective masses in units of m are valid for $T \lesssim 100\,\mathrm{K}$. The values are taken from [Vur01] for GaSb and $In_{0.53}Ga_{0.47}As$ except the split-off energy for $In_{0.53}Ga_{0.47}As$ [Spi00]. The parameters for Ge are according to [Iof].*

effective hole masses by scalars. For GaSb, for example, these are $m_{hh} = 0.4m$, $m_{lh} = 0.05m$ and $m_{so} = 0.14m$ for heavy holes, light holes and split-off holes, respectively [Iof].

In the presence of an external magnetic field $\boldsymbol{B} = \nabla \times \boldsymbol{A}$, the Zeeman Hamiltonian (2.2) adds to the Hamiltonian $\mathscr{H}_c$ in the Schrödinger equation (2.5). In addition, the canonical momentum is replaced by its kinetic equivalent $\boldsymbol{P} = \boldsymbol{p} + e\boldsymbol{A}$, so that the spin-orbit Hamiltonian reads as

$$\mathscr{H}_{SO}^B = \mathscr{H}_{SO} + \frac{\hbar}{4m^2c^2}\left[\nabla V \times e\boldsymbol{A}\right]\cdot\boldsymbol{\sigma}$$

with the spin-orbit Hamiltonian $\mathscr{H}_{SO}$ given in equation (2.6). The Hamiltonian for a charge carrier is then [Lut55]

$$\mathscr{H}_c^B = \left[\frac{(\boldsymbol{p}+e\boldsymbol{A})^2}{2m} + V(\boldsymbol{r}) + \mathscr{H}_{SO}\right] + \left[\frac{\hbar}{4m^2c^2}\left[\nabla V \times e\boldsymbol{A}\right]\cdot\boldsymbol{\sigma} + \frac{1}{2}g\mu_B\boldsymbol{B}\cdot\boldsymbol{\sigma}\right]. \tag{2.8}$$

Again, the energy dispersion in proximity to band extrema can be determined by perturbative expansion maintaining the analogy to free electrons. For a non-degenerate band extremum, and defining $\boldsymbol{k}' = 0$ without loss of generality, the expansion yields

$$E_{lk_z}^{\pm} = \left[\frac{\hbar^2k_z^2}{2m^*} + \hbar\omega_c\left(l + \frac{1}{2}\right)\right] \pm \frac{1}{2}g^*\mu_B B,$$

where $E_{lk_z}^{+}$ and $E_{lk_z}^{-}$ are the dispersions for a spin-down and a spin-up carrier, respectively. The contribution in the squared brackets expresses the Landau quantisation of the energy levels due to the external magnetic field: the electron motion is undisturbed in magnetic-field direction, while it is confined to cyclotron orbits in the plane perpendicular to the magnetic-field direction. The cyclotron frequency is $\omega_c = \hbar eB/(m^*c)$. Just like the effective mass, the effective Landé factor g^* is a tensor in general. Spin precession of electrons in the Γ-valley is characterised by an isotropic Landé tensor $\boldsymbol{g}^*$. The Landé factor for electrons in the Γ-valley of many III-V semiconductors is

well approximated in three-band $\boldsymbol{k}\cdot\boldsymbol{p}$-theory, that is [Her77]

$$g^* = \frac{P^2}{3}\left(\frac{1}{E_g} - \frac{1}{E_g+\Delta}\right). \tag{2.9}$$

$P^2 = (2/m)|\langle S|\, p_i\, |I\rangle|^2$ with $i = x$, y or z and $\langle I| = \langle X|$, $\langle Y|$ or $\langle Z|$ is proportional to the interband matrix element that couples an s-like conduction band state to a p-like valence band state. With the parameters given in [Her77] – $P^2 = (20-30)\,\mathrm{eV}$ in a variety of III-V semiconductors – the low-temperature limit of the electron effective Landé factor for GaSb is $g^* = -9.0$. Using the weighted average of the values for P^2 for GaAs and InAs and the band energies given in table 2.2, the result for $In_{0.53}Ga_{0.47}As$ is $g^* = -4.2$. In the L-valleys in contrast, $\boldsymbol{g}^*$ is a diagonal tensor with two independent components g_l and g_t as a result from the ellipsoidal shape of the surfaces of constant energy. As in the case of Γ-valley electrons in III-V materials, the components of the Landé tensor for electrons in the L-valleys of Ge can be assessed from a small number of band parameters. The components explicitly are [Rot60]

$$g_{l/t} \sim 2 - \frac{2}{3}\frac{\Delta}{E_L^{cv}}\left(\frac{m}{m_{t/l}} - 1\right). \tag{2.10}$$

With the energy difference between valence and conduction band at the L-point $E_L^{cv} \sim 2\,\mathrm{eV}$ and the effective masses and Δ from table 2.2, this estimation yields $g_l = 2$ and $g_t = 0.9$.

2.2 Spin orientation via direct and indirect optical transitions

In general, absorption of a photon of appropriate energy $\hbar\omega$ – specifically $\hbar\omega \geq E_g$ – generates an electron in the conduction band and a hole in the valence band of a semiconductor. As already mentioned, in spin-orbit coupled systems absorption of circularly polarised light is an efficient tool to generate carrier spin polarisation. For direct optical transitions in III-V semiconductors and germanium, this is understood in analogy to optical orientation in atoms. For indirect transitions, the situation is somewhat more complex since phonons are necessary to ensure momentum conservation. The optical pumping community [Hay08, cf. introduction 1] commonly describes electron spin orientation via indirect transitions in silicon in a two-step model. The electron spins are first oriented via virtual direct transitions. The subsequent scattering into the fundamental (indirect) conduction band minima is assumed to conserve spin polarisation. As mentioned previously, a comprehensive theoretical description of spin-dependent indirect optical transitions has been developed only recently and again for silicon [Che11, Li10]. In the following, carrier spin orientation via direct optical transitions in III-V semiconductors and germanium is briefly recapitulated. In addition, electron spin orientation via indirect optical transitions in germanium is discussed in compliance with the results of Cheng et al. [Che11].

Direct transitions at the Γ-point The probability per unit time for direct optical transitions between valence band states $\langle v|$ of energy $E_v(\boldsymbol{k_v})$ and conduction band states $\langle c|$ of energy $E_c(\boldsymbol{k}_c)$ with $\boldsymbol{k} = \boldsymbol{k}_v = \boldsymbol{k}_c$ is given by Fermi's Golden Rule

$$W_{direct} = \frac{2\pi}{\hbar} \sum_{\boldsymbol{k}} \left| \left\langle c \left| \mathscr{H}_{el-phot} \right| v \right\rangle \right|^2 \delta\left(E_c(\boldsymbol{k}) - E_v(\boldsymbol{k}) - \hbar\omega\right). \tag{2.11}$$

The Hamiltonian $\mathscr{H}_{el-phot} = e\boldsymbol{r} \cdot \boldsymbol{E}$ describes the interaction between the electric dipole $e\boldsymbol{r}$ of an electron-hole pair and the electric field $\boldsymbol{E}$ of the incident light. For right- or left-circularly polarised light propagating along the z-axis the Hamiltonian can be expressed in terms of orbital symmetries

$$\mathscr{H}^{\pm}_{el-phot} \propto X \pm iY. \tag{2.12}$$

From the point of view of quantum mechanics, circularly polarised light consists of photons with angular momentum $\hbar$ oriented either parallel – right-circular or σ^+ – or anti-parallel – left-circular or σ^- – with respect to the direction of light propagation. At the Γ-point in zinc-blende- or diamond-structured semiconductors, $\langle v|$ and $\langle c|$ are the Bloch functions listed in table 2.1. Due to their orbital symmetries, the transition matrix element $M_{c \to v} = \left| \left\langle c \left| \mathscr{H}_{el-phot} \right| v \right\rangle \right|^2$ is non-zero only for transitions with $\Delta m_j = m_{j,c} - m_{j,v} = \pm 1$ in accordance with conservation of angular momentum. Plus and minus sign hold for σ^+- and σ^--light, respectively. A schematic view of the allowed transitions is shown in figure 2.3. In the following, the optical transitions under σ^+ excitation are discussed exemplarily. (The carrier spin polarisations induced by σ^- excitation are the same except for the sign.) The allowed transitions are, first, from the heavy hole band with $m_j = -3/2$ to the conduction band with $m_j = -1/2$, second, from the light hole band with $m_j = -1/2$ to the conduction band with $m_j = 1/2$. Third, transitions from the split-off holes with $m_j = -1/2$ to the conduction band with $m_j = 1/2$ are possible. However, for photon energies $\hbar\omega$ that exceed E_Γ but are smaller than $E_\Gamma + \Delta$, no electrons are excited from the split-off band to the conduction band. In the following, the spin polarisation of the photogenerated electrons is denoted P_e and that of the holes is denoted P_h. To determine P_e and P_h, that are defined as the average S_z generated per photon compared to the ideal case where each photon generates a carrier with $S_z = \frac{\hbar}{2}$, the relative transition amplitudes as well as the spin projections of the involved states are required explicitly. The transition matrix elements are

$$\begin{aligned} M_{hh \to cb} &= \left| \langle S \downarrow | X + iY | \sqrt{\frac{1}{2}} \left[(X - iY) \downarrow \right] \rangle \right|^2 = \frac{1}{2} P^2 \\ M_{lh \to cb} &= \left| \langle S \uparrow | X + iY | -\sqrt{\frac{1}{6}} \left[(X - iY) \uparrow \right] - \sqrt{\frac{1}{3}} Z \downarrow \rangle \right|^2 = \frac{1}{6} P^2 \end{aligned}$$

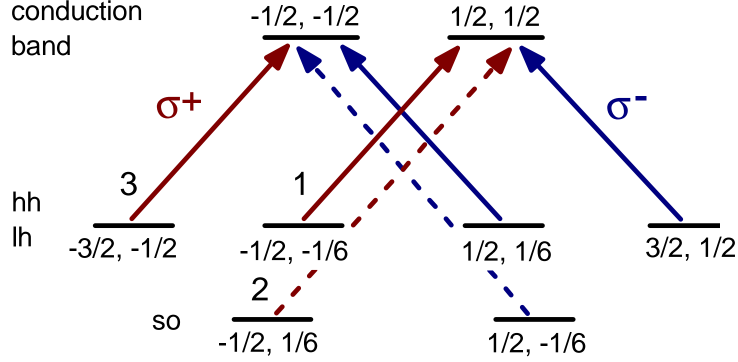

FIGURE 2.3 *Allowed interband transitions at the Γ-point. The levels are labelled by the projections of total and spin angular momentum onto the propagation direction of light, m_j and m_s, following [Rio10]. The relative amplitudes for transitions between the m_j sublevels are indicated exemplarily for right-circularly polarised light.*

or, in ratio $M_{hh\to cb} : M_{lh\to cb} = 3 : 1$. The projections of the spin onto the z-direction $\langle c|\, \sigma_z \,|v\rangle$ are included in figure 2.2. Altogether, absorption of circularly polarised light at the fundamental absorption edge in GaSb, $In_{0.47}Ga_{0.53}As$ and comparable III-V compounds, as well as at the direct absorption edge of Ge induces an electron spin polarisation of

$$P_e = \frac{3\left(-\frac{1}{2}\right)+1\left(\frac{1}{2}\right)}{\frac{1}{2}\left(3+1\right)} = -50\,\%, \tag{2.13}$$

and a hole spin polarisation of [Rio10]

$$P_h = -\frac{3\left(-\frac{1}{2}\right)+1\left(-\frac{1}{6}\right)}{\frac{1}{2}\left(3+1\right)} = 83.3\,\%. \tag{2.14}$$

Interestingly, no net electron spin polarisation would result if spin-orbit coupling was absent. Then, transitions from the split-off band to the conduction band would contribute with a relative transition amplitude of 2, resulting in

$$P_e = \frac{3\left(-\frac{1}{2}\right)+1\left(\frac{1}{2}\right)+2\left(\frac{1}{2}\right)}{\frac{1}{2}\left(3+1+2\right)} = 0.$$

Indeed, a sophisticated theoretical approach [Nas07, Rio10] reveals that the band edge electron spin polarisation (2.13) decreases markedly for $\hbar\omega > E_\Gamma + \Delta$. The decrease is, however, only partly attributed to transitions from the split-off band to the conduction band. The main reason is rather the energy dependence of transitions from the heavy-hole band to the conduction band. Turning the focus to the hole spin polarisation (2.14), according to Rioux et al. [Rio10], such a relatively high value occurs only for excitation exactly at the absorption edge, since P_h results from

a superposition of heavy hole states and light hole states. For $\hbar\omega > E_\Gamma$, $P_h(\hbar\omega)$ approximately matches $-P_e(\hbar\omega)$[3].

Indirect transitions to the L-valleys Irradiating Ge with photons that exceed the fundamental (indirect) bandgap but not the direct bandgap in energy ($E_\Gamma < \hbar\omega < E_g$) generates electrons with quasi-momentum $\boldsymbol{k}_c$ and holes with quasi-momentum $\boldsymbol{k}_v = \boldsymbol{k}_c \mp \boldsymbol{q}$. Such a process involves first, an electron-photon interaction, and second, an interaction of the electron and a phonon with momentum $\boldsymbol{q}$ and frequency ω_q. In sum, energy and quasi-momentum are conserved. According to Fermi's Golden rule in second order perturbation, the transition probability per unit time for indirect transitions is

$$W_{indirect} = \frac{2\pi}{\hbar} \sum_{\boldsymbol{k}_v, \boldsymbol{k}_c} \left| \sum_z \frac{\langle f | \mathscr{H}_{el-phon} | z \rangle \langle z | \mathscr{H}_{el-phot} | i \rangle}{E_z - E_v(\boldsymbol{k}_v) \mp \hbar\omega_q - \hbar\omega} \right|^2 \delta\left(E_c(\boldsymbol{k}_c) - E_v(\boldsymbol{k}_v) - \hbar\omega \pm \hbar\omega_q\right). \quad (2.15)$$

The initial state consists of an electron in the valence band and a specified number of occupied phonon states N_q. In the final state, the electron occupies a conduction band state, and N_q is changed by ± 1. The virtual intermediate states $\langle z|$ are of energy E_z. It can be concluded from equation (2.15) that the degree of carrier spin polarisation resulting from optical transitions across an indirect fundamental bandgap is not only determined by the selection rules for angular momentum, but also by spin-dependent electron-phonon interactions. As mentioned above, the degree of spin polarisation related with indirect optical transitions is subject to current research. Specifically, the above mentioned theoretical investigation by Cheng et al. reveals $P_e = -25\,\%$ in silicon for excitation with σ^- light just above the bandgap, and at $T = 4\,\mathrm{K}$. The same polarisation degree is associated with direct optical transitions at the Γ-point in silicon [Nas07]. However, as a result of phonon contributions, P_e degrades below $5\,\%$ before $\hbar\omega$ excesses $E_g + E_{TO}$, where $E_{TO} \sim 60\,\mathrm{meV}$ is the energy of the involved transversal optical (TO) phonon. Translating these results to Ge, $P_e = 50\,\%$ is expected at the indirect bandgap. The degree of polarisation should albeit degrade markedly within an even narrower energy window, since the phonon energies in Ge are approximately half of those in silicon [Iof].

2.3 Carrier spin relaxation and decoherence

In physical systems, a spin or spin ensemble interacts with its environment. The dynamics of an ensemble of N coherent electron spin states is described analogue to equation (2.4), including phenomenological relaxation terms. Explicitly, the time evolution of the ensemble magnetisation

[3] Specifically, simulations assuming pulsed instead of continuous wave excitation indicate that the band edge hole spin polarisation (2.14) is approximately preserved as long as the central pulse energy exceeds E_Γ by less than the spectral width of the laser pulses.

$\boldsymbol{M} = N\langle \boldsymbol{\mu}_S \rangle = -Ng\mu_B \langle \boldsymbol{S} \rangle / \hbar$ is described by

$$\begin{aligned} \frac{dM_x}{dt} &= (\boldsymbol{\omega}_L \times \boldsymbol{M})_x - \frac{M_x}{T_2} \\ \frac{dM_y}{dt} &= (\boldsymbol{\omega}_L \times \boldsymbol{M})_y - \frac{M_y}{T_2} \\ \frac{dM_z}{dt} &= (\boldsymbol{\omega}_L \times \boldsymbol{M})_z - \frac{M_z - M_z^0}{T_1}. \end{aligned} \tag{2.16}$$

Such a set of equations was introduced by Felix Bloch in 1946 [Blo46] to model the dynamics of nuclear magnetisation. The time constants T_1 and T_2 characterise relaxation in and perpendicular to the magnetic-field direction, respectively. The former – also referred as longitudinal relaxation – involves transitions between the Zeemann levels. These spin flips come along with energy exchange with the environment and the magnetisation component in magnetic-field direction relaxes to the thermal equilibrium value M_z^0. The latter transversal relaxation processes reduce phase coherence. Concerning a single spin – which is a superposition of $\langle\uparrow|$ and $\langle\downarrow|$ – the phase between the eigenstates is randomised within T_2. Observing an ensemble, T_2 is the time scale of irreversible loss of phase coherence between the individual spin states. In contrast, $T_2^* \leq T_2$ commonly denotes reversible losses[4], such as the loss of phase coherence in an ensemble of donor-bound – and thus localised – electrons, due to local fluctuations in the magnetic-field amplitude. In general, measurements on spin ensembles in semiconductors probe T_2^* instead of T_2 [Hu01]. Spin relaxation and decoherence of quasi-free conduction band electrons – or itinerant electrons – is, however, characterised by a single coherence time scale τ_s, since $T_2 = T_2^*$. In addition, in cubic semiconductors $T_1 \leq 2T_2$.

The spin relaxation time in general depends on material characteristics as well as experimental conditions, such as crystal symmetry, doping concentration and dopant, lattice temperature and optically induced carrier density. Several microscopic mechanisms are known to contribute to carrier spin relaxation in semiconductors. For itinerant electrons, these are the Elliott-Yafet (EY), the D'yakonov-Perel' (DP) and the Bir-Ahronov-Pikus (BAP) mechanism. Dealing with donor-bound electrons, hyperfine interaction as well as anisotropic exchange interaction dominate spin relaxation. Hole spin relaxation is typically orders of magnitude faster than electron spin relaxation resulting from the stronger influence of spin-orbit coupling [Yu05].

Elliott-Yafet relaxation As a consequence of spin-orbit coupling, it is not possible to factorise the carrier wavefunctions into orbital and spin components. In other words, the wavefunctions $\Psi_{n\boldsymbol{k}\uparrow}$ and $\Psi_{n\boldsymbol{k}\downarrow}$ are not spin eigenstates, but $\Psi_{n\boldsymbol{k}\uparrow}$ contains a – comparatively small – spin down component and vice versa . Although interactions driving carrier momentum scattering – such as carrier-phonon, carrier-impurity and carrier-carrier interactions – are spin-independent, this admixture results in a non-zero probability of a spin flip accompanying a momentum scattering event.

[4] Reversible phase decoherence can be retrieved in spin-echo experiments.

Thus, EY relaxation is characterised by a spin relaxation time proportional to the momentum relaxation time τ_p [Ell54, Yaf63].

Considering electrons in the isotropic and parabolic global conduction band minimum of a III-V semiconductor, momentum relaxation is dominated by scattering events accompanied with relatively small momentum changes. The corresponding scattering potentials are long-ranged and smooth. Under this precondition, the EY spin relaxation rate is

$$\left(\frac{1}{\tau_s(E_{\boldsymbol{k}})}\right)_{EY} = A\beta^2\left(\frac{E_{\boldsymbol{k}}}{E_g}\right)\frac{1}{\tau_p(E_{\boldsymbol{k}})}, \tag{2.17}$$

where $\tau_p(E_{\boldsymbol{k}})$ denotes the momentum relaxation time of an electron with kinetic energy $E_{\boldsymbol{k}}$. $\beta = \gamma(1-\gamma/2)/(1-\gamma/3)$ with $\gamma = \Delta/(\Delta+E_g)$ is determined by the fundamental bandgap energy and the spin-orbit splitting of the valence band. A is a dimensionless parameter that depends on the relevant momentum scattering mechanism.

D'yakonov-Perel' relaxation In the absence of inversion symmetry, the spin degeneracy is lifted in some direction in $\boldsymbol{k}$-space even without an external magnetic field. Such an energy-level splitting can technically be described by an internal $\boldsymbol{k}$-dependent magnetic field acting on the carrier spin states [D'y72]. Due to the dependence on $\boldsymbol{k}$, the frequency at which a spin precesses along the internal magnetic field is changed by electron momentum scattering from a state $\Psi_{n,\boldsymbol{k}\uparrow}$ to a state $\Psi_{n,\boldsymbol{k}'\uparrow}$. The impact depends on the ratio of the average frequency Ω of spin precession along the internal magnetic field and the momentum scattering time τ_p. For $\Omega \gg \tau_p$, each individual spin completes several precession cycles at the frequency associated with its location in $\boldsymbol{k}$-space, before the respective charge carrier is scattered to another state characterised by $\boldsymbol{k}'$. In this ballistic regime, the ensemble spin relaxes the faster the more momentum scattering events occur per unit time. Given that, alternatively, Ω is small compared to the inverse momentum relaxation time, a particular spin does not undergo a full precession cycle, but moves through $\delta\Phi = \Omega\tau_p$ before the respective carrier momentum is changed and the spin sees a different internal magnetic field. Mathematically, this is described by a random walk of the spin state. After $n = t/\tau_p$ steps, the accumulated phase is $\Phi(t) = \delta\Phi\sqrt{t}/\tau_p$. Identifying the spin relaxation time by $\Phi(\tau_s) = 1$, it is $(\tau_s)^{-1} = \Omega^2\tau_p$. Hence in this motional narrowing regime – in contrast to the ballistic regime described above – enhancing the momentum relaxation rate slows down spin relaxation. Commonly, precessional dephasing in the motional narrowing regime is denoted DP relaxation.

The explicit form of electron spin-orbit coupling in semiconductors without inversion center is

$$\mathscr{H}_{SO}^{BIA} = \frac{\hbar}{2}\boldsymbol{\Omega}_{BIA}(\mathbf{k})\cdot\boldsymbol{\sigma}, \tag{2.18}$$

where

$$\mathbf{\Omega}_{BIA}(\mathbf{k}) = \frac{\alpha\hbar^2}{\sqrt{2E_g(m_c)^3}} \begin{pmatrix} \left(k_y^2 - k_z^2\right) k_x \\ \left(k_z^2 - k_x^2\right) k_y \\ \left(k_x^2 - k_y^2\right) k_z \end{pmatrix} \tag{2.19}$$

is the frequency at which an electron spin processes along the internal magnetic field. The approximation

$$\alpha = 4\gamma/\sqrt{3-\gamma}(m_c/m) \tag{2.20}$$

is found in literature [Son02], where γ is – as in section 2.3 – defined as $\gamma = \Delta/(\Delta + E_g)$. In the motional narrowing regime, the spin-relaxation rate can be calculated according to

$$\left(\frac{1}{\tau_s(E_{\boldsymbol{k}})}\right)_{DP} = q\alpha^2 \frac{E_{\boldsymbol{k}}^3}{\hbar^2 E_g} \tau_p(E_{\boldsymbol{k}}) \tag{2.21}$$

with the momentum relaxation time $\tau_p(E_{\boldsymbol{k}})$ for an electron with kinetic energy $E_{\boldsymbol{k}}$. q is a dimensionless factor, that depends on the dominant momentum scattering mechanism. The DP mechanism often dominates electron spin relaxation in III-V semiconductors [Jia09b].

Bir-Aronov-Pikus relaxation Another reason for spin relaxation is the exchange scattering of an electron with a hole [Bir76, Aro83]. The interaction Hamiltonian $\mathscr{H}_{eh} \propto \boldsymbol{S} \cdot \boldsymbol{J} \delta(\boldsymbol{r})$ is proportional to the product of electron spin $\boldsymbol{S}$ and hole angular momentum $\boldsymbol{J}$, provided that electron and hole are located at the same position $\boldsymbol{r}$. In some cases, electron-hole exchange scattering dominates electron spin relaxation in strongly p-doped III-V semiconductors at low temperatures [Mei84, Jia09b].

Hyperfine and anisotropic exchange interaction At low temperatures and donor concentrations, electrons may be localised at donor states. Electron spin relaxation is then driven by hyperfine interaction of the electron spins with surrounding nuclear spins, and – in inversion-asymmetric materials – by the interaction of two electrons localised at a pair of donor states. Following [Kav01], the latter contains an anisotropic contribution as a result of spin-orbit interaction. This means that a site interchange of the two electrons comes along with a diametrical rotation of the spin states by a certain angle β. In addition, the isotropic part of the exchange interaction, that is a factor of β^{-1} stronger than the anisotropic part, causes site interchanges accompanied by diametrical reversion – or flip-flop – of the involved spin states. Such flip-flop processes motionally narrow electron spin dephasing due to the anisotropic exchange interaction. With the time constant for the flip-flop processes denoted τ_c, the electron ensemble spin therefore relaxes within

$$\frac{1}{\tau_{s,A}} = \frac{2}{3}\beta^2\tau_c^{-1}.$$

The correlation time τ_c decreases exponentially with increasing donor distance [Dzh02], and, at sufficiently low donor concentrations, hyperfine interaction dominates electron spin relaxation.

The corresponding Hamiltonian is $\mathscr{H}_{hf} \propto \sum_i g_{n,i}\boldsymbol{S}\cdot\boldsymbol{I}_i\delta(\boldsymbol{r}-\boldsymbol{R}_i)$. Each localised electron spin $\boldsymbol{S}$ typically sees an effective magnetic field generated by $\sim 10^5$ nuclear spins $\boldsymbol{I}_i$. $g_{n,i}$ is the nuclear Landé factor. Spatial as well as temporal fluctuations of the effective nuclear magnetic field lead to relaxation of the electron spin ensemble. The resulting spin relaxation time at zero external magnetic field is

$$\frac{1}{\tau_{s,N}} = \frac{2}{3}\left\langle \omega_N^2 \right\rangle \tau_c.$$

Here, ω_N denotes the frequency at which an electron spin precesses along the effective nuclear magnetic field.

2.4 Optical readout of carrier spins

An optically induced spin polarisation changes the optical properties of the material under consideration. In particular, the polarisation state of linearly polarised light is rotated and/or changed to elliptical upon transmitting a sample with macroscopic magnetic moment $\boldsymbol{M}$. These effects known as Faraday rotation and ellipticity are phenomenologically understood in the common description of light-matter interaction based on the Maxwell equations

$$\begin{aligned} \nabla\times\boldsymbol{E} &= -\mu_0\frac{\partial\boldsymbol{H}}{\partial t}, \\ \nabla\times\boldsymbol{H} &= \varepsilon_0\boldsymbol{\varepsilon}\frac{\partial\boldsymbol{E}}{\partial t}, \end{aligned} \tag{2.22}$$

where $\boldsymbol{E}$ is the light wave's electric and $\boldsymbol{H}$ its magnetic-field vector. The vacuum permeability and permittivity are denoted ε_0 and μ_0, respectively. The Maxwell equations (2.22) assume $\boldsymbol{\mu} = \mu_0\mathbf{1}$ since the impact of the magnetic permeability tensor $\boldsymbol{\mu}$ on light-matter interaction is usually small. The dielectric permeability tensor $\boldsymbol{\varepsilon}$ depends on the light angular frequency ω, and on $\boldsymbol{M}$. It is defined by the material function $\boldsymbol{D} = \varepsilon_0\boldsymbol{\varepsilon}(\omega,\boldsymbol{M})\cdot\boldsymbol{E}$, where $\boldsymbol{D}$ is the dielectric displacement vector. In a cubic crystal without macroscopic magnetic moment the dielectric tensor is isotropic. However, a macroscopic magnetisation reduces the cubic symmetry. Specifically, for $\boldsymbol{M} = (0,0,M_z)^T$ the dielectric tensor is of the form

$$\boldsymbol{\varepsilon}(\omega,\boldsymbol{M}) = \begin{pmatrix} \varepsilon_{xx} & \varepsilon_{xy} & 0 \\ -\varepsilon_{xy} & \varepsilon_{xx} & 0 \\ 0 & 0 & \varepsilon_{zz} \end{pmatrix}, \tag{2.23}$$

where the $\varepsilon_{ij} = \varepsilon'_{ij} + i\varepsilon''_{ij}$ are generally complex. For a plane wave with frequency ω and wave vector $\boldsymbol{k}$ characterised by $\boldsymbol{E} = \boldsymbol{E}_0\exp\left[-i\left(\omega t - \boldsymbol{k}\cdot\boldsymbol{r}\right)\right]$ and $\boldsymbol{H} = \boldsymbol{H}_0\exp\left[-i\left(\omega t - \boldsymbol{k}\cdot\boldsymbol{r}\right)\right]$ the Maxwell

equations (2.22) read[5]

$$\begin{aligned} \boldsymbol{k}\times\boldsymbol{E} &= \omega\mu_0\boldsymbol{H}, \\ \boldsymbol{k}\times\boldsymbol{H} &= -\omega\varepsilon_0\boldsymbol{\varepsilon}\cdot\boldsymbol{E}. \end{aligned}$$

With $\boldsymbol{k}\times(\boldsymbol{k}\times\boldsymbol{E}) = \boldsymbol{k}\cdot\left(\boldsymbol{k}\cdot\boldsymbol{E}-k^2\boldsymbol{E}\right)$, the light wave within the magnetised medium is finally described by

$$\boldsymbol{k}\cdot\left(\boldsymbol{k}\cdot\boldsymbol{E}-k^2\boldsymbol{E}\right)+\varepsilon_0\mu_0\omega^2\boldsymbol{\varepsilon}\cdot\boldsymbol{E},$$

or specifically for light propagating in z-direction – and defining $\boldsymbol{N} = \left(\varepsilon_0\mu_0\omega^2\right)^{-1}\boldsymbol{k}$ – by

$$\begin{aligned} &\left(N^2-\varepsilon_{xx}\right)E_x-\varepsilon_{xy}E_y = 0, \\ &\varepsilon_{xy}E_x+\left(N^2-\varepsilon_{xx}\right)E_y = 0. \end{aligned} \tag{2.24}$$

The normal modes solving equations (2.24) are the right- and left-circularly polarised waves

$$D_\pm = \varepsilon_0 N_\pm^2\left(E_x \pm iE_y\right)$$

with $E_y = \pm iE_x$. The complex indices of refraction $N_\pm = n_\pm + ik_\pm$ for the circularly polarised partial waves are determined by $N_\pm^2 = \varepsilon_{xx}\pm i\varepsilon_{xy}$. Accordingly, the polarisation plane of linearly polarised light is – per unit length of propagation through the magnetised material – rotated by the Faraday rotation angle

$$\theta_F(\omega,\boldsymbol{M}) \propto \mathrm{Re}(N_+ - N_-),$$

if the real parts of $N_\pm$ differ, or if, in other words, the magnetisation induces circular birefringence. For different imaginary parts of $N_\pm$ – i.e. magnetisation-induced circular dichroism – incident linearly polarised light gets elliptically polarised. The Faraday ellipticity per unit length is

$$\eta_F(\omega,\boldsymbol{M}) \propto -\mathrm{Im}(N_+ - N_-).$$

In polarisation-resolved pump-probe investigations, the dynamics of carrier spins, that are induced by circularly polarised pump pulses, is detected via the transient change of the polarisation state of linearly polarised probe pulses. Carrier spin dynamics in semiconductors is in generally mapped in both transient Faraday rotation and ellipticity (in transmission measurements), or in the corresponding Kerr rotation and ellipticity in reflection (cf. [Gla12, and references therein]). Figure 2.4 summarises the physical principles which govern such investigations (for experimental details refer to chapter 3). Circularly polarised pump pulses induce a spin-polarised carrier distribution that is associated with a macroscopic magnetic moment (cf. section 2.2). The polarisation states of the probe pulses before and after transmission through the sample is depicted in terms of circularly polarised basis states $\boldsymbol{E}^\pm = [\boldsymbol{x}\pm i\exp(i\varphi)\boldsymbol{y})]E_0\exp[i(\boldsymbol{k}\cdot\boldsymbol{r}-\omega t)]$. According

[5] A this point, the identities $\nabla\times\boldsymbol{E} = i\boldsymbol{k}\times\boldsymbol{E}$, $\nabla\times\boldsymbol{H} = i\boldsymbol{k}\times\boldsymbol{H}$ and $\partial\boldsymbol{E}/\partial t = -i\omega\boldsymbol{E}$, $\partial\boldsymbol{H}/\partial t = -i\omega\boldsymbol{H}$ are used.

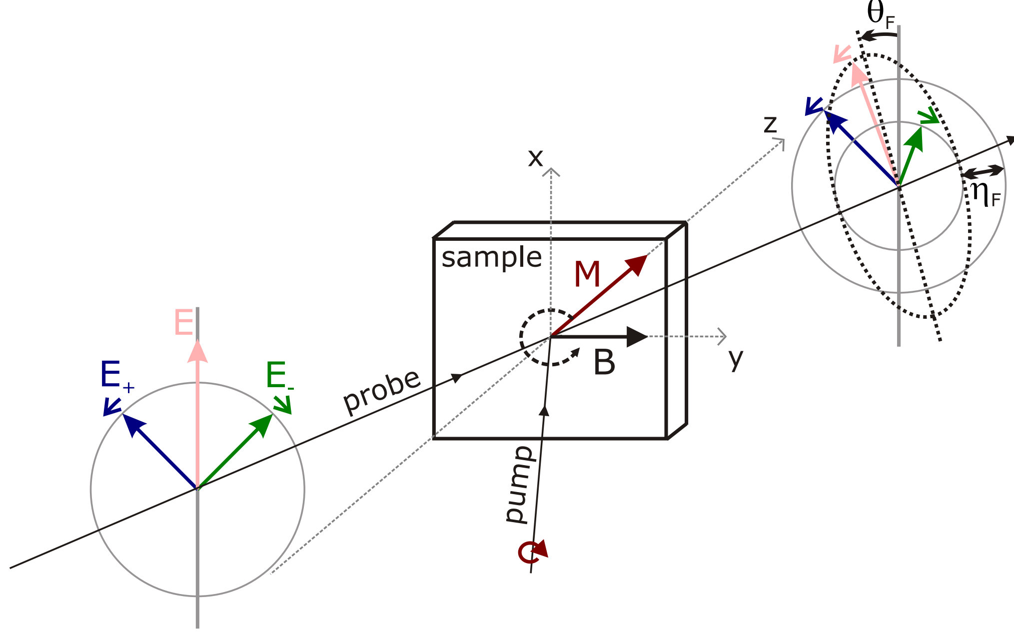

FIGURE 2.4 *Time-resolved magneto-optics. The polarisation states of incident and transmitted probe pulses is illustrated following [Sug00]). Furthermore depicted are the magnetisation that is associated with the pump-induced carrier spin polarisation, and the in-plane magnetic field along which **M** precesses. (The impact of coherent spin precession on the polarisation state of the transmitted probe pulses is not shown).*

to the Faraday effect, linearly polarised incident probe pulses ($\varphi = \pm\pi/2$, $E^+ = E^-$) are rotated ($\varphi \neq \pm\pi/2$) and accumulate ellipticity ($E^+ \neq E^-$) proportional to the pump-induced carrier spin polarisation. The magnitude of $\boldsymbol{M}$ is reduced when the optically induced spin polarisation looses coherence, while precession in an external magnetic field, that is oriented in the sample plane, periodically alters the projection of $\boldsymbol{M}$ onto the z-direction (cf. section 2.3). Carrier spin dynamics is thus mapped in the transient Faraday rotation

$$FR(t) = A \times \exp\left(-t/\tau_s\right) \times \cos\left[(\omega_L) \times t\right] \tag{2.25}$$

when scanning the time delay between pump and probe pulses. Equation (2.25) is true if only one spin-carrying species contributes to the Faraday rotation signal (with initial signal amplitude A). An analogue relation applies for transient Faraday ellipticity. Carrier spin dynamics can also be probed with circularly polarised pulses. The spin information is then contained in the different optical bleaching signals for co- and counter-circularly polarised pump and probe pulses, that directly maps transient circular dichroism [Bog00]. Many magneto-optical pump-probe investigations of carrier spin dynamics in semiconductors detect Faraday (or Kerr) rotation [Wu10]. On the example of the investigated direct-gap semiconductors, the present work confirms that Faraday rotation and ellipticity (or circular dichroism) yield comparable results for itinerant electrons

(cf. sections 4.1 and 4.2). Left- and right-circularly polarised pump pulses induce inverted signal amplitudes since the initial spin polarisation is oriented either parallel or antiparallel with respect to the propagation direction of light (cf. section 2.2). Linearly polarised pump pulses induce an equal number of spins oriented parallel and antiparallel with respect to the propagation direction of light, and therefore produce no transient magneto-optical signal. As a result of the convolution of – inherently similar – orientation and detection mechanisms, magneto-optical pump-probe spectroscopy is not sensitive to the sign of the effective Landé factor. Its absolute value is, however, mapped in the precession frequency ω_L according to equation (2.3).

3 Experimental setup and measuring technique

The thesis at hand investigates carrier spin dynamics via (i) time-resolved circular dichroism (CD) and (ii) time-resolved Faraday rotation and/or ellipticity (FR/FE) both of which are widely used measuring techniques [Wu10, and references therein][1]. This chapter details the experimental configurations used in the present work including laser sources, optical setup and signal processing (section 3.1). Section 3.2 gives an overview over the equipment for magnetic field and temperature control.

3.1 Magneto-optical pump-probe setup

Figure 3.1 depicts a schematic representation of the optical setup. The upper panel shows the beam guidance from the laser source towards the sample, while the lower panels illustrate the optical setups to detect either FR and/or FE or CD.

Laser sources Two commercially available laser sources are used, that is a Toptica FFS and a Coherent RegA/OPA system. Considering the Toptica FFS both the passively mode-locked resonator and the amplifier are based on optical fibres. In particular, the active media are Er^{3+}-doped ones. Pump and laser transition energies correspond to 980 nm – delivered by a laser diode – and 1550 nm, respectively. Laser pulses are formed via polarisation additive pulse mode locking, i.e. exploiting the intensity dependence of the polarisation rotation of elliptically polarised light that occurs at high power densities. The pulses are further amplified and guided through a silicon prism compressor to achieve an average laser intensity of $I_{out} = 250\,\text{mW}$ and pulse durations τ_p in the range of 100 fs. The Coherent RegA/OPA system contains a Kerr-lens mode-locked titanium-sapphire ($Ti{:}Al_2O_3$) oscillator (Micra-18) with integrated pump laser (Verdi V-18), a regenerative amplifier (RegA 9040) with external grating stretcher/compressor and an optical parametric amplifier (OPA 9850). The frequency-doubled $Nd{:}YVO_4$ pump laser delivers 18 W optical power at a wavelength of 532 nm. 5 W of the Verdi power are used to pump the titanium-sapphire oscillator. The average power of the Micra is typically 400 mW at a repetition rate of 80 MHz. Pulse duration and central wavelength are 40 fs and 800 nm, respectively. The remaining Verdi power generates population inversion in the gain medium of the amplifier, that is again $Ti{:}Al_2O_3$. An acousto-optical Q-switch suppresses lasing until a Micra seed pulse is injected to the amplifier cavity. To prevent damage, the seed pulses are stretched prior to injection by an acousto-optic

[1] In particular, a comprehensive description of the time-resolved FR technique is given in [Cro95].

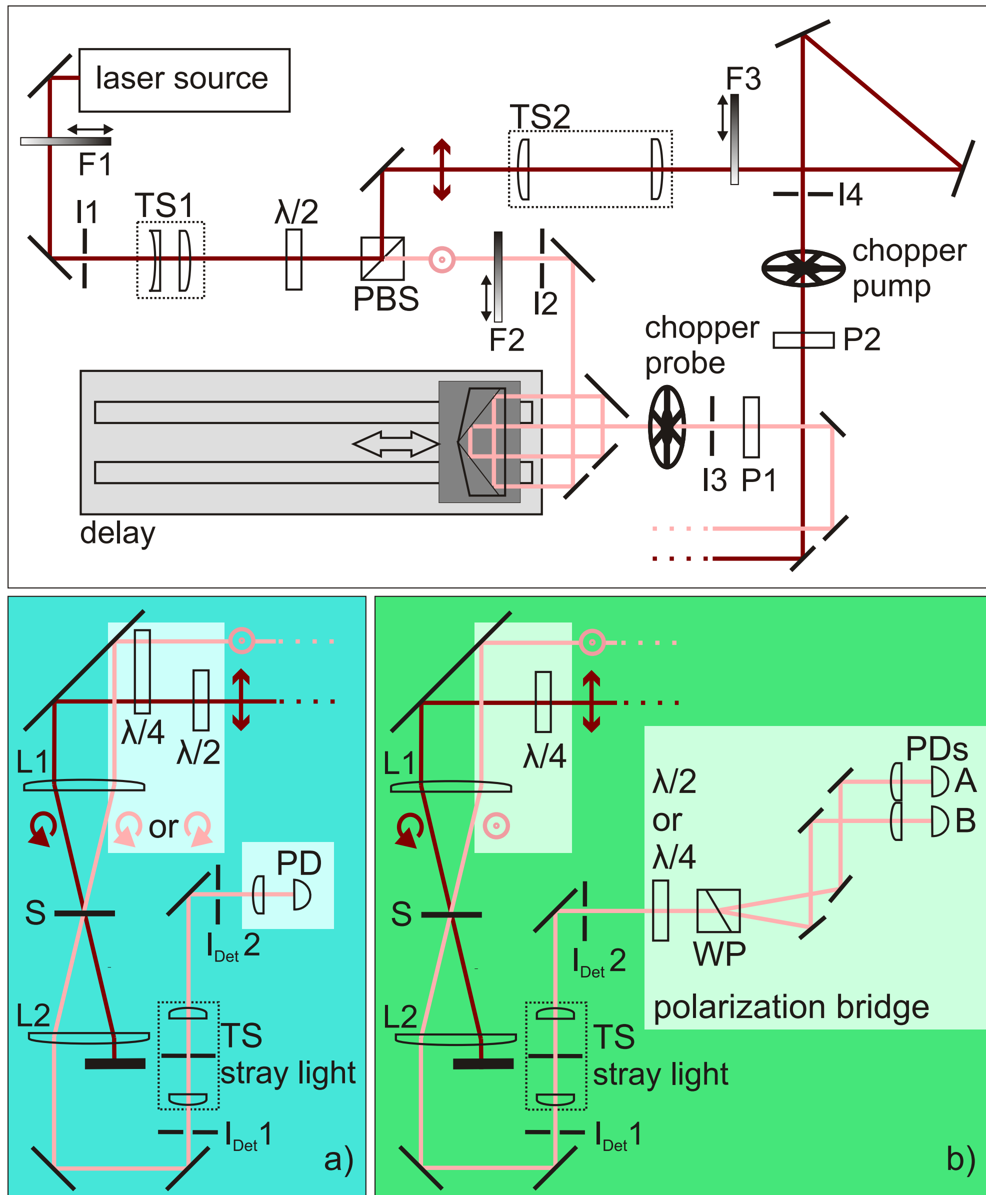

FIGURE 3.1 *Optical setup. Upper panel: Pump (dark red) and probe (light red) beam are separated via half-wave plate ($\lambda/2$) and polarising beam splitter cube (PBS). The probe continues along a delay line, pump and probe are guided through chopper wheels. Lower panels: Beam guidance to the sample (S) and detection arms for (a) Faraday rotation (FR) or ellipticity (FE), or (b) circular dichroism (CD). FR and FE are detected via a polarisation bridge consisting of a half- or a quarter-wave plate ($\lambda/4$), a Wollaston prism (WP) and two photodiodes (PD). When impinging the sample, pump and probe pulses are circularly and linearly polarised, respectively. For CD pump and probe pulses are co- or counter-circularly polarised, a photodiode detects the optical bleaching signals. Polarisation states are indicated as colour-coded arrows. Additional denoted components are telescopes (TS), polarisers (P), neutral density filters (F), irises (I) and lenses (L).*

cavity dumper. A single seed pulse is subsequently amplified passing the gain medium typically 20 times before it is ejected by the cavity dumper (a Faraday isolator is included to separate incoming and outgoing pulse trains). Both cavity dumper and Q-switch are SiO_2 crystals. The amplified pulses are recompressed to a pulse duration of 40 fs. The average output power of the RegA is 1.7 W at a repetition rate of 250 kHz[2]. Finally, the RegA delivers femtosecond pulses centred at 800 nm with a pulse energy that exceeds that of the seed pulses by a factor of $(1.7\,\mathrm{W}/250\,\mathrm{kHz})/(400\,\mathrm{mW}/80\,\mathrm{MHz}) = 6.8\,\mu\mathrm{J}/5.5\,\mathrm{nJ} \sim 1000$. Typically, 70 % of the RegA power are used to operate the OPA. Part of the input is focussed on a sapphire window to generate a white light continuum via self-focussing and self-phase modulation. The input remainder is overlapped with the continuum in a β-BaB_2O_4 (BBO) crystal. In the non-linear crystal, optical parametric amplification takes place, i.e. a signal wavelength within the continuum is amplified via difference frequency generation. Momentum conservation – or phase matching – can be realised for signal wavelengths ranging from $(1250-1600)$ nm by adjusting the BBO orientation. For reasons of energy conservation idler photons are generated in the amplification process. Since the photon energy of the pump photons corresponds to 800 nm, the photon energy of the idler photons corresponds to $(2400-1600)$ nm in accordance with the signal wavelengths specified above. The idler output is, however, not relevant for the measurements discussed in the present thesis. In most of the measurements the signal output of the OPA is used exclusively (only in one case the remainder of the RegA input power – that leaves the OPA as a third output beam – serves as a pump). Specifically, the central wavelength of the OPA is tuned between 1350 nm and 1570 nm. Output parameters of the OPA and the fibre laser are summarised in table 3.1.

	Toptica FFS	Coherent RegA/OPA OPA output
I_{out}	250 mW	$(40-50)$ mW
f_{rep}	90.5 MHz	250 kHz
E_p	2.8 nJ	0.2 μJ
τ_p	80 fs	60 fs
$\hbar\omega$	0.80 eV	$(0.79-0.92)$ eV
FWHM	25 meV	40 meV

TABLE 3.1 *Output parameters – average power, repetition rate, central photon energy, energy per pulse, pulse duration and spectral width (full-width-half-maximum) – of the laser sources.*

Pump, probe and delay The laser beam is guided through a telescope (TS1) to minimise beam divergence and adjust the beam diameter. The beam is then divided into a pump and a probe beam

[2] In principle, f_{rep} is tunable from 50 kHz to 300 kHz. All present measurements that rely on the RegA/OPA system are conducted with 250 kHz.

via a half-wave plate ($\lambda/2$) and a polarising beam splitter cube (PBS). Thus, the intensity ratio of pump and probe is adjustable, and the beams are polarised perpendicular to each other. Typically, the probe intensity is chosen to be $\lesssim 1/10$ of the pump intensity. The absolute intensities of pump and probe can additionally be tuned by continuously variable neutral density filters (F1 to F3). A delay stage driven by a stepper motor induces time delay between pump and probe pulses. The total length is 300 mm or – with $c = 3 \times 10^8\,\mathrm{m/s}$ – 2 ns for single pass. To access longer delay times, and as is shown in figure 3.1, the probe is aligned to pass the delay line twice corresponding to a total delay length of 4 ns. The minimal step width of the delay stage is $0.2\,\mu$m, or a few femtoseconds, which is more than an order of magnitude shorter than the pulse duration. The irises (I1 to I4) facilitate beam alignment and – in case the RegA/OPA system serves as laser source – block unpolarised and locally separated parts of the laser output. Linear polarisers (P1 and P2) further improve the polarisation degree and transform polarisation noise to intensity noise, the latter of which is effectively suppressed in FR/FE measurements through the use of a polarisation bridge.

Spot sizes and optically induced carrier density The pump spot size is reduced via telescope T2 so that it exceeds the probe spot size at the location of pump-probe overlap in the sample plane. Such a configuration assures that the pump-probe signal is not altered by minor variations of (i) the probe position within the sample plane (due to deviations from straight alignment along the delay line) and/or (ii) the probe spot size (due to beam divergence), while scanning the delay. Moreover, the probed in-plane optically induced carrier density is the more homogeneous the higher the ratio r_{pump}/r_{probe}. Satisfying conditions are achieved using a lens with focal length of $f = -75$ mm and one with $f = 100$ mm for T1, while T2 consists of a $f = 100$ mm and a $f = 60$ mm lens. (The order of the lenses is given in propagation direction. The concave lens in T1 is chosen to safe space.) Typical parameters with the OPA tuned to a central wavelength of 1500 nm are the following. The focal radii of pump and probe are $80\,\mu$m and $55\,\mu$m, respectively, when focussed onto the sample plane with a $f = 150$ mm lens (L1). The spot size of the probe is constant over the delay line within the $5\,\mu$m accuracy of spot size determination using a razor blade[3]. The conditions depend on the focal length of L1 – that is between 75 mm and 150 mm, adapted to the dimensions of the respective cryostat – as well as on the laser source and/or the central wavelength. In particular, the divergence of the fibre laser output is larger than that of the OPA and can not be compensated as well. However, the fibre laser is used to determine comparably short-lived dynamics up to 100 ps, where the change in the probe spot size over the measured delay is $\leq 10\,\%$.

To estimate optically induced carrier densities n_{opt} the number of absorbed photons per sample volume is integrated numerically over the propagation length within the sample z and the spectral

[3]The specified spot radii correspond to the $1/e^2$ width of a Gaussian intensity distribution. For a detailed description of spot size determination refer to [Eic04].

shape $I(\lambda)$ of the excitation pulses

$$n_{opt} = \frac{1}{V}\int dz \int d\lambda \frac{I(\lambda)}{f_{rep} \times \hbar\omega(\lambda)} \times A(z,\lambda). \tag{3.1}$$

The spectral intensity

$$I(\lambda) = I_{eff} \exp\left[-4\ln 2\left(\frac{\lambda-\lambda_c}{\Delta\lambda}\right)^2\right] / \int \exp\left[-4\ln 2\left(\frac{\lambda-\lambda_c}{\Delta\lambda}\right)^2\right]$$

is calculated for a Gaussian pulse. Full-width-half-maximum and central wavelength are denoted $\Delta\lambda$ and λ_c, respectively. I_{eff} corresponds to the average incoming intensity I_0 corrected for reflection losses at the sample surface (that specifically are $(30-40)\,\%$ for the investigated semiconductors) and at the cryostat window(s) (4 % per window). $A(z,\lambda) = \alpha(\lambda)\exp[-\alpha(\lambda)z]$ denotes the relative absorption. Wavelength (and temperature) dependence of the absorption coefficient $\alpha(\lambda)$ are taken into account according to [Ghe95] for GaSb, [Zie86] for $In_{0.53}Ga_{0.47}As$ and [Mac57, Sei69][4] for Ge. The sample volume excited by the laser pulses is $V = z \times \pi r^2$. Note that in case of optically thick samples the carrier density is noticeably inhomogeneous over the propagation length within the sample. This is shown in figure 3.2 for a 1.5 mm thick Ge sample at $T \lesssim 100\,\mathrm{K}$. The figure depicts the optically induced carrier density per mW (with respect to I_0) as a function of z, comparing excitation predominantly across the indirect ($\lambda_c = 1505\,\mathrm{nm}$ or $\hbar\omega = 0.82\,\mathrm{eV}$) to excitation predominantly across the direct bandgap ($\lambda_c = 1360\,\mathrm{nm}$ or $\hbar\omega = 0.91\,\mathrm{eV}$) (for details concerning the excitation conditions cf. section 5.1). The $1/e$-penetration depth of the central wavelength is $z_p = 0.5\,\mathrm{mm}$ for excitation across the indirect bandgap but only $z_p = 2\,\mu\mathrm{m}$ for excitation across the direct bandgap. To specify comparable values, the n_{opt} in the further course of the present work are peak densities. Especially with respect to penetration depths of the order of 1 mm it is worth mentioning that the Rayleigh lengths[5] that correspond to the pump and probe parameters specified above are approximately 15 mm and 8 mm, respectively. Such values justify the assumption of a constant spot size in equation (3.1).

Stray light suppression The transmitted probe is collected via L2 (that is of the same focal length as L1) while the transmitted pump is blocked at this place. The collected probe is guided through a telescope with a pinhole in its focal plane to reduce stray light stemming from the pump. The telescope lenses have a focal length of 50 mm and typically a 200 μm pinhole is used.

Lock-in detection The transmitted probe is focussed onto one or two $In_{0.53}Ga_{0.47}As$ photodiodes (FG10, Thorlabs) to detect FR/FE or CD. The photodiodes are operated in reverse bias and the probe-induced photocurrent is converted to a measuring voltage by a resistance. Measuring

[4] The respective data is accessible on [Iof].

[5] The Rayleigh length is the length over which the spot sizes do not exceed $\sqrt{2} \times r$ where r is the focus radius.

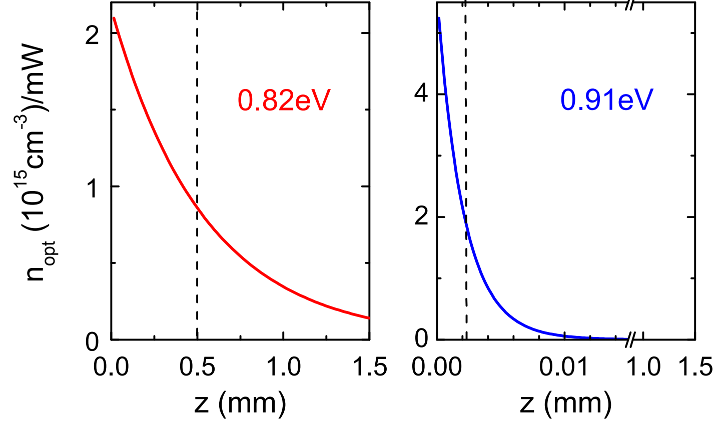

FIGURE 3.2 *Optically induced carrier density per* mW *average laser power as a function of propagation length in Ge at low temperatures. Left-hand side: excitation predominantly across the indirect bandgap (pulses centred at* 0.82 eV*). Right-hand side: excitation across the direct bandgap (pulses centred at* 0.91 eV*). The dashed lines indicate the respective* $1/e$*-penetration depths.*

resistances between 10 kΩ and 100 kΩ are used depending on the sample's transparency. The voltage drop at the measuring resistance is recorded relying on a lock-in amplifier (SR830, Stanford Research Systems) referenced to on-off modulation of the pump beam. The pump beam is modulated at a few kHz by a chopper wheel – which applies to most of the measurements – or using an acousto-optical modulator (MGAS-110, EOPC)[6]. The lock-in amplifier thus measures the transmission change induced by the pump pulses $\Delta T = T_{\text{pump}} - T$ (T_{pump} and T are the transmissions with and without pump, respectively). The carrier spin signals discussed in the present thesis are – unless stated otherwise – presented according to the widely used normalized differential transmission $\Delta T/T = (T_{\text{pump}} - T)/T$.

Circular dichroism Figure 3.1 (a) illustrates the beam guidance for CD measurements. Both pump and probe pass the same quarter-wave plate. Co- and counter-circularly polarised pump-probe configurations are realised with an additional half-wave plate in the pump. The pump-induced spin polarisation is contained in the difference of co- and counter-circular optical bleaching signals $(\Delta T/T)_{co} - (\Delta T/T)_{counter}$ considering that the optically induced spin polarisation is $< 100\,\%$ (cf. section 2.2).

Faraday rotation or ellipticity The beam guidance to detect pump-induced FR or FE of an incident linearly polarised probe is shown in figure 3.1 (b). The transmitted probe passes a polarisation bridge that consists of a half- or a quarter-wave plate to detect FR or FE, respectively, and

[6] In some cases, the signal is measured in a double lock-in scheme where not only the pump but also the probe is chopped. The chopping frequency of the probe is a few tens of Hz. Since the overall signal output is locked to both pump and probe chopping frequencies such a double lock-in scheme may further reduce stray light.

a Wollaston prism. The latter separates two orthogonal linearly polarised beams. To balance the polarisation bridge the pump is blocked and the probe transmitted through the sample is evenly distributed to the photodiodes denoted A and B. For precise balancing the probe is chopped, and the transmission signals are measured with the lock-in amplifier. The wave plate used for balancing is mounted in a rotation mount with angular precision of 5 arcmin. With this scheme, the polarisation bridge is typically balanced down to the noise level. When the polarisation bridge is balanced, the pump-induced spin polarisation manifests in $(\Delta T_A - \Delta T_B)/T$. Compared to CD measurements, the advantage of FR/FE measurements is that fluctuations in the laser intensity are cancelled via the polarisation bridge. As a result, FR or FE measurements in principle offer the potential for shot noise limited detection. Some sources of noise in magneto-optical pump probe measurements are well predictable. These are input noise of the Lock-in amplifier, thermal noise of the measuring resistances, shot noise related with the dark current of the photodiodes, and photon shot noise of the probe light. According to manufacturer's data, the input noise of the Lock-in amplifier is typically $6\,\mathrm{nV}/\sqrt{\mathrm{Hz}}$. The contributions from the remaining noise sources are estimated in the following for typical values of measuring resistance $R = 10\,\mathrm{k}\Omega$ and measuring voltage $U_{PD} = 0.1\,\mathrm{V}$. The thermal noise of the $10\,\mathrm{k}\Omega$ measuring resistance at room temperature is

$$\begin{aligned} \frac{\Delta U_T}{\sqrt{Hz}} &= \sqrt{4k_B T R} \\ &= \sqrt{4 \times (1.38 \times 10^{-23}\,\mathrm{J/K}) \times 300\,\mathrm{K} \times 10\,\mathrm{k}\Omega} = 13\,\mathrm{nV}/\sqrt{\mathrm{Hz}} \end{aligned}$$

The shot noise related with the dark current of the photodiode is

$$\begin{aligned} \frac{\Delta U_{S\ dark}}{\sqrt{Hz}} &= R\sqrt{2eI_0} \\ &= 10\,\mathrm{k}\Omega\sqrt{2 \times (1.6022 \times 10^{-19}\,\mathrm{C}) \times 25\,\mathrm{nA}} = 1\,\mathrm{nV}/\sqrt{\mathrm{Hz}}, \end{aligned}$$

where the dark current of $I_0 = 25\,\mathrm{nA}$ is specified by the manufacturer at a reverse bias of 5 V. The photon shot noise is calculated as

$$\begin{aligned} \frac{\Delta U_{S\ phot}}{\sqrt{Hz}} &= \sqrt{2eU_{PD}R} \\ &= \sqrt{2 \times (1.6022 \times 10^{-19}\,\mathrm{C}) \times 0.1\,\mathrm{V} \times 10\,\mathrm{k}\Omega} = 18\,\mathrm{nV}/\sqrt{\mathrm{Hz}}. \end{aligned}$$

From the estimations above, the dominant noise sources are thermal noise of the measuring resistance and photon shot noise. The total noise is roughly $20\,\mathrm{nV}/\sqrt{Hz}$ corresponding to a

$$\frac{20\,\mathrm{nV}/U_{PD}}{\sqrt{Hz}} = \frac{20\,\mathrm{nV}/0.1\,\mathrm{V}}{0.88\,\mathrm{Hz}} = 2 \times 10^{-7}$$

relative noise level with an integration time of 0.1 s (or an equivalent noise bandwidth of 0.88 Hz with the commonly used Lock-in filter settings). The typical apparent noise in the FR/FE transients of the present study is 1×10^{-6}, which exceeds the theoretical limit by nearly an order of magnitude. However, the above estimation of the relative noise level does not take into account additional sources of noise in a real experiment, such as current noise of the measuring resistance, noise induced by vacuum- and/or helium pumps and pump-induced noise. Both the presence of pump photons as well as the chopping of the pump may induce additional noise. Yet, the polarisation bridge significantly reduces the apparent noise level. Typically, the apparent noise in a single detector signal exceeds the apparent noise in a FR/FE transient by a factor of 5 when the fibre laser is used as a laser source (cf. section 4.1.1). In measurements that rely on the OPA, the improvement is even a factor of $10-20$. Such an improvement is indeed relevant in view of signal amplitudes down to a few 10^{-4} in section 4.2 and chapter 5.

3.2 Temperature and magnetic field control

The samples are kept at temperatures between 3 K and room temperature and/or exposed to – if not explicitly stated otherwise – in-plane magnetic fields. To this end various optical cryostats, magnets and/or combinations are used. Table 3.2 gives an overview over the respective configurations including maximal obtainable magnetic field B_{max} and field uncertainty ΔB (which in case of the split-pair magnet corresponds to the manufacturer specification for the magnetic field homogeneity within the sample volume).

	cryostat type	magnetic field		
		type	B_{max} (T)	ΔB (%)
–	–	electromagnet Siemens	1	1
Microstat® He Oxford Instruments	continuous flow	–	–	–
Microstat® He Rectangular Tail Oxford Instruments	continuous flow	external electromagnet GMW	~ 0.7	1
He-Bath-Cryostat-Spektro CryoVac	bath			
Spectromag® Oxford Instruments	bath	integrated split-pair	7	0.6

Table 3.2 *Devices for temperature and/or magnetic field control.*

4 Electron spin dynamics in the direct-gap semiconductors gallium antimonide and indium gallium arsenide

The present chapter is dedicated to electron spin dynamics in selected direct-gap (bulk) semiconductors, specifically GaSb (section 4.1) and $In_{0.53}Ga_{0.47}As$ (section 4.2). GaSb is chosen to investigate electron spin dynamics under comparatively strong spin-orbit coupling. Indeed, the spin-orbit splitting of the valence band is comparable to the fundamental bandgap. In contrast, $\Delta_{SO} = 1/2E_g$ in $In_{0.53}Ga_{0.47}As$ and $\Delta_{SO} = 1/5E_g$ in the prototypical GaAs. In general, the strength of spin-orbit coupling crucially influences carrier spin relaxation in semiconductors without inversion center (cf. [Wu10] and section 2.3). As an example, the inherently strong spin-orbit interaction for holes was predicted [Kra08] and experimentally shown [Hil02] to induce complex sub-picosecond dynamics of hole spins in GaAs. The present study of GaSb – as a model system for strong spin-orbit coupling – and $In_{0.53}Ga_{0.47}As$ is well suited to examine the impact of spin-orbit coupling on electron spin relaxation. Except for the strength of spin-orbit interaction, the relevant band parameters of both semiconductors are comparable (cf. table 2.2). Beyond that, electron spin dynamics in $In_{0.53}Ga_{0.47}As$ is intriguing in consideration of reports on electron spin coherence times as long as $(100-200)$ ns in n-type GaAs [Kik98, Dzh02]. Such long-lived spin coherence is related to donor-bound electron spins, that relax via hyperfine- or anisotropic exchange interaction. Furthermore, $In_{0.53}Ga_{0.47}As$ is a promising candidate for room temperature applications. As in GaAs, the D'yakonov-Perel' mechanism is expected to dominate spin relaxation in the ambient temperature range, and coherence times in the same order of magnitude are anticipated [Son02]. Yet, the effective Landé factor for conduction band electrons in $In_{0.53}Ga_{0.47}As$ is approximately an order of magnitude higher than in GaAs [Zaw08], so that coherent electron spin precession should be detectable at lower magnetic fields. In addition, the bandgap energies of both GaSb and $In_{0.53}Ga_{0.47}As$ are favourable for applications in the telecom wavelength band around $1.55\,\mu$m. Up to now, no magneto-optical pump probe analysis of electron spin dynamics in this wavelength range has been reported, despite the potential importance in view of future device applications.

4.1 Gallium antimonide – GaSb

The section starts with some details on sample preparation and experimental configurations, followed by a discussion of the samples' electronic properties and room temperature transmission. The results on electron spin dynamics in GaSb are presented in four sections. Section 4.1.1 compares detection relying on either circular dichroism or Faraday rotation to each other. The influence of temperature, doping concentration and optically induced carrier density is investigated in sections 4.1.2 and 4.1.3. Finally, the effective Landé factor is extracted from electron spin precession in in-plane magnetic fields (section 4.1.4). Parts of the results on electron spin dynamics in GaSb have been published as [Hau09].

Samples and experimental details The GaSb samples are provided by Professor Amanns group at the Walter Schottky Institute[1]. Using molecular beam epitaxy, 1 μm thick bulk GaSb layers are grown on intrinsic GaAs substrates. To reduce the density of dislocations related to the lattice mismatch of approximately 7 % – the lattice constants are $a_{GaAs} = 5.65$ Å and $a_{GaSb} = 6.10$ Å [Iof] – a GaSb/AlSb superlattice is grown prior to deposition of GaSb. Time-resolved spin dynamics is investigated in three samples. As laid out below, two of them are doped with Te, one is nominally undoped. In preparation for the time-resolved transmission measurements, the sample substrates are thinned to $\sim 100\,\mu$m and optically polished prior to glueing them on Infrasil windows. Both Infrasil as well as the UVN 2000 Statisloh glue are transparent in near-infrared light and not birefringent. The samples are mounted in the Microstat® He cryostat, that is operated between $T = 5$ K and room temperature (sections 4.1.1, 4.1.2 and 4.1.3). The effective Landé factor is determined in a room temperature magneto-optical setup relying on the Siemens electromagnet (section 4.1.4). As a laser source, the Toptica FFS is used. The pump beam is chopped by the EOPC acousto-optic modulator at a frequency of 6 kHz.

Electronic properties The electronic properties at room temperature and $T = 77$ K are determined by Hall measurements in a van-der-Pauw geometry [VdP58]. The resulting Hall mobilities μ_H and carrier concentrations n_H are summarised in table 4.1. The Te-doped samples are n-conductive whereas the nominally undoped specimen reveals residual p-conductivity. According to polarity and, in case of the n-doped specimens, concentration of majority carriers, the samples are in the following referred to as nGaSb17, nGaSb18 and pGaSb. In the n-doped samples, μ_H approximates the electron mobility μ_n, and n_H gives the electron concentration N. The value for N determined at room temperature equals the donor concentration n_D. The rather counterintuitive temperature dependence of N is a result of DX centres [Poo90, Du05]. Such deep donor sites act as deep acceptors at room temperature while behaving as shallow donors at low temperature [Die07]. The determined electron mobilities are in line with literature values for epitaxial n-doped GaSb

[1] Amann group (E26), Walter Schottky Institut der Technischen Universität München, Am Coulombwall 3, D-85748 Garching, http://www.wsi.tum.de/Research/AmanngroupE26/tabid/97/Default.aspx.

room temperature			
sample	dopant	μ_H (cm^2/Vs)	n_H (cm^{-3})
nGaSb17	Te	3500	1.2×10^{17}
nGaSb18	Te	1200	1.5×10^{18}
pGaSb	–	370	4.8×10^{16}

77 K			
sample	dopant	μ_H (cm^2/Vs)	n_H (cm^{-3})
nGaSb17	Te	6400	1.8×10^{17}
nGaSb18	Te	2400	1.7×10^{18}
pGaSb	–	630	1.3×10^{16}

TABLE 4.1 *Hall mobilities μ_H and carrier concentrations n_H at room temperature and liquid nitrogen temperature.*

[Bar96]. Hall mobility and carrier concentration determined for sample pGaSb are dominated by holes as theses are the majority carriers. The electron mobility – which is in fact of relevance for the data interpretation in section 4.1.2 – is expected to be $\sim 10,000\,\text{cm}^2\text{Vs}^{-1}$ at room temperature as well as at $T = 77\,\text{K}$ [Chi95, Bar96], i.e. larger than in moderately n-doped GaSb. Electron mobility and concentration determine two quantities relevant for theoretical estimates of the spin relaxation rate. This is, first, the momentum relaxation time

$$\tau_p = \mu_n m_c / e. \tag{4.1}$$

In addition, the Fermi energy is needed as it approximates the mean kinetic energy of the conduction band electrons in degenerately doped materials. In the Nilsson approximation [Nil73], the Fermi energy relative to the conduction band edge is

$$E_F = k_B T \left(\frac{ln(r)}{1-r} + \left(\frac{3\sqrt{\pi}r}{4} \right)^{2/3} + \frac{8\sqrt{\pi}r}{3(4+\sqrt{\pi}r)^2} \right), \tag{4.2}$$

where $r = N/N_c$ is ratio of the electron concentration in conduction band and the effective density of states N_c

$$N_c = 2\left[m_c k_B T / \left(2\pi\hbar^2\right)\right]^{3/2} \tag{4.3}$$

The τ_p and E_F for the GaSb samples are given in table 4.2.

Room temperature transmission Figure 4.1 shows the room temperature transmission as a function of photon energy. The transmission curves are recorded in a Perkin Elmer Lambda 19 UV/VIS/NIR spectrometer. The transmission reduces in two steps, one between 0.7 eV and 0.8 eV

	room temperature		77 K	
sample	τ_p (s)	E_F (meV)	τ_p (ps)	E_F (meV)
nGaSb17	8×10^{-14}	n.d.	1.4×10^{-13}	30
nGaSb18	3×10^{-14}	112	5.0×10^{-13}	130
pGaSb	2.2×10^{-13}	n.d.	2.7×10^{-13}	n.d.

TABLE 4.2 *Momentum relaxation time τ_p and – in case of degeneracy – Fermi energy E_F. E_F is given relative to the conduction band edge, n.d. means non-degenerate.*

and another at $\sim 1.4\,\text{eV}$. An extended view of the step at higher photon energies is shown in the inset of figure 4.1. This step is associated with the absorption edge of the GaAs substrates and its spectral position is in good agreement with the room temperature bandgap energy of $E_g = 1.42\,\text{eV}$ [Vur01]. The steps at lower photon energy are associated with the GaSb layers. It is not possible to extract the exact spectral positions of the absorption edges since the signals may partly reflect absorption in the superlattices. However, the blue-shifted absorption edge for sample nGaSb18 confirms that the sample is degenerately doped. (The shift is due to the Burstein-Moss effect: if the Fermi level lies above the conduction band edge, the gap between occupied valence band states and unoccupied conduction band states is effectively increased [Bur54, Mos58].)

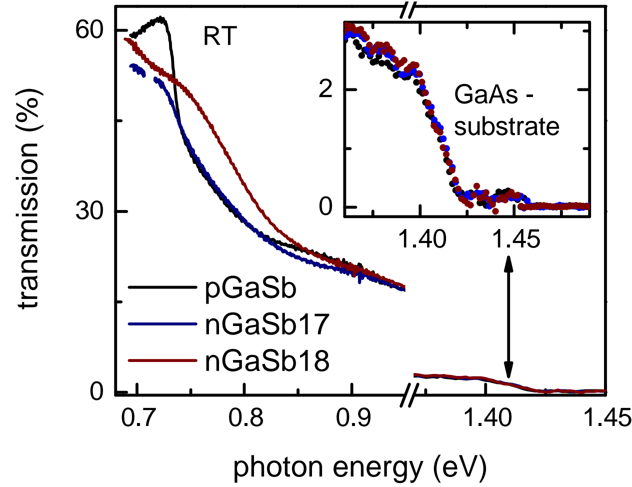

FIGURE 4.1 *Room temperature transmission spectra. The inset shows an extended view of the region around $\hbar\omega = 1.4\,\text{eV}$, where the absorption edge of the GaAs substrate is detected.*

4.1.1 Circular dichroism versus Faraday rotation

The photon energy of the Toptica FFS is in the vicinity of the absorption edges of the investigated samples. However, the electron population is decidedly excited and probed at the band edge only in case of samples pGaSb and nGaSb17 at low temperatures. To check for potential

impact of the specific detection mechanism on the extracted spin relaxation times, the transient spin population is investigated via both CD and FR. Figure 4.2 depicts exemplary data for sample nGaSb17 recorded at $T = 100\,\mathrm{K}$. Panel (a) shows raw data of a measurement probing the transient CD after excitation of spin-polarised carriers. The excitation pulse is σ^+-polarised and generates an electron-hole density of $n_{opt} \sim 1 \times 10^{16}\,\mathrm{cm}^{-3}$. The optical bleaching signal for probe light polarised co-circular with respect to the excitation pulses is depicted as filled circles, while the transient for counter-circular polarised excitation and probe pulses is indicated by open circles. Both optical bleaching signals do not decrease markedly beyond a pump-probe delay of 50 ps. However, the initial difference vanishes for delay times $\gtrsim 30\,\mathrm{ps}$. This indicates that the electron population relaxes considerably slower than the electron spin polarisation. The latter is thus proportional to the difference of the co- and counter-circular pump-probe configurations. If the rates of electron-hole recombination and spin relaxation are comparable, the difference of the two transmission changes have to be divided by their sum to extract correct spin relaxation times [Bog00]. Such transients are referred to as normalized CD. The normalization is particularly important in case of sample pGaSb, as is shown in section 4.1.2. The normalized CD is depicted in figure 4.2 (b) as solid squares. The peak at zero delay time is comparatively broad with respect to the sub-100 fs pulse duration of the fibre laser pulses. However, the AOM considerably extends the pulse duration[2]. Accordingly, both width and decay time of the initial peak are $< 1\,\mathrm{ps}$ for all samples over the whole temperature range under investigation. The second peak at $\sim 2\,\mathrm{ps}$ is due to the back-reflection from the substrate. The respective pump pulse is expected to arrive $2 \times \{100 \times 10^{-6}\,\mathrm{m}/\left[3 \times 10^8\,\mathrm{m/s} \times (1/3.3)\right]\} \sim 2.2\,\mathrm{ps}$ after the actual excitation pulse according to the sample thickness and the refractive index of the substrate of $n = 3.3$ [Iof]. The longer-lived part of the transient is assigned to the electron spin polarisation. This interpretation is confirmed by the corresponding effective Landé factor, that is determined in section 4.1.4. In particular, no signature of hole spin dynamics is resolved in agreement with (i) short hole spin relaxation times in direct-gap semiconductors [Hil02, Yu05, She10] and (ii) the fact that the magneto-optical response associated with transitions from the hh/lh bands to the conduction band is dominated by electron phase space filling (cf. [Lor11]). The red line is a mono-exponential fit to the decay of the electron spin polarisation. The fit reveals a decay time of 10 ps. The triangles in figure 4.2 (b) display the normalized FR observed for the same excitation conditions. The fit – again represented by a red line – corroborates the above spin relaxation time. Both normalized CD and normalized FR are found to deliver comparable spin relaxation times. This applies not only for the specific case discussed here but over the whole investigated parameter range, as is demonstrated along the way in section 4.1.2. The transients in figure 4.2 (b) additionally illustrate the noise suppression resulting from the polarisation bridge (cf. section 3.1). The noise level apparent in the normalized FR transient is 1×10^{-6}, while for the normalized CD transient it is 6×10^{-6}.

[2]The AOM material is TeO_2. Considering only dispersion of second order, the pulses are expected to be broadened to 170 fs. An autocorrelation measurement indicates a pulse duration of 400 fs after transmission through the AOM.

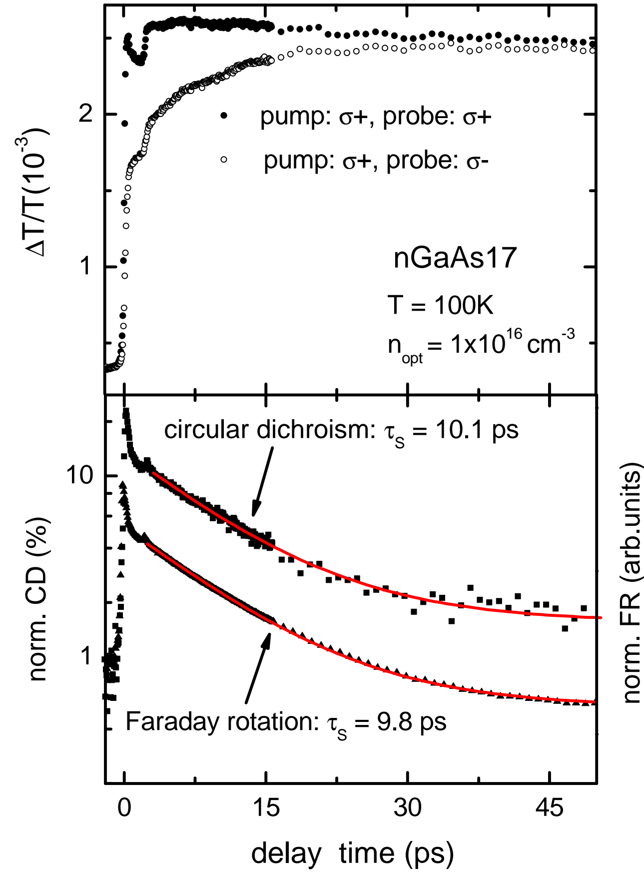

FIGURE 4.2 *(a) Transient differential transmission of sample nGaSb17 at* $T = 100\,\mathrm{K}$. *Solid circles: co-circularly polarised excitation and probe pulses. Open circles: counter-circularly polarised excitation and probe pulses. (b) Squares: normalized CD extracted from the data in panel (a). Triangles: normalized FR for the same experimental conditions. Solid lines: exponential fits to the data.*

4.1.2 Temperature and doping density dependences of the coherence time

Donor concentration $10^{17}\,\mathrm{cm}^{-3}$

Figure 4.3 displays the electron spin relaxation times extracted from normalized CD and/or FR measurements in sample nGaSb17 recorded at various temperatures. The relaxation time decreases from 14 ps at low temperatures to 4 ps at room temperature. For such high mobility n-type samples, electron spin relaxation is expected to be dominated by the DP process [Son02, Jia09b]. The doping density of sample nGaSb17 implies a degenerately occupied conduction band in the low temperature range, as detailed in the discussion of the electronic properties (cf. table 4.2).

In the limit of degenerate electron statistics, the mean electron kinetic energy is approximated by the Fermi energy. The average DP scattering time is then [D'y72]

$$\left(\frac{1}{\tau_s}\right)_{DP,\,deg} = q_{deg}\alpha^2\frac{(E_F)^3}{\hbar^2 E_g}\tau_p \tag{4.4}$$

using the notation of equation (2.21). The solid line in figure 4.3 shows the resulting spin relaxation time with the Fermi energy and the momentum relaxation time at $T = 77\,\mathrm{K}$ extracted from the Hall data (table 4.2), as well as the expected temperature dependences [Bar96]. Note that in combination with α estimated from equation (2.20), $q_{deg} = 3.2$ is needed to obtain agreement with the low temperature spin relaxation times of the experiment. Similar values have been reported for phonon scattering in non-degenerately doped semiconductors, cf. discussion below. In contrast, phonon and ionised impurity scattering in degenerately doped material are characterised by $q_{deg} = 0.3$ and $q_{deg} = 0.05$, respectively [D'y72]. The latter should dominate at low temperatures, corresponding to spin relaxation times ~ 50 times larger than observed in the present experiment. There are several possible explanations for this discrepancy. First and presumably most important, for α approximation (2.20) is used. If corresponding experimental data is available, it is possible to calculate α from the Dresselhaus parameter γ_D [Wu10]

$$\alpha = 2\sqrt{2m_c^3 E_g}/\left(\hbar^3\right) \times \gamma_D. \tag{4.5}$$

Experimental values for γ_D vary over a wide range. For the prototypical semiconductor GaAs experimental – as well as theoretical – γ_D range from $(6-30)\,\mathrm{eV\AA^3}$ [Cha06], and the commonly used $\alpha = 0.07$ [Žut04] corresponds to $\gamma_D \sim 25$. However, the γ_D for GaSb lie between $(100-200)\,\mathrm{eV\AA^3}$ [Cha06], so that equation (2.20) underestimates α by a factor of $3-6$. Taking into account that τ_s is inversely proportional to α^{-2}, equation (4.4) with α calculated from γ_D approximates the experimentally determined low temperature spin relaxation times with q_{deg} closer to the theoretical estimate[3]. In addition, deviations from the degenerate DP model may be attributed to the sample

[3] In [Hau09], the underestimated α according to equation (2.20) have been used. In the following, the values of q_{deg} or q resulting from this choice are indicated together with those from the more reasonable values for α calculated from the literature values for γ_D.

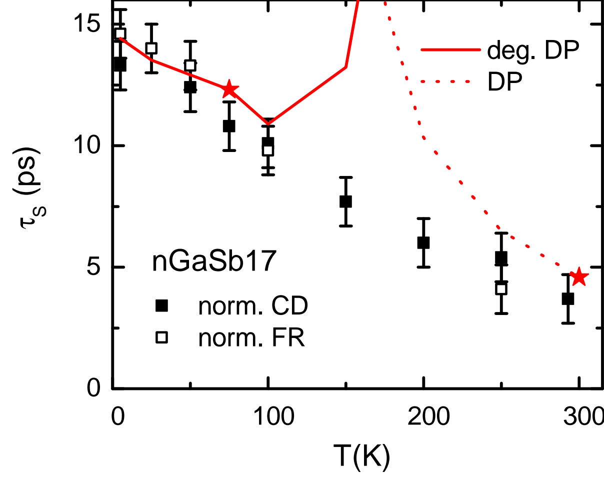

FIGURE 4.3 *Spin relaxation times in nGaSb17 extracted from normalized CD (solid squares) and/or FR (open squares) for various temperatures. Solid and dashed lines: model calculations for the D'yakonov-Perel' mechanisms. The stars indicate points where the Hall mobility is actually measured.*

being a thin layer with dislocations at the film-substrate interface: a dislocation-mediated increase of the spin relaxation rate is suggested by a recent analysis of spin relaxation in InSb [Lit07] and InAs [Lit06] thin films. Furthermore, the measured electron mobility can deviate from the actual bulk transport properties due to carrier accumulation or depletion at surfaces and interfaces [Pet58], and – especially important in pump-probe investigations with optically induced electron densities of the order of or higher than the dopant density – the measured Hall mobility is not necessarily a good indicator for the momentum relaxation time at low temperature. This is, e.g., evidenced by Jiang et al., who use a fully kinetic spin Bloch equation approach to simulate spin relaxation times [Jia09b]. The latter point is, however, more relevant for low temperature spin relaxation in nominally undoped or weakly doped specimens such as sample pGaSb (see below), as well as the $In_{0.53}Ga_{0.47}As$ sample (cf. the more detailed discussion on the basis of comparable literature results for GaAs in section 4.2.2).

For temperatures approaching ambient values, the electron distribution in the conduction band approaches the Boltzmann limit. The mean electron kinetic energy is then the thermal energy and equation (2.21) reads [D'y72]

$$\left(\frac{1}{\tau_s}\right)_{DP} = q\alpha^2 \frac{(k_B T)^3}{\hbar^2 E_g} \tau_p. \tag{4.6}$$

As is true for all model calculations in the further course of the present chapter, the temperature dependence of the bandgap is calculated from equation (2.7) with A and B taken from [Vur01], while for the effective mass the low temperature limit is used over the whole temperature range. (Actually, both temperature dependences are of comparatively minor influence taking into account the limited accuracy especially of the spin-orbit coupling parameter α.) The temperature depen-

dence of the spin relaxation time according to equation (4.6), with α from equation (2.20) and $q = 20$, is plotted as a dashed line in figure 4.3. Again, the value of q needed to reproduce the ultrashort spin relaxation time of 4 ps at room temperature is larger than theoretical predictions of $q \sim 3$ for phonon scattering and $q = 1.5$ for ionised impurity scattering [Mei84, Dzh04]. However, with α calculated from γ_D, the data is approximated with q close to these theoretical suggestions. In addition, the simulation by Song and Kim [Son02] – that relies on theoretical models for the momentum relaxation rates – results in a room temperature electron spin lifetime of several picoseconds in moderately n-doped GaSb, which is in agreement with the present experimental finding. For completeness, it should be noted that the results of Song and Kim for low temperatures indicate spin relaxation times of more than 1 ns. This discrepancy is, however, due to their assumption of non-degenerate carrier statistics, which is inappropriate for a $n \sim 10^{17}\,\mathrm{cm}^3$-doped sample at low temperatures.

Note that in the intermediate temperature range, both applied models – the degenerate and the Boltzmann limit of the DP mechanism – do not reproduce the experimentally observed spin relaxation times. This can be understood since the average kinetic energy of the partially degenerate electron gas is neither appropriately described by $k_B T$ nor by E_F. An appropriate description would instead require an integration over the $E_{\boldsymbol{k}}$ weighted by the effective electron density in the conduction band, which is beyond the scope of the present consideration.

Donor concentration $10^{18}\,\mathrm{cm}^{-3}$

Turning to the more strongly doped sample nGaSb18, spin relaxation times of $(1-2)$ ps are observed over the investigated temperature range from 5 K up to room temperature. The data extracted from normalized CD and/or normalized FR transients are shown in figure 4.4. As calculated in the discussion of the sample's electronic properties, the electron distribution is degenerate up to room temperature (table 4.2). At such low mobilities, and especially in semiconductors of comparatively narrow fundamental energy gap, it has been commonly argued that the EY mechanism markedly contributes to spin relaxation at low temperatures [Son02, Lit06, Lit07]. However, the ab initio simulations of Jiang et al. [Jia09b] introduced in the discussion concerning sample nGaSb17 suggest that the DP process is stronger than the EY mechanism even at such conditions. In the following, the experimentally determined τ_s are compared to the simplified analytical approximations for both mechanisms.

In order to approximate the data with the DP model (4.4), either $q_{deg} = 0.8$ with α according to equation (2.20), or $q_{deg} = (0.02 - 0.1)$ with α calculated from the γ_D given in [Cha06] is needed. As a reminder: the theoretical predictions are $q_{deg} = 0.3$ for phonon scattering and $q_{deg} = 0.05$ for impurity scattering. These values are of the same order of magnitude than those extracted from the present data. The model calculation is included as a red line in figure 4.4. While the model curve agrees with the observed low temperature spin relaxation time, the rather low mobility at room temperature would give rise to a DP spin lifetime of ~ 4 ps.

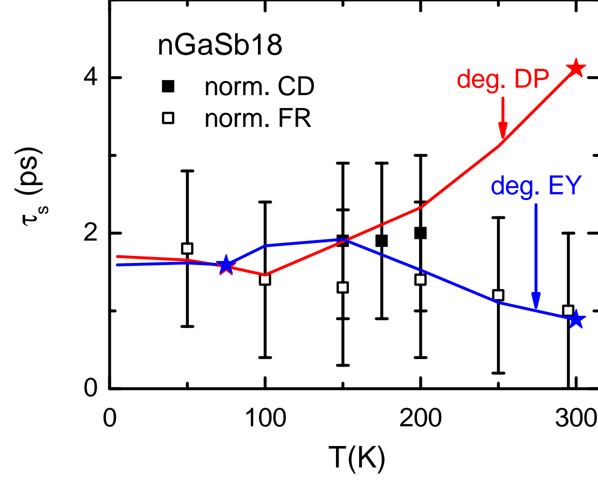

FIGURE 4.4 *Spin relaxation times in nGaSb18 extracted from normalized CD (solid squares) and/or FR (open squares) for various temperatures. Solid lines: model calculations for the D'yakonov-Perel' and Elliott-Yafet mechanisms. The stars indicate points where the Hall mobility is actually measured.*

In the notation of equation (2.17), the EY electron spin relaxation time in case of degeneracy can be estimated by [Mei84]

$$\left(\frac{1}{\tau_s}\right)_{EY,\,deg} = A\beta^2 \left(\frac{E_F}{E_g}\right)^2 \frac{1}{\tau_p} \tag{4.7}$$

where A is typically in the range of $2-6$. The blue line in figure 4.4 shows the result for the EY spin relaxation time computed from equation (4.7) with $E_F = 130\,\text{meV}$ and $A = 6$. As in the model calculations for sample nGaSb17, the momentum relaxation time resulting from the Hall data is used at $T = 77\,\text{K}$ and room temperature, and the temperature dependence of τ_p is modelled according to Baraldi et al. [Bar96]. In contrast to the DP prediction above, the result for the EY mechanism – choosing A in accordance with theoretical predictions – reproduces the low temperature as well as the room temperature lifetime of the experiment.

Nominally undoped GaSb

The above results for the n-doped GaSb layers is compared to the nominally undoped sample pGaSb. The spin relaxation times extracted from normalized CD and/or FR transients for various temperatures are shown in figure 4.5 as filled and open squares. For comparison, the relaxation times that result from mono-exponential fits to the non-normalized transients are shown as filled and open circles. As mentioned in section 4.1.1, in sample pGaSb, the electron population relaxes notably within the spin lifetime at lower temperatures, so that the normalization is necessary. The evaluation reveals spin lifetimes of approximately 30 ps below 50 K. This is twice as long as ob-

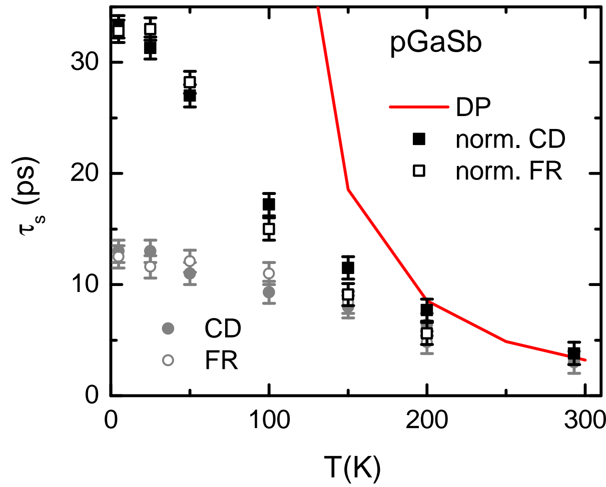

FIGURE 4.5 *Decay times extracted from transient CD and/or FR in nominally undoped GaSb for various temperatures. The filled/open circles result from not normalized transients, whereas the spin relaxation times are determined from normalized CD/FR transients and are represented by the filled/open squares. The solid line is a model calculation according to the D'yakonov-Perel' mechanism.*

served in the moderately n-doped nGaSb17. In particular, the low temperature time constant is approximately four times larger than in undoped GaSb quantum wells, where quantum confinement leads to an enhancement of the DP scattering rate [Hal99]. For higher temperatures, the spin lifetime strongly decreases towards the room temperature value of 4 ps, i.e. comparable to the decay time seen in nGaSb17 (cf. figure 4.3). The solid line in figure 4.5 shows the resulting DP spin relaxation time calculated with equation (4.6). The ultrashort spin lifetime at room temperature is reproduced with either α according to equation (2.20) and $q = 10$ or α calculated from the above mentioned literature values for γ_D and $q = 0.3 - 1$. The latter value is somewhat lower than the expected $q = 3$ for phonon scattering. However, one has to keep in mind that the momentum scattering time is calculated from literature values, instead of actual values, for the electron mobility in the present sample (cf. discussion of the electronic properties in the introductory remarks of the present chapter). The tremendous increase of the spin lifetime at low temperatures predicted by the analytical DP model is not found in the experiment. In this context, first the rather complex structure of impurities acting as acceptors in nominally undoped GaSb [Hu04] should be mentioned. In strongly p-doped GaSb (and GaAs), the BAP mechanism (cf. section 2.3) is reported to limit the electron spin lifetime at low temperatures to the $(1 - 10)$ ns, that are determined from spin-polarised luminescence [Mei84]. For doping concentrations that correspond to the residual hole concentration in the present sample, Song and Kim [Son02] predict spin relaxation times of ~ 250 ps limited by the BAP mechanism. Second, as referred to in the discussion of sample nGaSb17, a failure of the analytical DP model at low temperatures is expected, mainly due to the deviation of the momentum scattering time calculated from the Hall mobility and the actual

one in the optically induced electron distribution. In this context, the above mentioned ab initio simulations of Jiang et al. [Jia09b] even identify the DP mechanism to dominate over the BAP mechanism in p-type GaSb. However, they do not give values that could be compared with the present experimental conditions.

4.1.3 Influence of optically induced carrier density

Since constant irradiances are used over the investigated temperature range, the reduction of the bandgap energy for elevated temperatures effectively yields an increase of n_{opt} by a factor of 2 comparing the room temperature data to the data obtained at $T = 5\,\mathrm{K}$ for samples pGaSb and nGaSb17 (cf. figures 4.3 and 4.5). Figure 4.6 shows the impact of n_{opt} on the spin relaxation time at low temperatures for both samples. The dependences of τ_s on n_{opt} are well described by power law fits with an exponent of -0.1. The trend towards faster spin relaxation upon increasing n_{opt} contradicts DP-dominated spin relaxation at first glance, since stronger electron-electron scattering is expected to decrease the spin relaxation rate in this case [Gla04]. However, more sophisticated simulations addressing DP relaxation of optically induced electron spins are consistent with a decrease of τ_s with increasing n_{opt} [Kra10, Jia09b]. In the present study, such effects are investigated in more detail in $In_{0.53}Ga_{0.47}As$ (cf. section 4.2.2). At this point, the important result is that increasing the excitation power by a factor of 2 has minor influence on the spin relaxation time. At room temperature, the dependence of τ_s on n_{opt} is even less pronounced, as evidenced by a practically constant τ_s in sample pGaSb when varying n_{opt} between $4 \times 10^{15}\,\mathrm{cm}^{-3}$ and $3 \times 10^{16}\,\mathrm{cm}^{-3}$ (data not shown). In the case of sample nGaSb18, n_{opt} is presumably less than the $\sim 1 \times 10^{16}\,\mathrm{cm}^{-3}$ for samples nGaSb17 and pGaSb over the whole investigated temperature range due to the blue-shift in the absorption edge (cf. room temperature transmission, figure 4.1). In conclusion, the dependences discussed in the previous section are confirmed to primarily arise from the variation in crystal temperature.

4.1.4 Spin precession at room temperature

Finally, electron spin dynamics in the presence of in-plane magnetic fields is investigated in sample pGaSb at room temperature. Figure 4.7 depicts FR transients in $B = 0.46\,\mathrm{T}$ and $B = 0.86\,\mathrm{T}$. In addition, a transient without external magnetic field is shown. This transient is modelled by a single exponential decay which – in line with the previous results – reveals a spin relaxation time of $\tau_{B=0} = (3.5 \pm 1)\,\mathrm{ps}$. The transients measured in non-zero magnetic fields are well modelled by exponentially decaying cosine functions mapping the coherent Larmor precession of the optically induced electron spin polarisation (cf. section 2.4). The fits extract spin relaxation times of 3.9 ps at $B = 0.46\,\mathrm{T}$ and 4.5 ps at $B = 0.86\,\mathrm{T}$. Such an increase in τ_s in external magnetic fields is in principle consistent with DP relaxation taking into account magnetic-field induced orbital motion of the conduction band electrons [Žut04]. The cyclotron oscillation of the – with respect to the external magnetic field – transversal components of the electron quasi-momentum effectively leads

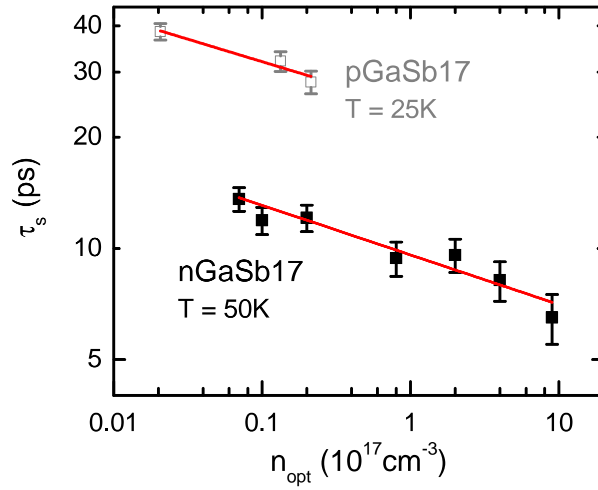

FIGURE 4.6 *Spin relaxation times in samples nGaSb (filled squares) and pGaSb (open squares) for various excitation intensities and low lattice temperatures of* $T = 50\,\mathrm{K}$ *and* $T = 25\,\mathrm{K}$*, respectively. Solid lines: power law fits to the data.*

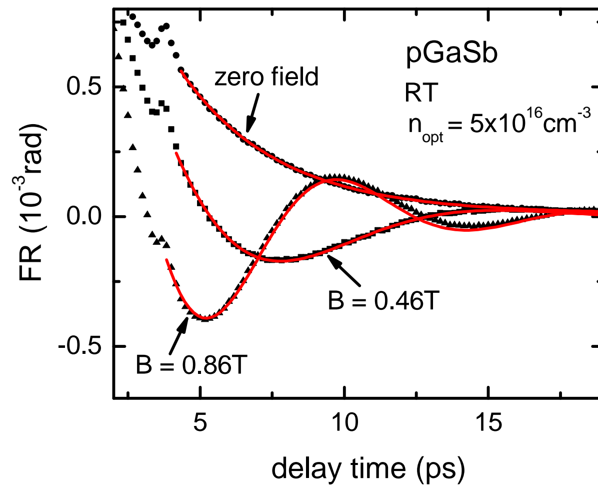

FIGURE 4.7 *FR transients after photo-generation of* $n_{opt} = 5 \times 10^{16}\,\mathrm{cm}^3$ *electrons with a circularly polarised pump pulse in external magnetic fields B of zero,* $0.46\,\mathrm{T}$ *and* $0.86\,\mathrm{T}$*. The solid lines correspond to a single exponential decay (*$B = 0\,\mathrm{T}$*) and exponentially damped cosine functions (*$B = 0.46\,\mathrm{T}$*,* $B = 0.86\,\mathrm{T}$*).*

to a continuous change of the Larmor precession axis between subsequent momentum scattering events. In addition, the data yield an effective Landé factor of $|g^*| = 9 \pm 1$. This result is in agreement $|g^*| = 9.3$ reported from electron spin resonance [Her71], and matches the estimate of $g^* = -9.0$ from 3-band $\boldsymbol{k} \cdot \boldsymbol{p}$-theory (cf. section 2.1). Note that these comparative values are low temperature values. The effective Landé factor is known to depend on temperature. However, for semiconductors that exhibit comparable absolute values of g^*, than observed here, the difference in g^* at liquid helium temperature and room temperature is typically less than the measurement uncertainty of the present investigations (cf. [Oes96] and section 4.2).

4.2 Indium gallium arsenide – $In_{0.53}Ga_{0.47}As$

After some remarks on sample preparation and experimental details, as well as an overview over the sample's electronic properties and room temperature transmission, electron spin dynamics in n-type $In_{0.53}Ga_{0.47}As$ is investigated. Room temperature spin dynamics is discussed in section 4.2.1 as a function of (i) external magnetic field, (ii) temperature ranging from room temperature to $\sim 80^\circ$ C and (iii) optically induced carrier density. The dependence of low temperature electron spin dynamics on (i) optically induced carrier density and (ii) external magnetic field is addressed in section 4.2.2.

Sample and experimental details The $In_{0.53}Ga_{0.47}As$ sample is again provided by Professor Amanns group[1]. The sample is grown by molecular beam epitaxy on a semi-insulating InP substrate. The lattice constants of the two materials are equal so that $In_{0.53}Ga_{0.47}As$ is deposited strain-free on the substrate. The layer is $3.8\,\mu$m thick and n-doped. As described for the GaSb samples, the substrate is thinned to approximately $100\,\mu$m, optically polished, and the sample is glued on an Infrasil window to facilitate time-resolved transmission measurements. Time-resolved magneto-optical measurements are performed at room temperature utilising the Toptica FFS in combination with the EOPC acousto-optic modulator to chop the pump beam at 6 kHz. In this configuration, the sample is placed in the Siemens electromagnet. Additional room temperature data is taken relying on the Coherent RegA/OPA system (if not explicitly labelled "Toptica FFS", the data shown in the following is measured with the OPA as a laser source). In this case the pump beam is chopped with a chopper wheel at a frequency of 1.5 kHz, and the magnetic field is provided by the GMW electromagnet. Low temperature spin dynamics is partly investigated in the latter experimental setup with the sample mounted in the Microstat® He Rectangular Tail cryostat. Alternatively, low temperatures and magnetic fields are provided by the Spectromag® system. The data discussed in the present section is partly from FR and partly from FE transients. The detection method does not affect the results: various control experiments confirm comparable signal amplitudes, decay times and precession frequencies from FR and FE transients. In particular, this finding is in accordance with the equivalence of transient FR and transient CD in GaSb in section 4.1.1.

Electronic properties and room temperature transmission Electronic properties and room temperature transmission of the $In_{0.53}Ga_{0.47}As$ sample are determined analogue to the characterisation of the GaSb samples described at the beginning of section 4.1. Table 4.3 summarises the sample's electronic properties at room temperature and liquid nitrogen temperature. Since the sample is n-conductive, Hall mobility and carrier concentration map the characteristics of conduction band electrons. For comparison: the electron mobility in the $In_{0.53}Ga_{0.47}As$ sample is similar to that reported for nominally undoped GaSb at room temperature, yet a factor of ~ 3 higher than in the latter at liquid nitrogen temperature.

	RT	77 K
n_H ($\mathrm{cm^{-3}}$)	2.4×10^{15}	1.7×10^{15}
μ_H ($\mathrm{cm^2/Vs}$)	9000	38000
τ_p (s)	2×10^{-13}	9×10^{-13}

TABLE 4.3 *Hall mobilities and carrier concentrations at room temperature and liquid nitrogen temperature. The momentum relaxation times are calculated according to equation (4.1) with the electron effective mass specified in table 2.2.*

The room temperature transmission of the $In_{0.53}Ga_{0.47}As$ sample indicates, that the spectral position of the absorption edge corresponds to the room temperature bandgap of 0.74 eV [Vur01], as expected with regard to the low doping concentration (data not shown).

4.2.1 Spin dynamics around room temperature – influences of magnetic field, temperature and optically induced carrier density

Figure 4.8 depicts typical raw data for the $In_{0.53}Ga_{0.47}As$ sample at room temperature. The transients are recorded with the OPA tuned to a central photon energy of 0.8 eV. The optically induced carrier density is $n_{opt} = 3 \times 10^{16}\,\mathrm{cm^{-3}}$. The FR transient in the upper panel is recorded without an external magnetic field, whereas the transients in the middle and lower panel reveal coherent Larmor precession of the optically induced spin polarisation in in-plane magnetic fields of $B = 0.45\,\mathrm{T}$ and $B = 0.73\,\mathrm{T}$. As observed in GaSb, the transients are not indicative of a hole spin signature (this is true not only for the room temperature data discussed in the present section, but also for the low temperature transients that are analysed in section 4.2.2). The solid lines are a single exponential or exponentially decaying cosine functions to extract spin relaxation times and/or the effective Landé factor. The resulting τ_s and $|g^*|$ are summarised in figure 4.9. Note that there is no need to normalize the FR signals to the signal of carrier recombination, since the decay time of the latter is found to be $\geq 5\,\mathrm{ns}$, i.e. at least 2 orders of magnitude longer than the decay time of the electron spin signals.

The lower panel in figure 4.9 depicts the effective Landé factor. The solid line indicates the average value of $|g^*| = 3.8 \pm 0.1$. This value is $\sim 95\,\%$ of the low temperature absolute value estimated from equation (2.9) and actually observed in experiment (cf. section 4.2.2). Sine E_g

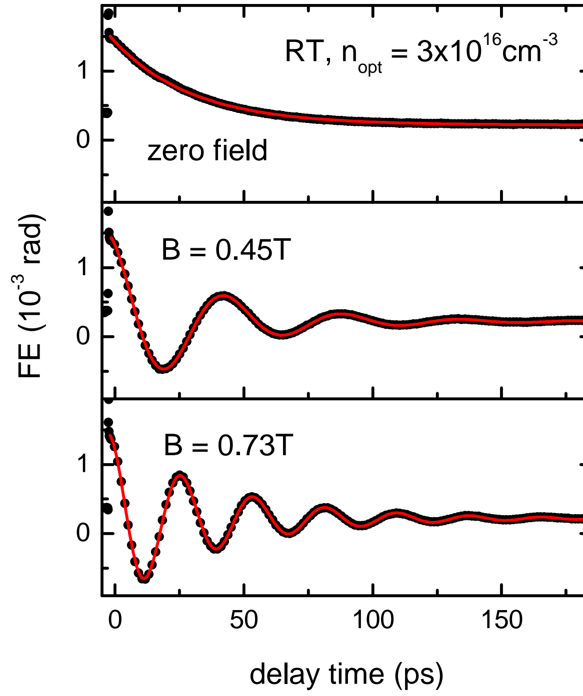

FIGURE 4.8 *FR transients recorded at room temperature after photo-excitation of* $3\times10^{16}\,\mathrm{cm}^{-3}$ *electron-hole pairs in zero magnetic field and in magnetic fields of* $B=0.45\,\mathrm{T}$ *and* $B=0.73\,\mathrm{T}$. *The lines are fits to the data.*

decreases with temperature, the $\boldsymbol{k}\cdot\boldsymbol{p}$-approach predicts a higher absolute value at room temperature which is in contrast to the observation. However, the experimental finding is in line with previous results in GaAs, InSb and CdTe [Oes95, Oes96, Hoh06, Hüb09] and was theoretically reproduced by Zawadzki et al. for GaAs in consideration of the following two aspects [Zaw08]. First, the effective Landé factor does not depend on the overall temperature change of the bandgap. The temperature dependence of g^* – just as that of the effective mass – is rather appropriately described taking into account solely the bandgap modification due to thermal expansion. Second – and this is the more important effect – the effective Landé factor measured at ambient temperatures is not appropriately represented by the band edge value since the electrons occupy energetically higher Landau levels. According to the calculations of Zawadzki et al., in GaAs with $B=4\,\mathrm{T}$ the Landau levels up to $l\sim5$ are of importance at $T=50\,\mathrm{K}$, whereas at $T=300\,\mathrm{K}$ the levels up to $l\sim30$ are occupied. Zawadzki et al. find that the effective Landé factor varies from $g^*\sim-0.5$ in the $l=0$ level to $g^*\sim+1.5$ for the highest level occupied at $T=300\,\mathrm{K}$. Averaging over the Landau levels yields $g^*=-0.44$ ($g^*=-0.3$) at low temperatures ($T=300\,\mathrm{K}$) in agreement with the available experimental data for GaAs. Experiments in InSb and CdTe reveal room temperature values of $|g^*|$ approximately 5 % and 15 % smaller than the respective values at low temperatures. These observations as well the present finding in $In_{0.53}Ga_{0.47}As$ are qualitatively consistent with

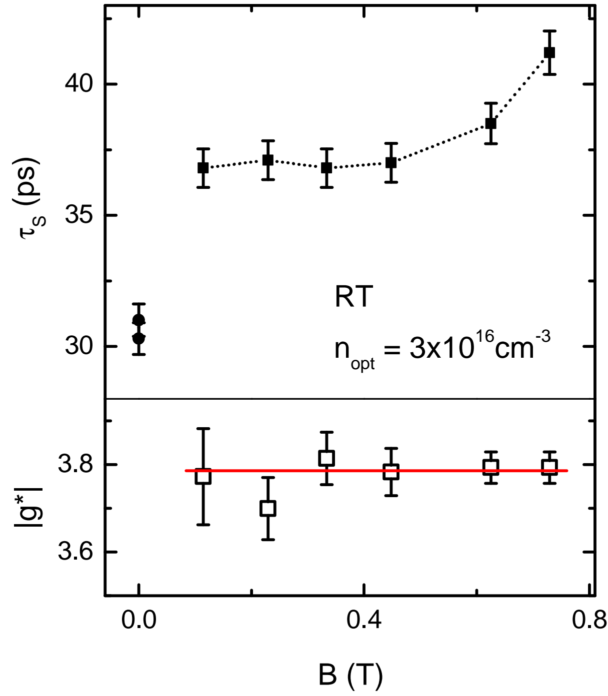

FIGURE 4.9 *Magnetic-field dependent electron spin coherence at room temperature. The upper panel shows the spin relaxation time. The lower panel depicts the effective Landé factor (squares) together with the average value (solid line).*

the theoretical model described by Zawadzki et al.

The upper panel of figure 4.9 shows the spin relaxation time as a function of B. Without external magnetic field, $\tau_s \sim 30\,\text{ps}$, and an enhancement of τ_s is observed for $B \neq 0\,\text{T}$. While the latter is addressed in the following section, it is first of all interesting to compare the observed τ_s to the DP prediction in the Boltzmann limit (4.6). With the low temperature effective mass according to [Vur01], the result is $\tau_s = 25\,\text{ps}$. Assuming the temperature dependence of the effective mass to follow overall temperature dependence of the bandgap results in $\tau_s = 35\,\text{ps}$. Both values – calculated with $q = 3$ for momentum scattering dominated by polar-optical phonons [Dzh04], and α estimated according to equation (2.20)[4] – are in good agreement with the present experimental finding. In addition, due to the high mobility, EY relaxation (2.17) with $A = 2$ for phonon scattering [Mei84] is a factor of $20-30$ weaker and therefore of minor influence. Although the arguments so far indicate that the DP mechanism is responsible for spin relaxation in $In_{0.53}Ga_{0.47}As$ at room temperature, additional information is desirable to substantiate the statement, just because for α a theoretical approximation is used and – as mentioned in section 2.3 – literature values, e.g.

[4]The remaining parameters are (i) the momentum relaxation time calculated from the room temperature Hall mobility (cf. table 4.3), (ii) the fundamental bandgap energy at room temperature interpolated from the respective values for InAs and GaAs, and (iii) the split-off energy from table 2.2.

for GaAs, vary by a factor of 5.

Magnetic field dependence

The magnetic field dependence of τ_s, depicted in the upper panel of figure 4.9, provides an additional argument supporting DP relaxation. The observed suppression of spin relaxation with increasing magnetic field is in principle in line with this mechanism, as motivated in section 4.1.4. For a more detailed analysis, the τ_s found in Voigt configuration are compared to those in Faraday configuration. In the latter configuration, the external magnetic field is oriented parallel to the direction of light propagation and thus parallel to the optically induced spin polarisation. Consequently, the transients recorded in Faraday geometry trace the exponential decay of the spin polarisation along the magnetic direction, and no Larmor precession is detected. Such an investigation is conducted with the Toptica FFS as a laser source. The spin relaxation times extracted from transients recorded in Voigt- as well as in Faraday geometry are displayed in figure 4.10 as a function of the external magnetic field. (Note that, compared to the data in Voigt geometry relying on the OPA in figure 4.9, the τ_s in Voigt geometry measured with the fibre laser are $\sim 10\,\%$ higher for $B \neq 0$. Since comparable densities of optically induced carriers – $n_{opt} \sim 10^{16}\,\mathrm{cm}^{-3}$ with both laser sources – are used, this finding possibly implies an influence of the actual energy distribution of the optically induced carriers: although the OPA is tuned to the central photon energy of the Toptica FFS ($\hbar\omega = 0.8\,\mathrm{eV}$), the FWHM of the fibre laser pulses is approximately a factor of 1.5 smaller than that of the OPA pulses, cf. section 3.1.) The suppression of DP relaxation in an external magnetic field due to the cyclotron motion of the electrons is theoretically treated in [Ivc73, Mar83], and for small magnitudes of the external magnetic field is described by [Lit10]

$$\tau_s(0) = \frac{1}{8}\left[\frac{5}{1+(\omega_c\tau_p^*)^2} + \frac{3}{1+(3\omega_c\tau_p^*)^2}\right]\tau_s(B). \tag{4.8}$$

The range of small magnetic-field magnitudes is limited by the conditions $\omega_L\tau_p \ll 1$ and $\omega_L/\omega_c \ll 1$ [Ivc73], where $\omega_c = (e/m_c)B$ is the cyclotron frequency. Both conditions are fulfilled in the magnetic-field range of the present investigation: at $B = 1\,\mathrm{T}$, $\omega_L\tau_p = (3.3\times 10^{11}\,\mathrm{s}^{-1})\times(2\times 10^{-13}\,\mathrm{s}) \sim 0.1$ and $\omega_L/\omega_c = 3.3\times 10^{11}\,\mathrm{s}^{-1}/(4.3\times 10^{12}\,\mathrm{s}^{-1}) \sim 0.1$. The spin relaxation time at zero magnetic field is denoted $\tau_s(0)$, while $\tau_s(B)$ is the relaxation time in the presence of an external magnetic field. τ_p^* is proportional to the momentum relaxation time, e.g. in [Lit10] $\tau_p^* = \tau_p/3$ is used, which is, however, explicitly stated to apply for impurity scattering. The model equation (4.8) fits the τ_s measured in Faraday geometry with $\tau_p^* = 0.8\times 10^{-13}\,\mathrm{s} \sim \tau_p/3$. The respective fit is included in figure 4.10. The data in Voigt geometry can not be reproduced with the model, although it should hold for both Faraday and Voigt geometry according to [Lit10]. Indeed in Voigt geometry, additional impact of an external magnetic field on spin relaxation is known [Bro04, and references therein]. In contrast to the increase of τ_s with increasing magnetic field due to the randomisation effect of cyclotron motion on the quasi-momentum distribution, the presence

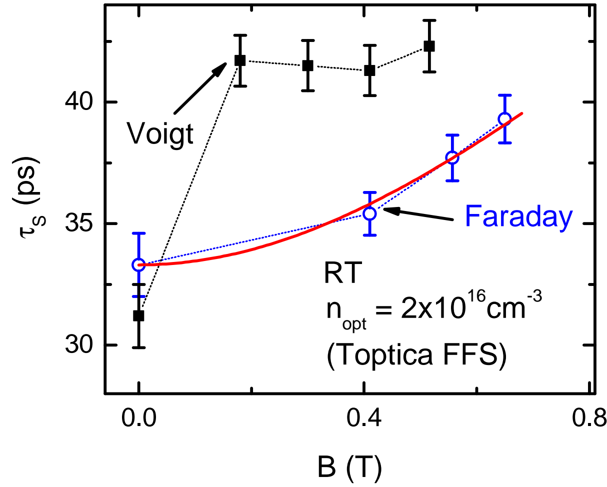

FIGURE 4.10 *Magnetic-field dependent spin relaxation times at room temperature. Black solid squares:* ***B*** *– as usually – oriented in the sample plane (Voigt geometry). Blue open circles:* ***B*** *parallel to the propagation direction of light (Faraday geometry). The color-coded dotted lines are guides to the eye. The red solid line is a fit according to equation (4.8) to the τ_s measured in Faraday geometry.*

of an external magnetic field can also enhance spin relaxation. The reason is the non-parabolic correction of the conduction band dispersion, or explicitly a term $\propto \boldsymbol{k}^4$. This is not negligible off the conduction band edge, so that the spin splitting of the conduction band – and consequently the electron g^* factor – is inhomogeneous, which in turn leads to faster spin relaxation. As a result, a peak in τ_s is expected for a certain magnetic-field magnitude depending on band parameters, carrier density and temperature. For instance, in GaAs with $n_d = 1 \times 10^{17}\,\mathrm{cm}^{-3}$ and at $T = 100\,\mathrm{K}$, the peak position is predicted at $B \sim 10\,\mathrm{T}$ [Bro02], and experimentally observed at $B = 1\,\mathrm{T}$ in comparably doped InAs in the same temperature range [Lit10]. Consequently, this effect can not explain the different characteristics of τ versus B in Voigt- and Faraday geometry observed in the present study, that particularly appear at low magnetic fields. Nevertheless, the finding that the external magnetic field tends to increase the spin relaxation time – and thus DP relaxation dominates spin relaxation – holds in Voigt as well as in Faraday geometry.

Temperature dependence

The dominance of the DP mechanism is further corroborated by the temperature dependence of the spin relaxation time shown in the upper panel of figure 4.11. The corresponding measurements are again conducted with the Toptica FFS as a laser source, and the sample temperature is varied from room temperature to $\sim 80^\circ\,\mathrm{C}$ by ohmic heating[5]. The error bars in the temperature indicate

[5] The original goal of the measurements was to investigate the influence of an electric field on g^*. Such an effect is expected to be linear in the electric field and was observed in electron spin resonance measurements in a two-dimensional electron gas in an asymmetric silicon quantum well [Wil07]. Instead of a linear dependence, the present

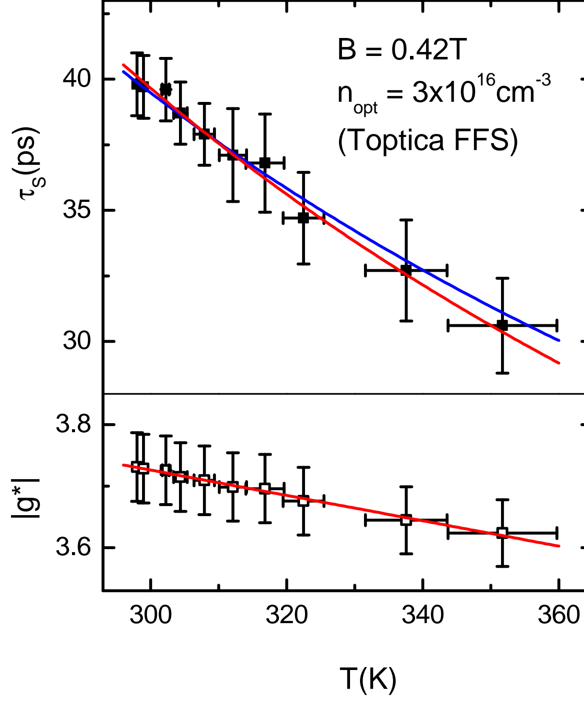

FIGURE 4.11 *Electron spin relaxation time and effective Landé factor for various temperatures from room temperature up to* $\sim 80^{\circ}$ C*. The associated FR transients are recorded in* $B = 0.42$ T*. The data in the upper panel is fitted with equation (4.9) for phonon-mediated DP relaxation (solid lines, for details refer to the main text). The solid line in the lower panel is a linear fit to the data.*

various assumptions for the temperature dependence of the effective mass. The data points are determined assuming that the effective mass decreases linear with temperature, but with half the gradient of the bandgap temperature characteristics. This accounts for the fact that the effective mass is a function of the dilatation change of the bandgap rather than of its overall temperature dependence (and is the most likely assumption, cf. section 2.1). The temperature error bars include constant effective mass (lower boundary), and the assumption that the effective mass follows the overall temperature dependence of the bandgap (upper boundary). The solid lines are fits to the temperature dependence of τ_s, assuming DP relaxation and polar-optical phonon scattering as the dominant momentum relaxation mechanism. Combining the temperature dependence of the latter described by $\tau_p = C(m_c/e)T^{-3/2}$ with equation (4.6) for DP relaxation in the Boltzmann limit yields

$$\tau_s = \left(\hbar^2 E_g\right) / \left[q\alpha^2 (k_B T)^3 C(m_c/e) T^{-3/2}\right]. \tag{4.9}$$

investigation revealed a decrease of both τ_s and g^* quadratic in the electric field, which leads to the conclusion that a temperature effect is observed rather than a direct influence of the electric field. The voltage-to-temperature conversion is determined from the voltage- or temperature-dependence of the transmission (for details, refer to appendix A).

To reproduce the electron mobility determined at room temperature (cf. table 4.3), the constant prefactor is chosen $C = 4.6 \times 10^7\,\mathrm{cm^2K^{3/2}(Vs)^{-1}}$. α is taken according to equation (2.20), and q as a free fitting parameter. The blue fit neglects the temperature dependences of E_g, α and the effective masses and yields $q = 2.7$. Taking into account the temperature dependences – using the weakened characteristics for the effective masses – results in $q = 2.2$. Both values are close to $q = 3$ for scattering with polar-optical phonons. Indeed, the temperature dependences of the band parameters are only of minor influence, so that the model (4.9) actually predicts $\tau_s \propto T^{-3/2}$, which is in line with the measured $\tau_s(T)$ within the limits of accuracy. Overall, the results are in good agreement with a similar investigation of room temperature spin relaxation in GaAs [Oer08].

Not only τ_s, but also the effective g factor decreases with increasing temperature. The data is shown in the lower panel of figure 4.11 together with a linear fit, that explicitly is

$$g^*(T) = -4.3 + 2 \times 10^{-3}\,\mathrm{K^{-1}}T.$$

This phenomenological model predicts $g^* \sim -4.3$ at absolute zero, compared to $|g^*| = 4.2$ as calculated from equation (2.9) and as experimentally observed close to liquid helium temperature (cf. section 4.2.2). Again, the present finding is in accordance with literature results in other materials: in the ambient temperature range, a linear dependence of g^* on temperature is reported in both CdTe and GaAs [Oes96, Zaw08]. Östreich et al. found that their experimentally determined g^* are reasonably approximated by $g^*(T) = -0.44 + 5 \times 10^{-4}T$ from room temperature down to liquid helium temperature [Oes96]. Such a trend is confirmed by the sophisticated theoretical model of Zawadzki et al., that additionally reproduces the flattening of $g^*(T)$ below $T \sim 20\,\mathrm{K}$ [Zaw08] (that occurs in agreement the minor temperature dependence of the bandgap in this temperature range).

Influence of the optically induced carrier density

In order to further examine the nature of spin relaxation at room temperature, the dependence of $|g^*|$ and τ_s on the optically induced carrier density is analysed. Figure 4.12 shows τ_s and $|g^*|$ for n_{opt} ranging from $3 \times 10^{16}\,\mathrm{cm^{-3}}$ to $5 \times 10^{18}\,\mathrm{cm^{-3}}$. The corresponding FR transients are recorded in an external magnetic field of $B = 0.73\,\mathrm{T}$ with the OPA tuned to a central photon energy of 0.8 eV. The spin relaxation time is independent of n_{opt} for carrier densities smaller than $\sim 3 \times 10^{17}\,\mathrm{cm^{-3}}$. At such densities the effective Landé is reduced from $|g^*| = 3.8$ at $n_{opt} = 3 \times 10^{16}\,\mathrm{cm^{-3}}$ – this value is represented as a guide to the eye by the dashed line in the lower panel of figure 4.12 – to $|g^*| = 3.6$ at $n_{opt} = 4 \times 10^{17}\,\mathrm{cm^{-3}}$. In contrast, τ_s markedly decreases upon further increase of n_{opt}. It reduces from $\sim 40\,\mathrm{ps}$ in the range up to $\sim 4 \times 10^{17}\,\mathrm{cm^{-3}}$ to $\sim 20\,\mathrm{ps}$ at the highest investigated density, following the power law dependence $\tau_s \propto n_{opt}^{-0.25}$. The effective Landé factor decreases from $|g^*| = 3.6$ at $n_{opt} = 4 \times 10^{17}\,\mathrm{cm^{-3}}$ to $|g^*| = 2.8$ at $n_{opt} = 5 \times 10^{18}\,\mathrm{cm^{-3}}$. The decrease can also be modelled by a power law, $|g^*|$ is proportional to $n_{opt}^{-0.1}$. To interpret these observations, first of all, faster carrier recombination that could potentially pretend reduced spin relaxation times at high n_{opt} can be excluded. Even for the highest n_{opt}, the carrier recombination time is found

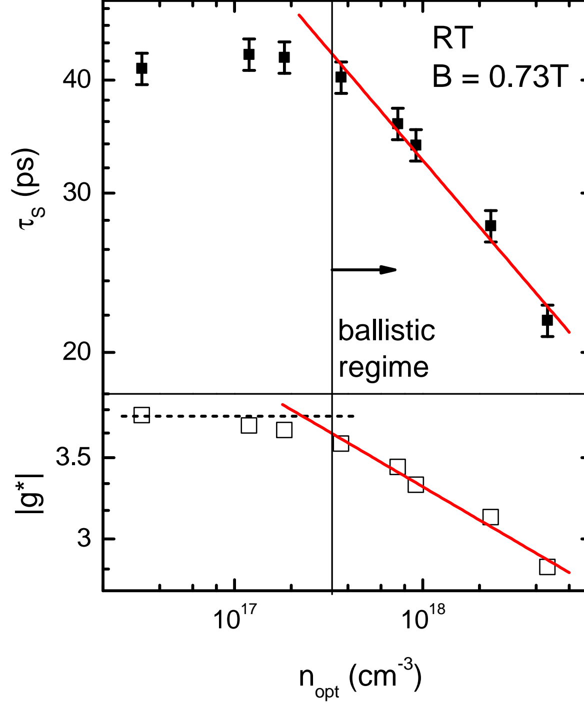

FIGURE 4.12 *Influence of the optically induced carrier density on spin relaxation time (upper panel) and effective Landé factor (lower panel). The corresponding FR transients are recorded at room temperature in $B = 0.73\,\mathrm{T}$. The uncertainty in $|g^*|$ is indicated by the size of the data points. The dashed line indicates $|g^*| = 3.8$ as extracted from the analysis of FR transients in various magnetic-field magnitudes at $n_{opt} = 3\times10^{16}\,\mathrm{cm}^{-3}$. The solid lines are power law fits to the data for $n_{opt} > 3\times10^{17}\,\mathrm{cm}^{-3}$.*

to exceed 5 ns and thus is of negligible influence. Another argument is in fact more informative. If DP relaxation dominates spin relaxation, an increase of n_{opt} can affect spin relaxation in two ways. In the motional narrowing regime (cf. section 2.3), an impact is only expected in case electron-electron scattering markedly contributes to momentum relaxation. If so, τ_s increases linearly with n_{opt} [Gla04, Oer08], since the spin relaxation time is inversely proportional to the momentum relaxation time. In [Oer08], a saturation of $\tau_s = 75\,\mathrm{ps}$ in n-type GaAs – the donor concentration is comparable to that of the $In_{0.53}Ga_{0.47}As$ sample investigated here – is observed in the range $n_{opt} \leq 1\times10^{17}\,\mathrm{cm}^{-3} - 2\times10^{17}\,\mathrm{cm}^{-3}$. The authors partially attribute this observation to enhanced screening of the electron-electron interaction and phase space filling. Both effects attenuate the enhancement of the scattering probability with increasing carrier density. Regarding the present investigation, the lower densities apparently lie within such a regime. A comparable decrease of τ_s upon a further increase of n_{opt}, as observed here, was also seen in GaAs [Ten09]. To explain such a decrease, it is instructive to recheck the motional narrowing condition $\Omega_{BIA} \leq \tau_p$ [Jia09a, She09, Kra10]. To do so, n_{opt} has to be compared to the effective density of states

in the conduction band, which – according to equation (4.3) – is $N_c = 2 \times 10^{17}\,\text{cm}^{-3}$ at room temperature. Consequently, for $n_{opt} > 2 \times 10^{17}\,\text{cm}^{-3}$ the conduction band is filled up to the Fermi energy calculated from equation (4.2) with the actual electron concentration in the conduction band $N = n_{opt} + n_d$. The maximum Ω_{BIA} can be calculated according to equation (2.19), the results are summarised in table 4.4 for various values of n_{opt} and $\boldsymbol{k}$ along $[1,1,0]$. This estimation shows

n_{opt} (cm^{-3})	2×10^{17}	1×10^{18}	5×10^{18}
E_F (meV)	8	80	260
Ω_{BIA} (s^{-1})	7.4×10^{10}	2.3×10^{12}	1.4×10^{13}
$\Omega_{BIA} \times \tau_p$	0.01	0.5	3

TABLE 4.4 *Transition from the motional narrowing to the ballistic regime of DP relaxation. The Fermi energy and $\Omega_{BIA}(E_F)$ are calculated according to equations (4.2) and (2.19), respectively. The momentum relaxation time is $\tau_p = 2 \times 10^{-13}\,\text{s}$.*

that the transition from the motional narrowing to the ballistic regime of DP relaxation occurs in close proximity to the beginning decrease of τ_s with $n_{opt}^{-0.25}$. Moreover, it is not surprising with regard to the tremendous influence of filling up higher Landau levels (cf. discussion above), that the decrease in $|g^*|$ proportional to $n_{opt}^{-0.1}$ starts at the transition from non-degenerate to degenerate distribution of the optically induced electrons.

4.2.2 Spin dynamics at low temperature – dependences on optically induced carrier density and magnetic field

Figure 4.13 depicts typical FR transients in $In_{0.53}Ga_{0.47}As$ at $T = 5\,\text{K}$. Unless stated otherwise, the transients discussed in the following are extracted from raw data recorded after left- and right-circularly polarised excitation according to $[FR_{\sigma^+}(t) - FR_{\sigma^-}(t)]/2$. This procedure subtracts a slowly varying, polarisation-independent background from the data. The transients in figure 4.13 are recorded in an external magnetic field of $B = 0.73\,\text{T}$ after excitation with pulses centred at $0.80\,\text{eV}$. The pulses central photon energy is lower than the bandgap energy of $E_g = 0.816\,\text{eV}$ (cf. table 2.2), while photons with $(0.80 + 0.02)\,\text{eV}$ – as mentioned in section 3.1, the full-width-half-maximum of the OPA pulses is $40\,\text{meV}$ – excite electrons with an excess energy of less than $10\,\text{meV}$. The transients are well modelled by exponentially decaying cosine functions, fits are included in figure 4.13 as solid lines.

Influence of the optically induced carrier density

As at room temperature (see previous section 4.2.1), the optically induced carrier density influences the decay time of the electron spin signal as well as the effective Landé factor. Focussing first on τ_s, the transient in the upper panel of figure 4.13 is, e.g., recorded with $n_{opt} = 8 \times 10^{14}\,\text{cm}^{-3}$

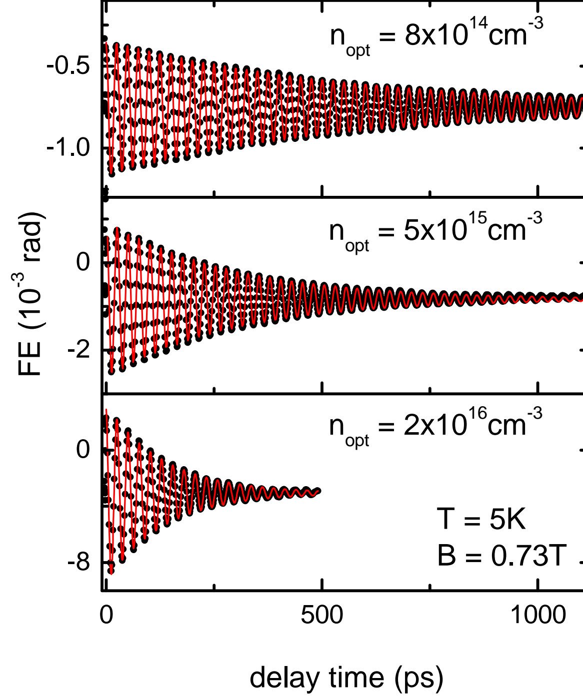

FIGURE 4.13 *FR transients at* $T = 5\,\mathrm{K}$ *in* $B = 0.73\,\mathrm{T}$. *The density of optically induced electron-hole pairs varies from* $n_{opt} \leq n_d$ *(upper panel) to* $n_{opt} \sim 10 \times n_d$ *(lower panel), where* $n_d = 1.7 \times 10^{15}\,\mathrm{cm}^{-3}$ *is the doping-induced electron density in the conduction band at* $T = 77\,\mathrm{K}$. *The lines are fits to the data.*

and decays within $\sim 500\,\mathrm{ps}$, whereas the fit to the transient in the lower panel – for which n_{opt} is a factor of 25 higher – reveals $\tau_s \sim 100\,\mathrm{ps}$. Figure 4.14 displays the τ_s and $|g^*|$ for a wide range of optically induced carrier densities from $2 \times 10^{14}\,\mathrm{cm}^{-3}$ to $\sim 10^{18}\,\mathrm{cm}^{-3}$. The size of data points correspond to the error bars for both quantities. As indicated by the different colours, the central photon energy of excitation and probe pulses varies from 0.83 eV over 0.80 eV to 0.79 eV (the full-width-half-maximum is $\sim 40\,\mathrm{meV}$ in all three cases). The reason for lowering the central photon energy is to achieve lower n_{opt}.

The effective Landé factor is in a good approximation independent of n_{opt} as long as it is $\lesssim 10^{16}\,\mathrm{cm}^{-3}$. The solid line in the lower panel of figure 4.14 indicates the average value of $|g^*| = 4.22 \pm 0.06$ at low excitation densities. Such a value is close to results of $g^* = -4.04 \pm 0.02$ [Bee95] or $g^* = -4.070 \pm 0.005$ [Kow96] from electron spin resonance measurements. It is furthermore well approximated by the three-band $\boldsymbol{k}\cdot\boldsymbol{p}$-prediction of $g^* = -4.2$ as calculated from equation (2.9). For $n_{opt} > 10^{16}\,\mathrm{cm}^{-3}$, the effective Landé factor decreases, which once again is possibly attributed to the filling of higher Landau levels.

Turning the focus to the spin relaxation time, a comparatively slow decline is observed for $n_{opt} \lesssim 10^{15}\,\mathrm{cm}^{-3}$ from $\tau_s \sim 600\,\mathrm{ps}$ at $n_{opt} = 2 \times 10^{14}\,\mathrm{cm}^{-3}$ to $\tau_s \sim 500\,\mathrm{ps}$ at $n_{opt} = 1 \times 10^{15}\,\mathrm{cm}^{-3}$.

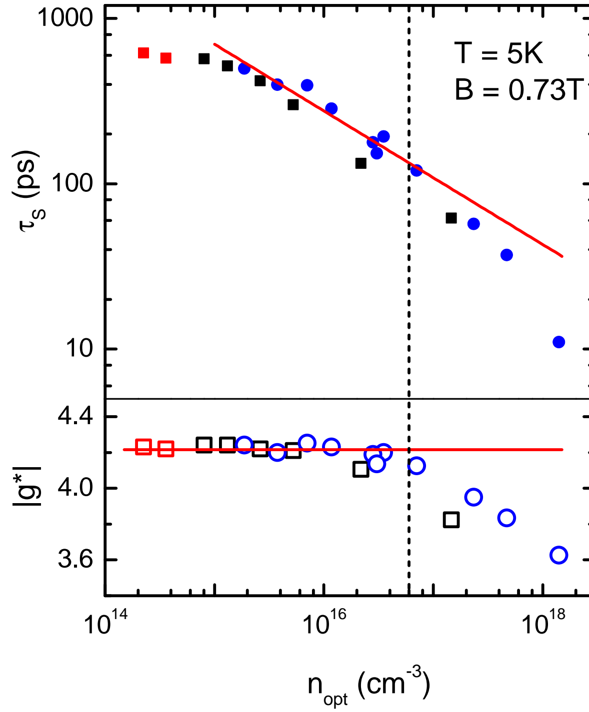

FIGURE 4.14 *Influence of the optically induced carrier density on spin relaxation time (upper panel, logarithmic abscissa and ordinate) and effective Landé factor (lower panel, logarithmic abscissa) at low temperatures. The corresponding FR transients are recorded in $B = 0.73\,\mathrm{T}$. The central photon energy is $0.83\,\mathrm{eV}$ (blue), $0.80\,\mathrm{eV}$ (black) and $0.79\,\mathrm{eV}$ (red). The error bars for τ_s and $|g^*|$ are indicated by the size of the data points. The solid line in the upper panel is a power law fit to the $0.83\,\mathrm{eV}$ data. The solid line in the lower panel indicates the average value of $|g^*|$. Both fits include only the data points with $n_{opt} < 6\times10^{16}\,\mathrm{cm}^{-3}$ (vertical dashed line).*

A further increase in n_{opt} decreases the relaxation time according to approximately $n_{opt}^{-0.4}$ as long as n_{opt} is smaller than $\sim 10^{17}\,\mathrm{cm}^{-3}$. A corresponding fit to the data with the photon energy centred at $0.83\,\mathrm{eV}$ is included exemplarily in the upper panel of figure 4.14. At higher excitation densities, τ_s decreases even faster with n_{opt}. For comparison: at room temperature $\tau_s \propto n_{opt}^{-0.25}$ is observed in this density range (cf. section 4.2.1). First of all, the τ_s found in experiment are orders of magnitude lower than the theoretical prediction for degenerate DP (4.4) or EY (4.7) relaxation with the momentum relaxation time calculated from the measured Hall mobility and its typical temperature dependence [Oli81]. In the temperature range of interest – that is $(5-10)$ K – the strongest spin relaxation rate is predicted by the degenerate EY model. The corresponding τ_s is $\sim 100\,\mathrm{ns}$ as compared to the experimentally observed $\sim 500\,\mathrm{ps}$ at low excitation densities. As mentioned in the discussion of the low temperature spin relaxation times in GaSb in section 4.1.2, a more sophisticated theoretical model is crucial to explain the experimentally determined τ_s. The main reason is the tremendous energy dependence of the momentum scattering rate at low temperatures, that

is not appropriately accounted for by the τ_p extracted from the Hall mobility and by simplifying the carrier energy distribution with the constant values kT or E_F [Jia09b]. As already mentioned, the fully microscopic kinetic spin Bloch equation approach of Jiang et al. overcome such inadequate assumptions [Jia09b]. In their approach, all possible momentum scattering mechanisms are included ab initio. The authors identify the DP mechanism to dominate over the EY mechanism over a wide range of electron densities and even for narrow gap semiconductors like InAs or InSb. This is in contrast to the conclusions drawn from the simplified analysis relying on equations (4.4) and (4.7). For the prototypical material GaAs at liquid helium temperature, Krauß et al. compare model calculations similar to those of Jiang et al. to the spin relaxation times they extract from FR transients [Kra10]. For moderately n-doped GaAs with $n_d \sim 4\times10^{16}\,\mathrm{cm}^{-3}$, their results range from $\tau_s = 900\,\mathrm{ps}$ (theory) and $\tau_s = 600\,\mathrm{ps}$ (experiment) for $n_{opt} \sim 10^{15}\,\mathrm{cm}^{-3}$ to $\tau_s = 350\,\mathrm{ps}$ (theory) and $\tau_s = 500\,\mathrm{ps}$ (experiment) for $n_{opt} \sim 4\times10^{16}\,\mathrm{cm}^{-3}$. Given that the spin-orbit parameter α is comparable for GaAs and $In_{0.53}Ga_{0.47}As$, similar values for τ_s in both materials are reasonable. Moreover, the theoretical dependence of τ_s on n_{opt} found by Krauß et al. can be approximated by a a power law fit with an exponent of $-(0.4-0.5)$ for n_{opt} in the range of $(1-4)\times10^{16}\,\mathrm{cm}^{-3}$ and is less steep for lower excitation densities. These findings are similar to the present observations for $In_{0.53}Ga_{0.47}As$. In total, the low temperature dependence of τ_s on n_{opt} found in the present study are qualitatively and quantitatively in line with DP relaxation of conduction band electron spins. Another interesting point is the range of the motional narrowing regime at low temperatures. According to equation (4.3), the critical density at $(5-10)\,\mathrm{K}$ is a factor of ~ 100 lower as compared to the value at room temperature, or precisely $N_c = 5\times10^{14}\,\mathrm{cm}^{-3}$ at 5 K. The Fermi energy (4.2) thus overcomes the thermal energy even for the lowest investigated $n_{opt} < 10^{15}\,\mathrm{cm}^{-3}$. At such low excitation densities and with taking into account $n_d = 1.7\ \times10^{15}\,\mathrm{cm}^{-3}$, $E_F \sim 1\,\mathrm{meV}$, whereas at the highest investigated $n_{opt} \sim 10^{18}\,\mathrm{cm}^{-3}$, $E_F = 90\,\mathrm{meV}$. With $\tau_p \sim 10^{-14}\,\mathrm{s}$ at $T = 5\,\mathrm{K}$, this results in $\Omega_{BIA}\times\tau_p = 0.06 \ll 1$ even for $n_{opt} \sim 10^{18}\,\mathrm{cm}^{-3}$. Thus, for an electron that is fully described by E_F and τ_p calculated from the Hall mobility, the motional narrowing condition would hold over the hole investigated range of excitation densities. However, as mentioned above, the optically induced electron distribution is not necessarily appropriately described using these approximations. For example, Krauß et al. estimate the transition from the motional narrowing to the ballistic regime at an electron density of $\sim 10^{17}\,\mathrm{cm}^{-3}$ for their moderately doped n-GaAs sample and $n_{opt} = 2\times10^{16}\,\mathrm{cm}^{-3}$. This corresponds to the density above which the $n_{opt}^{-0.4}$ does not model the dependence of τ_s on n_{opt} – and the density above which $|g^*|$ markedly deviates from the low density value – in the $In_{0.53}Ga_{0.47}As$ data shown in figure 4.14.

Magnetic field dependence of the coherence time

As mentioned at the beginning of the present chapter, comparatively long spin coherence times are observed when the spin-carrying electrons are bound to donors. However, the value of the spin relaxation time discussed in the previous section point to DP relaxation of itinerant elec-

trons. To gain further information about the dominant relaxation mechanisms, the magnetic field dependence of τ_s is investigated. Background of this approach is the marked decrease in τ_s with increasing magnetic field observed by Kikkawa et al. [Kik98] in the case of donor-bound electrons, where spin relaxation is dominated by hyperfine interaction with the lattice nuclei and/or anisotropic exchange interaction (cf. section 2.3). Consequently, despite the exact values of τ_s, a reversed dependence of τ_s on B as compared to the observation at room temperature discussed in section 4.2.1 can point to spin relaxation of donor-bound electrons. Figure 4.15 shows the τ_s as well as the effective Landé factor extracted from FR transients recorded at $T = (8-10)\,\mathrm{K}$. The magnetic field dependence is shown for two different excitation densities, $n_{opt} = 3\times10^{16}\,\mathrm{cm}^{-3}$ (black data points) and $n_{opt} = 6\times10^{14}\,\mathrm{cm}^{-3}$ (blue data points) from zero magnetic field up to $0.7\,\mathrm{T}$. The latter excitation density is in the range of the minimal n_{opt} examined in the present study (cf. discussion in the previous section 4.2.2).

The effective Landé factor is independent of B as expected at such comparatively low magnetic fields [Oes95]. The solid line is a fit to the data and reveals $|g^*| = 4.18\pm0.06$ in agreement with the finding in section 4.2.2.

Turning the focus to the spin relaxation time, the dependence on n_{opt} is comparable for both excitation densities and similar to the situation at room temperature: the relaxation times in an external magnetic field are found to exceed those for zero magnetic field, and increasing B tends to extend spin coherence. Consequently, even at $n_{opt} = 6\times10^{14}\,\mathrm{cm}^{-3}$ the magnetic field dependence points towards DP relaxation of conduction band electron spins rather than relaxation of donor-bound electron spins. The reason is probably the spectral width of the utilised laser pulses centred at $\hbar\omega$. As previously mentioned, the photons with energy $(\hbar\omega + \mathrm{HWHM})$ excite electrons with an excess energy of some meV. Those, as well as electrons excited by photons of even higher energy, contribute markedly to the electron population keeping in mind that the pulses are centred below the bandgap in the temperature range of interest. Typical binding energy at shallow donors lie in the same order of magnitude than such excess energies [Nak99], so that it is not astonishing, that itinerant electrons dominate the signal in the present excitation configuration.

Nevertheless, FR transients at $B = 1.4\,\mathrm{T}$ and $B = 2.1\,\mathrm{T}$ give rise to the interpretation that a mixture of itinerant and donor-bound electrons is responsible for the FR signal. Both transients are recorded under the same conditions than the transients that correspond to the data at the lower n_{opt} in figure 4.15. The transient at $B = 1.4\,\mathrm{T}$ is shown exemplarily in figure 4.16 (as a black line in the main panel). Unlike the transients recorded in magnetic fields up to $0.7\,\mathrm{T}$, the Larmor precessions at higher fields can not be modelled adequately by a single exponentially damped cosine function. The transients are rather well reproduced by two exponentially decaying cosines of same frequency but different initial amplitudes A_i, relaxation times τ_{si} and a phase difference

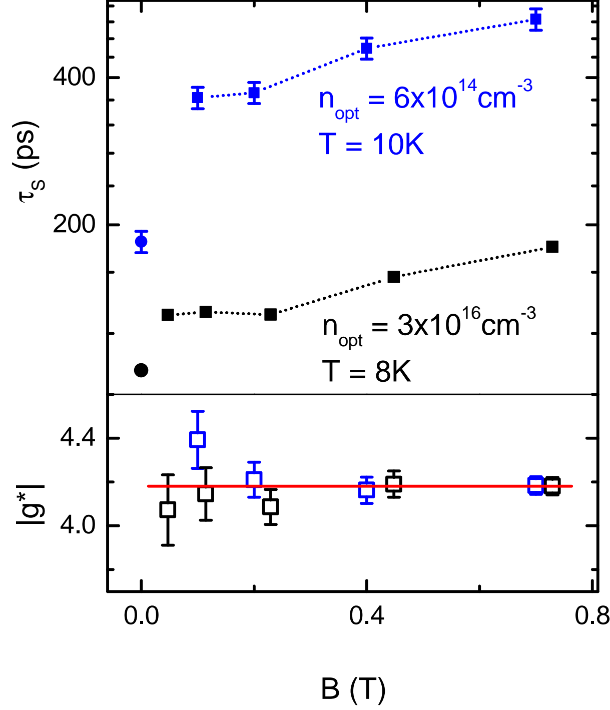

FIGURE 4.15 *Magnetic field dependence of spin relaxation at low temperatures for* $n_{opt} = 3 \times 10^{16}\,\mathrm{cm}^{-3}$ *(black data points) and* $n_{opt} = 6 \times 10^{14}\,\mathrm{cm}^{-3}$ *(blue data points). The central photon energy of incident pump and probe pulses is* 0.8 eV. *Upper panel (logarithmic ordinate): Spin relaxation time. The error bars to the data at higher excitation density are indicated by the size of the data points. The dotted lines are guides to the eye. Lower panel: effective Landé factor. The solid line is the average value.*

$\Delta\varphi = (\varphi_2 - \varphi_1)$, according to[6]

$$FR(t) = \sum_{i=1}^{2} A_i \times \exp(-t/\tau_{si}) \times \cos[(\omega_L) \times t + \varphi_i]\,. \tag{4.10}$$

The fit according to equation (4.10) is included in figure 4.15 as a solid line. The relevant fitting parameters are $A_1/A_2 = 2$, $\tau_{s1} = 170\,\mathrm{ps}$, $\tau_{s2} = 1\,\mathrm{ns}$ and $\Delta\varphi = \pi$. For the transient in $B = 2.1\,\mathrm{T}$, similar parameters are extracted: $A_1/A_2 = 1.4$, $\tau_{s1} = 150\,\mathrm{ps}$, $\tau_{s2} = 1\,\mathrm{ns}$ and $\Delta\varphi = 0.7\pi$. The phase difference of $\sim\pi$ is very interesting in consideration of a time-resolved FR analysis in GaAs by Hohage et al. [Hoh06]. Their experiments at $T = 5\,\mathrm{K}$ rely on tunable pulses with a comparatively narrow spectral width of 0.5 meV, and reveal a phase reversal tuning the laser pulses from the bandgap towards higher photon energies. For excitation at the absorption edge,

[6] To guarantee reasonable acquisition times, the FR transients at $B = 1.4\,\mathrm{T}$ and $B = 2.1\,\mathrm{T}$ are raw data corresponding to one circular polarisation. The polarisation-independent background is accounted for by an additional exponential decay in the fit function. This is omitted in (4.10) since it is not of physical relevance here.

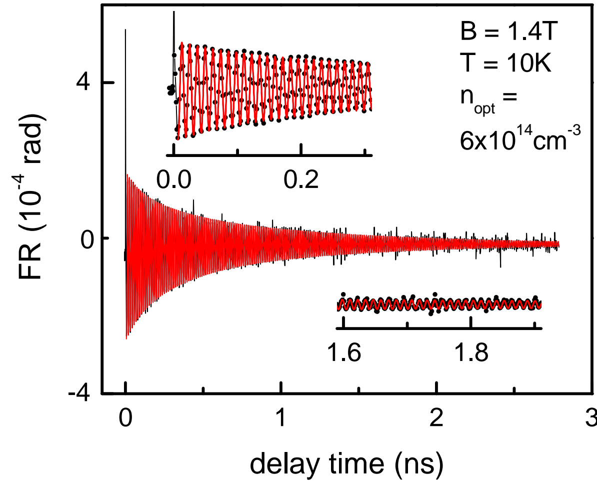

FIGURE 4.16 *FR transient at $T = 10\,\mathrm{K}$ in a magnetic field of $1.4\,\mathrm{T}$ after excitation of $6 \times 10^{14}\,\mathrm{cm}^{-3}$ electron-holes pairs. The line is a fit to the data according to model function (4.10). The insets are magnified views at short (upper left) and long (lower right) delay times.*

they observe $\tau_s \sim 20\,\mathrm{ns}$ and attribute the FR signal to donor-bound electrons, while for excitation with higher photon energies, τ_s decreases to $\sim 500\,\mathrm{ps}$ and itinerant electrons are stated responsible for the FR signal. The two signal components with a phase difference of $\sim \pi$ found in the present investigation could therefore stem from a mixture of both species. The coherence time of $\sim 1\,\mathrm{ns}$ for the potentially donor-bound electron spin polarisation is short compared to the maximum τ_s of the order of $100\,\mathrm{ns}$, that is reported for n-type GaAs (cf. overview of literature data 4). In principle, the strength of the hyperfine interaction is presumably stronger in $In_{0.53}Ga_{0.47}As$ than in GaAs due to the involved nuclei. The isotopic spin quantum numbers for the stable isotopes of Gallium and Arsenic is $I = -3/2$, whereas for Indium it is $I = 9/2$. In addition, the exact value of τ_s depends crucially on the exact value of the correlation time and its density dependence. The latter sets the crossover from spin relaxation dominated by hyperfine or anisotropic exchange interaction (cf. section 2.3). In total, electron capture by donors can possibly – albeit somewhat speculatively due to the limited available data – explain the FR transients at higher magnetic fields.

4.3 Summary

Polarisation-resolved pump-probe measurements in the direct-gap (bulk) semiconductors GaSb and $In_{0.53}Ga_{0.47}As$ reveal (i) electron effective Landé factors consistent with literature results from spin resonance measurements and (ii) that electron spin relaxation is mostly dominated by the D'yakonov-Perel' mechanism. In particular, the impact of spin-orbit coupling on electron spin relaxation becomes evident when comparing relaxation times in both materials. GaSb is a model system for strong spin-orbit coupling, spin relaxation at room temperature occurs within some ps.

The relevant band parameters of $In_{0.53}Ga_{0.47}As$ are comparable to those of GaSb except for the weaker spin-orbit coupling, and room temperature spin relaxation times of up to 40 ps are observed. The present results are based on two variable n-doped and an undoped GaSb sample(s), as well as an n-type $In_{0.53}Ga_{0.47}As$ sample. In particular, electron spin coherence in both materials is optically detectable in the telecom wavelength band around 1.55 μm, which is interesting for device applications. Material-specific key results are recapitulated in the following.

Gallium antimonide The relatively strong spin-orbit coupling in GaSb enhances the room temperature electron spin relaxation rate by a factor of 6 as compared to $In_{0.53}Ga_{0.47}As$ and more than a factor of 10 as compared to literature values for the prototypical material GaAs. Spin relaxation times range from $(1-30)$ ps depending on temperature, doping concentration and optically induced carrier density. A significant portion of the observations is in agreement with a well-known analytical formulation of D'yakonov-Perel' relaxation within a reasonable parameter range. In particular, the spin relaxation times are consistent with the model in all samples at room temperature, and also in the n-doped samples at low temperatures, where the electron distribution is degenerate. However, the low temperature spin relaxation times observed in the nominally undoped sample are orders of magnitude shorter than the model prediction. Such a finding confirms that the underlying description of the electron distribution by unperturbed material properties fails. In addition, the electron effective Landé factor of $|g^*| = 9 \pm 1$ is determined in the nominally undoped sample at room temperature.

Indium gallium arsenide In $In_{0.53}Ga_{0.47}As$, the crossover from the motional narrowing to the ballistic regime of D'yakonov-Perel' spin relaxation is observed at room temperature. For moderate optically induced carrier densities – that is in the motional narrowing regime – the electron effective Landé factor is $|g^*| \sim 3.8$. The dependences of the spin relaxation time on magnetic-field magnitude and temperature is qualitatively and quantitatively consistent with the analytical D'yakonov-Perel' model mentioned above. In the ballistic regime, both the absolute value of the effective g factor and the spin relaxation time decrease with increasing excitation density. In proximity of liquid helium temperature, the low temperature effective Landé factor known from electron spin resonance measurements is affirmed with $|g^*| \sim 4.2$. The values of τ_s and the dependences on the excitation density and magnetic-field magnitude are in good agreement with literature results on D'yakonov-Perel' relaxation of optically induced, itinerant electrons in the prototypical and related material GaAs. At magnetic fields > 1 T the data indicate electron capture to donor sites and subsequent spin relaxation. Due to the spectrally broad excitation, the observed spin relaxation times, however, remain two orders of magnitude below the ~ 100 ns reported in literature for donor-bound electron spins in comparably doped GaAs samples.

5 Spin dynamics in the indirect-gap semiconductor germanium

The present chapter addresses the dynamics of photogenerated carrier spin polarisations in the indirect-gap (bulk) semiconductor Ge. In particular, previously unaddressed questions about carrier spin injection and readout via indirect optical transitions are examined, and the impact of the multivalley conduction band on the dynamics of photogenerated electron spins is investigated. As mentioned in the introduction, in both, silicon and germanium, relatively long electron spin relaxation times occur when compared to direct-gap semiconductors. The inversion-symmetric crystal structure not only excludes D'yakonov-Perel' relaxation, but also relaxation via anisotropic exchange interaction. In addition, the prevailing isotopes are spinless, which suppresses relaxation via hyperfine interaction (cf. section 2.3). As a result, at temperatures as low as 1.3 K, spin-lattice relaxation times of 10^3 s in silicon [Wil61] and 10^{-3} s in Ge [Wil64] are reported from spin resonance measurements on donor-bound electrons in accordance with direct and Raman-type spin-lattice interactions [Has60, Rot60]. Also hole spins are expected to relax comparatively slow. A theoretical investigation of hole spin relaxation in Ge predicts relaxation times up to 500 ps [Dar05]. Specifically, that is is two orders of magnitude longer than in typical direct-gap semiconductors [Hil02, Yu05, She10]. Although silicon as the core material of conventional electronics is probably more interesting in view of device applications, in the present study, Ge is selected due to the following reasons. First, optical transitions can be induced predominantly across the indirect as well as across the direct bandgap with the available photon energies. Second, Ge exhibits relatively strong spin-orbit coupling. As a result, the elements of the electron effective g tensor are comparatively different. In particular, $g_t - g_l = 1.1$ in Ge compared to $g_t - g_l = -10^{-3}$ in silicon, as reported from the electron spin resonance measurements quoted above. Thus, in Ge, the impact of the tensor character on electron spin precession and decoherence is much stronger, and can be detected within the accessible delay time of the present (typical) magneto-optical pump-probe setup.

The results on carrier spin dynamics in Ge are presented as follows. After a short overview of relevant sample parameters and experimental details, both the origin of spin-dependent response as well as the impact of excitation conditions is discussed in section 5.1. The data implies that hole and electron spin dynamics are accessible. The dynamics of both species are subsequently investigated in sections 5.2 and 5.3 with regard to effective Landé factor/Landé tensor and coherence times. Parts of the chapter have been published as [Hau11, Hau12].

Sample properties – surface orientation and electronic properties The Ge samples are commercial optical grade n-type wafers with thicknesses in the range of 1 mm. The surfaces of samples A1 and A2 are oriented normal to $[1,0,0]$, according to the manufacturer (Umicore Electro-Optic Materials). The surface orientation of sample B (Edmund Optics) is determined by X-ray structure analysis relying on conventional θ-2θ detection of the X-rays emitted from a molybdenum tube and reflected from the sample surface[1]. Figure 5.1 depicts the counts detected by the utilised Geiger-Müller counter versus the angle of incidence θ. Evaluation of the diffraction data[2] reveals

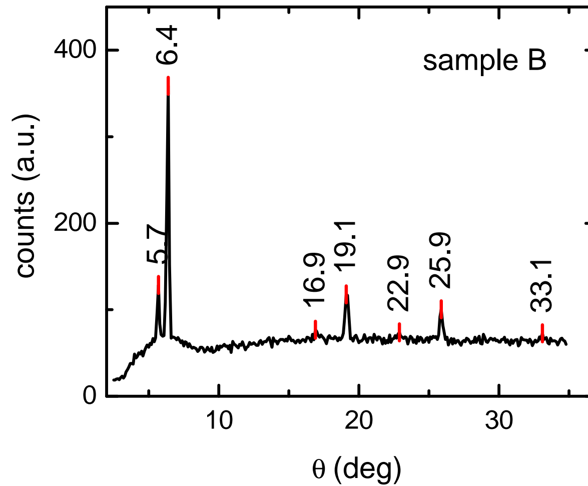

FIGURE 5.1 *X-ray diffraction pattern of sample B. The detector counts indicate the amount of radiation diffracted at the sample surface and are plotted against the angle of incidence θ.*

that the surface is oriented normal to $[1,1,1]$ with an accuracy of 1 %. Note that this accuracy expresses the resolution limit of the experiment. The surface orientation of wafers is typically exact within 0.1 %, as is stated by the manufacturer for samples A1 and A2.

Concerning the electronic properties, the donor concentration is in the range $n_D \sim 10^{13}\,\mathrm{cm}^{-3}$ for samples A1 and B, whereas sample A2 is comparatively highly doped with $n_D \sim 10^{16}\,\mathrm{cm}^{-3}$. The resulting electronic properties at room temperature are included in table 5.1 together with the respective surface orientations and sample thicknesses d. The data for samples A1 and A2 – that are doped with Antimony (Sb) – is again as specified by the manufacturer. Resistivity (ρ) and Hall mobility measurements reveal carrier (equals donor) concentration and polarity.

Experimental details For time-resolved transmission measurements, the samples are mounted in an optical cryostat, conductive lacquer is used as an additional support and to ensure good heat contact. For the data in sections 5.1 and 5.2 the Cryovac cryostat is used. The magnetic

[1]The X-ray setup of the Physikalisches Anfängerpraktikum at the Technische Universität München was used http://www.ph.tum.de/studium/praktika/ap/versuche/roen with the kind permission of Dr. Martin Saß.

[2]For details, refer to, e.g., [Kop04].

sample	surface orientation	$\rho[\Omega\text{cm}]$	$n_d[\text{cm}^{-3}]$	dopand	d[mm]
A1	$\langle 100 \rangle$	66 ± 3	$(2.2 \pm 0.1) \times 10^{13}$	Sb	0.55
A2	$\langle 100 \rangle$	0.045 ± 0.005	$(6 \pm 1) \times 10^{16}$	Sb	0.35
B	$\langle 111 \rangle$	20 ± 1	$(6 \pm 2) \times 10^{13}$	?	1.5

Table 5.1 *Ge samples parameters. Samples A1 and A2: Umicore Electro-Optic Materials, surface orientation, resistivity, doping concentration and doping atom according to the manufacturer's data. Sample B: Edmund Optics, surface orientation from X-ray analysis, doping concentration and polarity from resistivity and Hall mobility measurements.*

field is provided by the GMW electromagnet. For the data in section 5.3 temperatures from $T = 10\,\text{K}$ to $T = 250\,\text{K}$ and magnetic fields up to $B = 2.1\,\text{T}$ are provided by the Spectromag® system. Most of the data is recorded relying on the Coherent RegA/OPA system. Hole spin dynamics is additionally investigated with the Toptica FFS as a laser source (cf. section 5.2, the data is marked accordingly). Carrier spin dynamics is only investigated via FR, since the polarisation bridge could not be balanced with a quarter-wave plate. The reason are presumably linear magneto-optical effects in the comparatively thick samples.

5.1 Spin-dependent optical response

Owing to the indirect bandgap of Ge spin-dependent optical response is more complex as compared with direct-gap semiconductors. Due to the energetic proximity of Γ- and L-valleys in the conduction band ($\Delta_{\Gamma L} = 0.17\,\text{eV}$ at low temperatures, cf. table 2.2) energies that are resonant with indirect optical transitions intrinsically are not far from being resonant with direct optical transitions. As a result, two plausible mechanisms for optical spin readout exist. Mechanism A: A hole spin population in the Γ-valley can induce Faraday rotation for the present probe photon energies because they are only slightly detuned with respect to the direct bandgap (cf. corresponding results in GaAs [Wes07]) and, thereby, reveal hole spin dynamics. Mechanism B: Any spin-population in the L-valley will affect the corresponding optical transitions via Pauli blocking. This leads to circular dichroism and/or FR for such indirect transitions, reflecting electron spin dynamics in the L-valleys. The FR transients depicted in figure 5.2 indicate that both mechanisms for spin-dependent optical response indeed exist. The transients are recorded in sample B at a crystal temperature of $T = 8\,\text{K}$. Excitation and probing is – as for most of the FR transients discussed in this chapter – predominantly across the indirect bandgap. The corresponding transitions are illustrated in red in the simplified band diagram in figure 5.3. The energy gaps relevant for the ultrafast magneto-optical investigations presented in this work are the fundamental bandgap E_g and the energy gap at the Γ-point E_{Γ_1}. The split-off hole band is not shown. It is located $\sim 0.3\,\text{eV}$ below the top level of the valence band and transitions from this band into the conduction band are effectively not probed. The specified values for E_g and E_{Γ_1} are low temperature values (cf.

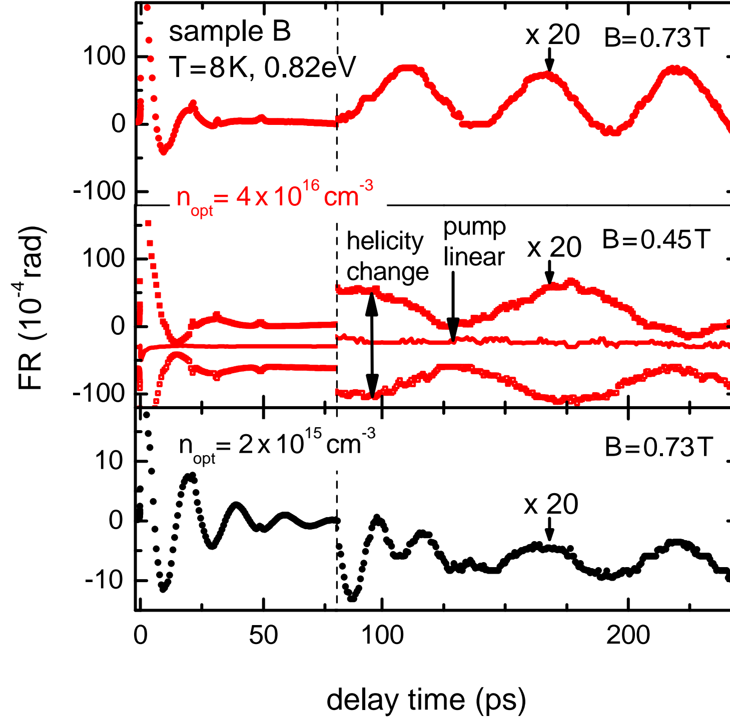

FIGURE 5.2 *Spin-dependent optical response in Ge (sample B) for two different excitation densities (excitation predominantly across the indirect bandgap) and magnetic field magnitudes at $T = 8$ K. The FR transients reveal two spin-carrying species characterised by different initial amplitude, decay time and precession frequency (the amplitude is rescaled for delay times exceeding 80 ps to show the longer-lived species).*

section 2.1). After photo-excitation, holes remain in the Γ-valley while electrons reside in the L-valleys. (For excitation across the direct bandgap, phonon-assisted scattering repopulates the electrons into the L-valleys of the conduction band within less than 1 ps [Ros88].) For the data in figure 5.2 both incident excitation and probe pulses are centred at $\hbar\omega = 0.82$ with a full-width-half-maximum of 0.04 eV. The respective spectral shape is depicted in the right panel of figure 5.3 together with a Gaussian fit that extracts central pulse energy and width (solid line). Note that, indeed, the absorption coefficient of Ge [Iof] varies by three orders of magnitude when comparing the two extreme tails of the laser pulses. The fraction of carriers excited via direct transitions is still minimal since the sample thickness is of the order of the penetration depth of $z_p = 0.5$ mm for the central pulse energy. The transients in figure 5.2 are recorded with two different optically induced carrier densities that specifically are $n_{opt} = 4 \times 10^{16}\,\text{cm}^{-3}$ (upper and second panel) and $n_{opt} = 2 \times 10^{15}\,\text{cm}^{-3}$ (lower panel). Three main observations are encoded in the transients. (i) Two oscillatory signal components of different amplitude and frequency are observed. The amplitudes scale as 100 : 1, the precession frequencies as 3 : 1. The large amplitude, high-frequency component decays on a time scale of $\sim$ 50 ps, while the oscillations of smaller amplitude and lower

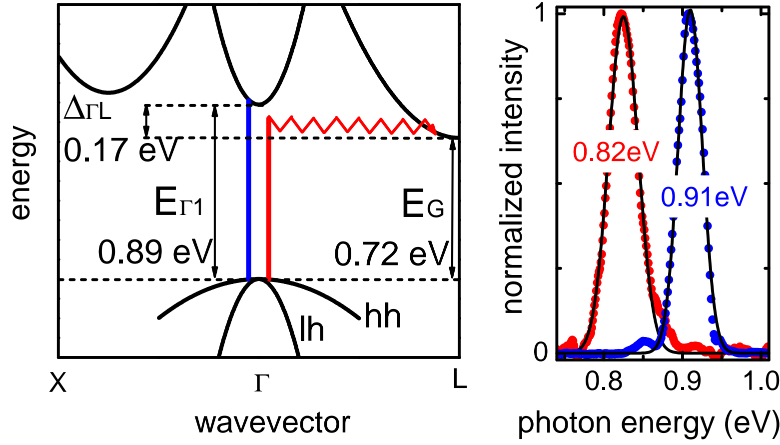

FIGURE 5.3 *Right-hand side: Simplified band structure of Ge indicating excitation with OPA pulses predominantly across the indirect bandgap (central photon energy* 0.82 eV*), as well as across the direct bandgap (central photon energy* 0.91 eV*). Left-hand side: spectral shape of the laser pulses. Solid lines: Gaussian fits.*

frequency persist beyond 200 ps. (The signal amplitude is rescaled by a factor of 20 for delay times exceeding 80 ps). (ii) When the magnetic field is lowered from $B = 0.73\,\mathrm{T}$ to $B = 0.45\,\mathrm{T}$ (cf. upper and second panel), the oscillation period increases as expected for carrier spin polarisations that exhibit coherent Larmor precession. The oscillatory FR signals reverse sign upon changing the helicity of the exciting laser pulses, while they are absent for the case of pumping with linearly polarised light (cf. sample traces in the second panel). (iii) The high-frequency oscillation is strongly damped for the stronger excitation condition while the low-frequency oscillation still shows virtually no damping beyond 200 ps (cf. upper/second panel and lower panel, respectively). These observations give evidence that circularly polarised optical excitation of bulk Ge generates two different and rather long-lived species, which both exhibit coherent Larmor precession with significantly different effective g factors. As will be corroborated in sections 5.2 and 5.3, there is substantial evidence that the faster decaying part of the signal reveals hole spin coherence – that is typically not resolved in bulk III-V semiconductors – whereas the long-lived part is related to electron spin coherence. The amplitudes of hole and electron spin signatures indicate that mechanism A (that reveals electrons spins in the L-valleys) is two orders of magnitude weaker than mechanism B (that reveals hole spins in the Γ-valley). Prior to detailed investigations on hole and electron spin dynamics, it is instructive to compare (i) excitation predominantly across the direct bandgap to excitation predominantly across the indirect bandgap and (ii) the magnitude of the magneto-optical response per photogenerated electron to the situation in III-V semiconductors. Figure 5.4 shows respective electron spin signals from sample B at $T = 8\,\mathrm{K}$. The transients are extracted from the difference between the signals for $\sigma+$ and $\sigma-$ polarised excitation to remove a slowly varying background. The transient in the upper panel is recorded after excitation of $n_{opt} = 4 \times 10^{16}\,\mathrm{cm}^{-3}$ electron-hole pairs predominantly across the indirect bandgap. As for the data in figure 5.2 above,

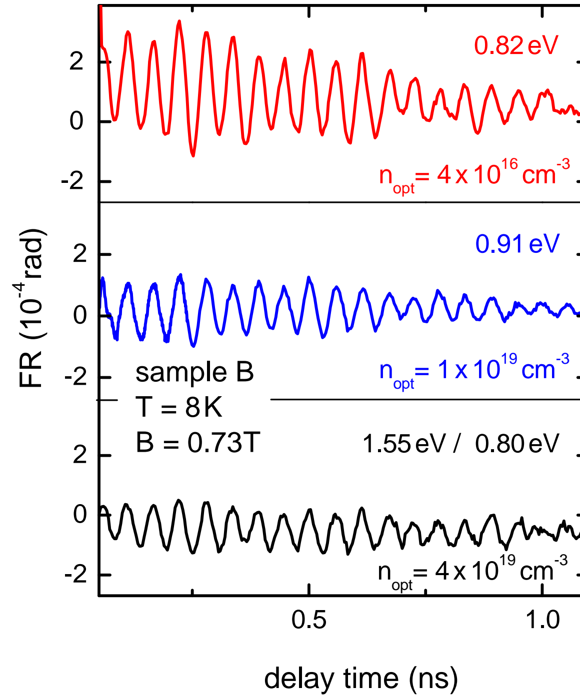

FIGURE 5.4 *Electron spin precession in sample B detected with different pump/probe configurations. The sample is cooled to $T = 8\,\mathrm{K}$ and exposed to $B = 0.73\,\mathrm{T}$. Upper panel: Excitation predominantly across the indirect bandgap. Pump and probe pulses centred at 0.82 eV. Second and lower panel: Excitation across the direct bandgap. Pump and probe pulses centred at 0.91 eV (second panel) or pump pulses centred at 1.55 eV and probe pulses centred at 0.82 eV (lower panel).*

the OPA is tuned to photon energies centred at 0.82 eV. In contrast, the transients in the second and lower panel are recorded after excitation across the direct bandgap. For the data in the second panel the OPA is tuned to $(0.91 \pm 0.02)\,\mathrm{eV}$. These photon energies exceed $E_{\Gamma_1} = 0.89\,\mathrm{eV}$, so that absorption occurs predominantly via direct optical transitions. Both excitation schemes are illustrated in figure 5.3. The spectral shape of the incident pump and probe pulses is included in the right panel of the figure together with a Gaussian fit. The transient in the lower panel of figure 5.4 is recorded after excitation with RegA pulses centred at 1.55 eV. As before the probe pulses are delivered by the OPA and centred at 0.82 eV. The electron spin signal is detected in all three pump/probe configurations. This can be understood recalling that a population of electrons at the L-point (and holes at the Γ-point) is effectively produced regardless of whether carriers are excited predominantly across the direct or the indirect-gap. The difference – that, however, does not affect the readout of the electron spins – lies in the initial states of electron repopulation within the conduction band. These are either located in the Γ-valley (excitation predominantly across the direct gap), or are virtual states (excitation predominately across the indirect gap, cf. section 2.2). The signal amplitudes as well as the decay times of the transients in figure 5.4 are of the same

order of magnitude. Naturally, excitation across the direct bandgap leads to higher densities of photogenerated carriers when using similar irradiances. Specifically, n_{opt} is more than two orders of magnitude higher for excitation with pulses centred at 0.91 eV and at 1.55 eV as compared to excitation across the indirect bandgap. The robustness of the electron spin signal against strong excitation conditions is thus further corroborated. As a side remark, no hole spin signal is resolved after excitation with pulses centred at 1.55 eV in contrast to excitation predominantly across the indirect bandgap and excitation with pulses centred at 0.91 eV. (This information is not included in figure 5.4. The transients are shown for delay times exceeding 50 ps which is beyond the lifetime of the hole spins at the present excitation densities, cf. section 5.2.2.) The lack of hole spin signature after excitation with pulses centred at 1.55 eV might originate from the possibility to excite split-off holes (the corresponding transitions are only accessible by the excitation pulses and, as stated before, not by the probe pulses). The admixture of split-off holes seems to prevent hole spin polarisation. Turning the focus back to the electron spin signal, the magnitude of the magneto-optical response per photogenerated electron can be estimated, assuming that each pump photon that is absorbed in the sample promotes one electron to the conduction band. For excitation with pulses centred at 0.82 eV, in the following referred to as configuration 1, the FR signal per photon per spot area is approximately $1 \times 10^{-19}\,\mathrm{cm}^2$. Comparing the various excitation conditions, the FR signals per areal density are in a $1 : 1/2 : 1/2$ ratio for excitation with pulses centred at 0.82 eV, 0.91 eV (configuration 2) and 1.55 eV (configuration 3), respectively, since the sample is optically thick for all three excitation conditions and comparable pump fluences are used. It is instructive to compare these values of the FR signal per areal density in Ge to typical values in III-V semiconductors. For a precise result, FR transient in Ge and in $In_{0.53}Ga_{0.47}As$ are recorded subsequently under the exactly same experimental conditions (in particular, spot size, temperature and magnetic field magnitude). The FR signal per photon areal density in $In_{0.53}Ga_{0.47}As$ is $3 \times 10^{-16}\,\mathrm{cm}^2$. This value is 3 orders of magnitude larger than the values stated above for Ge. Estimates based on FR transients in $In_{0.53}Ga_{0.47}As$ and GaSb recorded at various temperatures consistently yield $2-3$ orders of magnitude larger FR signal per photon areal density in the direct-gap materials. As discussed in section 2.2, in typical III-V semiconductors an electron spin polarisation of 50 % is induced by circularly polarised photons with $E_g = \hbar\omega$, and the polarisation degree is not decreased markedly for higher photon energies as long as $\hbar\omega < E_g + \Delta$. Thus, for comparable carrier spin orientation and readout efficiencies in a degenerate pump/probe configuration, the detected FR amplitude corresponds to $P_e \times P_e = 25\,\%$ [Bog00]. Investigating Ge in configuration 1, carrier spin orientation and readout efficiencies are presumably also comparable, since both address indirect optical transitions. Consequently, the comparison of the FR signals per areal density in the direct-gap semiconductors and Ge indicates an electron spin polarisation of approximately 1 % for excitation predominantly across the indirect bandgap of Ge. Note that, recently, Guite and Venkataraman extracted a somewhat higher orientation efficiency of $\sim 5\,\%$ for excitation with

$\hbar\omega = 0.92\,\text{eV}$ across the direct bandgap of Ge [Gui11][3]. Such values are, in terms of magnitude, in line with the theoretical results on optically induced electron spin polarisation versus excess energy in silicon by Cheng et al. [Che11, cf. section 2.2]. In particular, the electron spin polarisation is considerably smaller than the value of 50 % for excitation just above the fundamental bandgap of Ge. This is expected at the present excess energy of $\sim 0.1\,\text{eV}$, that exceeds the phonon energies by approximately a factor of 3. The orientation efficiency in configuration 2 and 3 can not be quantified as easily, since FR is again detected via indirect optical transitions (in configuration 2, FR is detected by the extreme long-wavelength tail of the probe pulses around 0.86 eV since the penetration depth at 0.91 eV is only $2\,\mu\text{m}$). However, the comparable magnitudes of magneto-optical response for all three pump-probe configurations indicate that the efficiency of optical orientation does not substantially differ for excitation across the direct and the indirect bandgap.

5.2 Hole spin dynamics

In the present section, the spin carrying species claimed as holes in the Γ-valley is investigated. After presenting typical raw data, the effective Landé-factor is discussed in section 5.2.1. The coherence time of the hole spin signal is analysed in section 5.2.2. First, the influence of magnetic field magnitude and optically induced carrier densities is addressed. Second, zero-field transients recorded with various excitation densities and different central pulse energies are evaluated. The impact of the repetition rate is discussed based on complementary measurements relying on the fibre laser. Finally, the dependence of the coherence time on crystal temperature is evaluated.

Characteristic raw data for hole spin coherence is shown in figure 5.5 without external magnetic field and for two different field magnitudes ($B = 0.45\,\text{T}$ and $B = 0.73\,\text{T}$). As most of the data discussed in this section, the transients are recorded in sample B after excitation predominantly across the indirect bandgap while the crystal is cooled to $T = 8\,\text{K}$. The initial carrier density is $n_{opt} = 8 \times 10^{14}\,\text{cm}^{-3}$. The zero-field FR signal is scaled logarithmically to show the peak at time overlap of excitation and probe pulses. The width as well as the decay time of the initial peak is approximately 0.5 ps, and its amplitude is typically 10 to 20 times stronger than the initial amplitude of the hole spin signal. Possible reasons for signals close to the time overlap include two-photon absorption involving pump and probe photons, as well as hot carrier relaxation [Sha89]. In addition, the peak may include heavy-hole spin dynamics (cf. discussion below). After the sub-picosecond decay, the experimental data is fitted well by a mono-exponential decay for $B = 0$ and by exponentially decaying cosine functions for $B \neq 0$. The fits are indicated as solid lines in figure 5.5 and reveal decay times as well as the effective g factor (in case $B \neq 0$).

[3] In the referred experiment, the polarisation direction of optically induced electron spins was modulated using an electro-optical modulator driven by a radio frequency voltage, and the modulated spin polarisation was detected electrically by a radio-frequency coil.

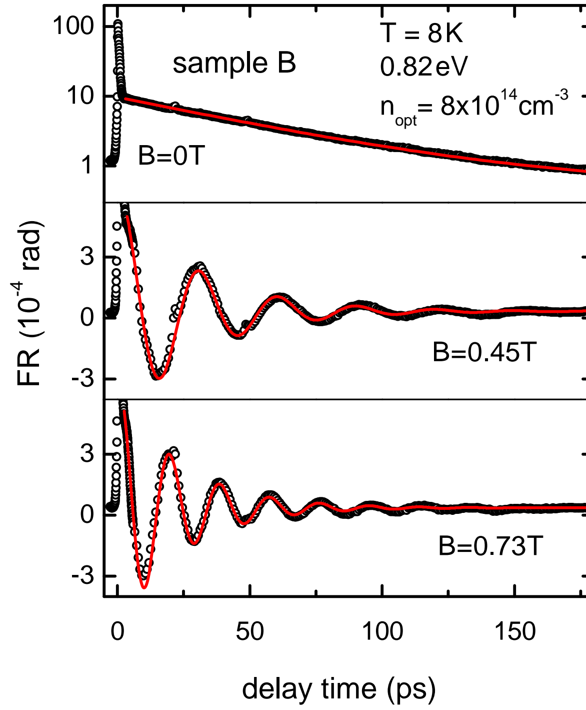

FIGURE 5.5 *FR transients mapping hole spin coherence in sample B at* $T = 8\,\mathrm{K}$ *after excitation of* $n_{opt} = 8 \times 10^{14}\,\mathrm{cm}^{-3}$ *electron-hole pairs. The central photon energy of the incident pump- and probe pulses is* $\hbar\omega = 0.82\,\mathrm{eV}$ *and sample is cooled to* $T = 8\,\mathrm{K}$. *Solid lines: mono-exponential or exponentially decaying cosine fits.*

5.2.1 Effective Landé factor

To gain information about the hole effective g factor, transients for up to five different magnetic field amplitudes (from $B \sim 0.2\,\mathrm{T}$ to $B \sim 0.7\,\mathrm{T}$) are evaluated for various excitation conditions. As indicated in section 5.1 and discussed in detail in the following section 5.2.2, the longest hole spin coherence times are observed with comparatively low excitation densities and at low crystal temperatures. Consequently, $|g^*|$ can be determined most accurately under such conditions. figure 5.6 plots the values of $|g^*|$ extracted from transients recorded at $T = 8\,\mathrm{K}$ after excitation predominantly across the indirect bandgap with pulses centred at $0.82\,\mathrm{eV}$. The resulting excitation densities range from $\sim 2 \times 10^{14}\,\mathrm{cm}^{-3}$ to $\sim 4 \times 10^{16}\,\mathrm{cm}^{-3}$. The error bars in figure 5.6 include statistics from comparing various magnetic field magnitudes as well as a 1% uncertainty in the latter (cf. section 3.2). The solid line is a linear fit to the data. It reveals $|g^*| = 5.7 \pm 0.2$. Transients recorded after excitation across the direct bandgap – with $n_{opt} \geq 10^{17} cm^{-3}$ – and after excitation with fibre laser pulses yield consistent values of $|g^*|$, yet contain bigger uncertainty due to smaller statistics and/or shorter decay times (data not shown). The same is true for sample A1, while in the more strongly doped sample A2, no hole spin signal is detected. The latter finding points towards a strong influence of impurity scattering on hole spin relaxation. In particular, after excitation

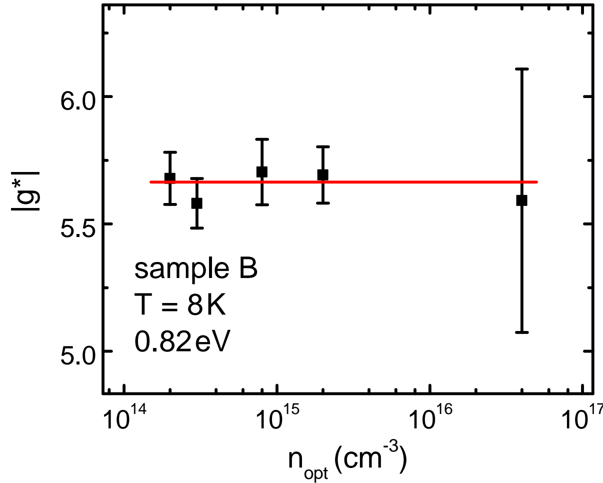

FIGURE 5.6 *Hole effective Landé factor. The corresponding FR transients are recorded in sample B at $T = 8\,\mathrm{K}$ and in various magnitudes of the external magnetic field. The solid line indicates the average value.*

across the direct bandgap, $T_2^* \sim 20\,\mathrm{ps}$ is observed in sample B for n_{opt} ranging from $10^{17}\,\mathrm{cm}^{-3}$ to $10^{19}\,\mathrm{cm}^{-3}$ (cf. data in section 5.2.2) although these optically induced carrier densities exceed the doping density of sample A2 by up to 2 orders of magnitude. An effective g factor of ~ 5.7 is inconsistent with the expectation for L-valley electrons taking into account the present spin-orbit coupling (cf. the $\boldsymbol{k}\cdot\boldsymbol{p}$-approximation (2.10) and the investigation of the L-valley Landé tensor in section 5.3). For electrons in the Γ-valley, $g = -3.0 \pm 0.2$ is reported from magneto-reflectance measurements [Agg70]. The same experiment revealed $g = -10 \pm 3$ for split-off holes. Combined spin-cyclotron resonance measurements in strained Ge indicate $g = 2\kappa = 7.20 \pm 0.08$ for light holes [Hen68], where κ is one of the Luttinger parameters [Lut55]. Roth et al. used a somewhat lower value of $\kappa = 3.266$ to match their experimental magneto-absorption spectra [Rot59]. The value of $|g^*| = 5.7 \pm 0.2$ extracted from the faster decaying component of the FR transients is thus closest to the literature results for light holes. Note that the optical orientation process induces three times more heavy hole spins than light hole spins, and carrier scattering from the heavy hole to light hole band is typically faster than vice versa [Sch95]. A possible explanation why heavy hole spins are not detected in the present measurements is a comparatively fast decay of heavy hole spin polarisation. Indeed, simulations of hole spin coherence in Ge result in faster relaxation of heavy hole spins as compared to light hole spins [Dar05]. However, the relaxation times predicted for conditions comparable to those of the present experiment are some picoseconds, which exceeds the initial sub-picosecond decay by one order of magnitude.

5.2.2 Coherence time – dependences on magnetic field, excitation conditions and temperature

Figure 5.7 depicts decay times of FR transients for various magnetic fields and optically induced carrier densities. As in the further course of the present section, instead of τ_s, the notation T_2^* and $\tau_{B=0}$ is used for decay times extracted from transients with and without external magnetic field, respectively. The data in figure 5.7 is extracted from the FR transients, that are also used for the analysis of the effective Landé factor in the previous section (specifically, the transients are recorded at $T = 8\,\mathrm{K}$ with pulses centred at $\hbar\omega = 0.82\,\mathrm{eV}$).

Magnetic field dependence As seen in figure 5.7, longer decay times are found without magnetic field when compared to data with magnetic field ($\tau_{B=0} > T_2^*$), and the coherence time further decreases with increasing B. As an example, at the lowest investigated excitation density – that is $n_{opt} = 2 \times 10^{14}\,\mathrm{cm}^{-3}$ – the coherence time without external magnetic field is $\sim 80\,\mathrm{ps}$ compared to $T_2^* \sim 30\,\mathrm{ps}$ in $B = 0.73\,\mathrm{T}$. Due to the center of inversion inherent to the Ge crystal, DP relaxation does not occur, and EY-type relaxation probably dominates spin relaxation (cf. section 2.3). There are two possible explanations for a magnetic-field mediated enhancement of spin decoherence. The first is indeed EY relaxation in the limit of strong mixing of the spin eigenstates. In this context, a model including certain points in the band structure, where the mixing is largely enhanced – known as spin hot spots – e.g. reproduces the experimentally observed decrease of the spin relaxation time with increasing magnetic fields in metals [Ẑut04]. In consideration of the stronger influence of spin-orbit coupling on holes when compared to conduction band electrons, stronger mixing – and thus, a decrease of the coherence time with increasing B – is plausible for hole spins. The second explanation lies in the $\boldsymbol{k}$-dependence of the Landé factor, that is presumably strong in the anisotropic and degenerate hole band, and might consequently dominate spin relaxation even at comparatively low magnetic-field magnitudes. As mentioned in the discussion of magnetic-field dependent spin relaxation in $In_{0.53}Ga_{0.47}As$, such an effect is found to reduce the electron spin relaxation time upon increasing B (cf. section 4.2.1 and references therein). It is furthermore instructive to compare the value of $\tau_{B=0}$ with the simulations on hole spin decoherence by A. Dargys [Dar05]. His calculations are based on EY-like spin relaxation mediated by momentum scattering between valence band states. The result is $(300-2)\,\mathrm{ps}$ for heavy hole spins and $(500-20)\,\mathrm{ps}$ for light hole spins. The long values are valid for hole kinetic energies up to $10\,\mathrm{meV}$, whereas the short hold at approximately $250\,\mathrm{mV}$. In the present experiment, holes are excited with excess energies of $\sim 100\,\mathrm{meV}$ corresponding to a spin relaxation time of $\sim 100\,\mathrm{ps}$ for light holes and $5\,\mathrm{ps}$ for heavy holes. As mentioned, the latter is somewhat too long to exclusively explain the lack of heavy hole spin signature in the FR transients. The former, however, is in good agreement with the experimentally observed (light hole) coherence time at relatively moderate excitation conditions (cf. figure 5.7 and additional data at weaker excitation conditions shown in the following). As mentioned at the beginning of the of the present chapter, such hole spin relaxation

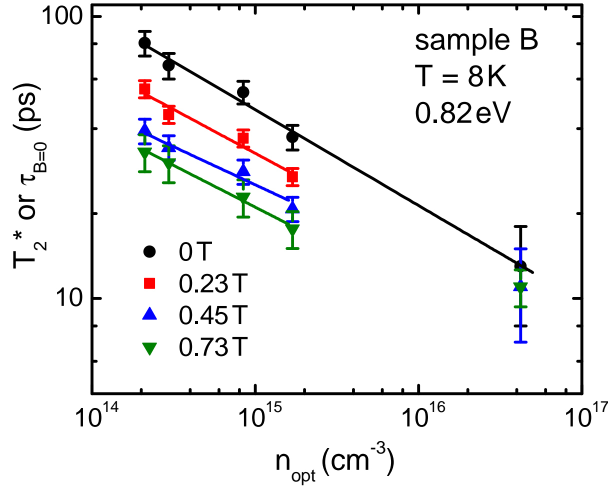

FIGURE 5.7 *Dependence of the spin coherence time with and without external magnetic field for various optically induced carrier densities and magnetic field magnitudes. The corresponding FR transients are recorded at $T = 8\,\mathrm{K}$ with pulses centred at $\hbar\omega = 0.82\,\mathrm{eV}$. The lines are power law fits.*

times are two orders of magnitude longer than theoretical prediction for low-temperature hole spin relaxation times in typical direct-gap semiconductors [Yu05, She10]. In particular, so far, no such long-lived hole spin signature has been observed in a bulk semiconductor.

Influence of excitation conditions Besides the dependence on B, the data depicted in figure 5.7 reveal that the hole spin coherence time is strongly affected by elevated carrier densities. The n_{opt}-dependence of the spin coherence time both with and without external magnetic field is well approximated by power law fits according to $\tau_{B=0}(\text{or } T_2^*) \propto n_{opt}^{-0.3}$. The fits are included as solid lines in figure 5.7. Note that – except for the highest density of $4 \times 10^{16}\,\mathrm{cm}^{-3}$ – the n_{opt} are well below the Mott density of $\sim 10^{16}\,\mathrm{cm}^{-3}$, at which the insulator-to-metal transition takes place in Ge at low temperatures [Bal85]. Consequently, maintaining the reasonable assumption of momentum-scattering mediated – or EY-like – spin relaxation, long-range carrier-carrier scattering apparently strongly influences hole spin dynamics. For excitation predominantly across the direct bandgap with pulses centred at $0.91\,\mathrm{eV}$ and n_{opt} ranging well above the Mott density from $(10^{17} - 10^{19})\,\mathrm{cm}^{-3}$, the hole spin signal is found to decay within $\sim 20\,\mathrm{ps}$ independent of n_{opt} (cf. blue triangles in figure 5.8). Focussing again on excitation predominantly across the indirect bandgap, hole spin coherence is even more robust for excitation with pulses centred at $0.80\,\mathrm{eV}$, i.e., closer to the indirect bandgap of Ge. The corresponding $\tau_{B=0}$ are depicted as orange squares in figure 5.8 and are $\sim 10\,\%$ longer than those found with a central pulse energy of $0.82\,\mathrm{eV}$ (cf. circles in figure 5.7). The trend towards longer spin coherence at reduced excess energies is in line with the proposed picture of EY-type hole spin relaxation. As for excitation with $\hbar\omega = 0.82\,\mathrm{eV}$, the $\tau_{B=0}$ found with $\hbar\omega = 0.80\,\mathrm{eV}$ are proportional to $n_{opt}^{-0.3}$, the corresponding fit

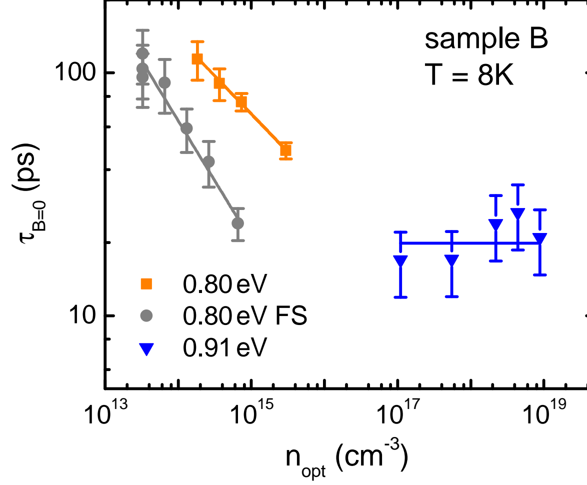

FIGURE 5.8 *Spin coherence times at zero magnetic field and $T = 8\,\mathrm{K}$ for various excitation conditions. Orange squares and grey circles: excitation predominantly across the indirect bandgap with pulses centred at $0.80\,\mathrm{eV}$ from the OPA and the fibre laser, respectively. The colour-coded lines are power law fits. Blue triangles: excitation predominantly across the direct bandgap with pulses centred at $0.91\,\mathrm{eV}$. The line is a guide to the eye.*

is shown together with the data. In contrast, coherence times extracted from transients relying on the Toptica FFS as a laser source follow a stronger dependence proportional to $n_{opt}^{-0.5}$. The fibre laser data is included in figure 5.8 as circles together with the corresponding power law fit as a solid line. The differences can be attributed to carrier accumulation effects, as optically induced carriers in Ge recombine with a decay period of approximately $1\,\mu\mathrm{s}$ [Cho77]. The electron-hole recombination time is thus shorter than the time between subsequent pulses from the OPA – that is $1/f_{rep} = 1/250\,\mathrm{kHz} = 4\,\mu\mathrm{s}$ – but two orders of magnitude longer than $1/90.5\,\mathrm{MHz} = 11\,\mathrm{ns}$ from the fibre laser.

Temperature dependence The discussion so far addressed hole spin coherence at a crystal temperature of $T = 8\,\mathrm{K}$. Figure 5.9 compares the zero-field results for $T = 8\,\mathrm{K}$ after excitation of various densities n_{opt} with pulses centred at $\hbar\omega = 0.8\,\mathrm{eV}$ – the same data is shown in figure 5.8 – to coherence times extracted from transients recorded under the same conditions, except for the lowered temperature. The downward triangles correspond to $T = 6\,\mathrm{K}$, while the upward triangles are the coherence times found at $T = 3\,\mathrm{K}$. In accordance with the marked dependence of hole spin coherence on the excitation conditions discussed so far, the longest decay times within the analysed parameter range are extracted at the most gentle excitation conditions in the analysed parameter range – that is $n_{opt} \leq 2 \times 10^{14}\,\mathrm{cm}^{-3}$ and $T = (3-6)\,\mathrm{K}$. The corresponding values are $\tau_{B=0} \sim 150\,\mathrm{ps}$. The impact of temperature diminishes at higher excitation densities as is evidenced by the matching values of $\tau_{B=0}$ at the highest investigated density $n_{opt} = 3 \times 10^{15}\,\mathrm{cm}^{-3}$. In addition, increasing the temperature to $T = 60\,\mathrm{K}$ reduces hole spin coherence to $\sim 10\,\mathrm{ps}$ (data not shown).

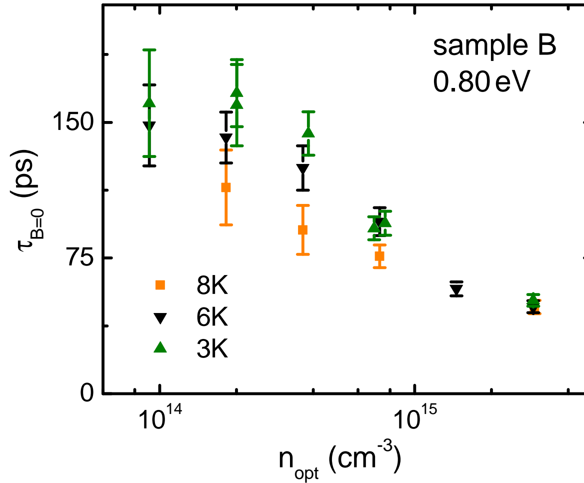

FIGURE 5.9 *Density-dependent hole spin coherence times for various temperatures. The corresponding FR transients are recorded at zero magnetic field after excitation with pulses centred at* 0.8 eV*. Squares:* $T = 8$ K*, data as in figure* 5.8*. Downward triangles:* $T = 6$ K*, upward triangles:* $T = 3$ K.

The observed temperature dependence further underlines the impact of carrier-carrier scattering, that, compared to the situation at $T = 8$ K, is enhanced at $T = 60$ K and reduced at $T = (3-6)$ K in combination with relatively low excitation densities.

5.3 Electron spin precession in the L-valleys

In the present section, electron spin dynamics is discussed comparing samples of different surface orientation and doping concentration (cf. sample parameters in table 5.1). First, electron spin precession is analysed as a function of the in-plane magnetic-field orientation, thereby deducing the effective g tensor for L-valley electrons (section 5.3.1). In section 5.3.2, the temperature dependences of the Landé tensor and the decay of spin coherence are investigated. In section 5.3.3, a rate equation model assuming free conduction band electrons as spin carriers is developed to explain experimentally observed dependences of the decoherence time on temperature, doping concentration and surface orientation, as well as on magnetic-field magnitude (section 5.3.4) and orientation within the sample plane (section 5.3.5).

All FR transients shown in the present section were recorded after excitation of $n_{opt} = (2-4) \times 10^{16}\,\mathrm{cm}^{-3}$ charge carriers predominantly across the indirect bandgap with pulses centred at $\hbar\omega = 0.82$ eV. As shown in the previous section 5.2, at such excitation conditions the hole spin polarisation decays within ~ 10 ps. The relatively long-lived electron spin signature is extracted from the difference between the signals for $\sigma+$ and $\sigma-$ polarised excitation to remove a slowly varying background.

5.3.1 Analysis of the Landé tensor

The panels on the left-hand side of figure 5.10 depict FR transients from sample A1 for three different orientations of the external magnetic field in the sample plane, namely $\alpha_1 = 45$, $\alpha_2 = 118^\circ$ and $\alpha_3 = 140^\circ$ measured against the $[0,1,1]$-direction in the sample plane. The transients are

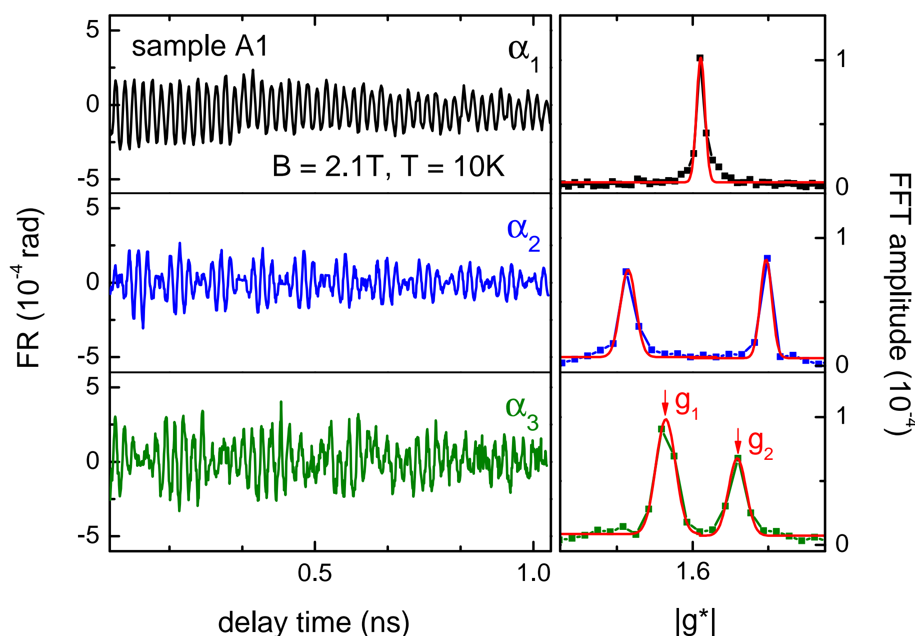

Figure 5.10 *Electron spin signature from sample A1 for three different orientations of $B = 2.1\,\mathrm{T}$ in the sample plane at $T = 10\,\mathrm{K}$. Left-hand side: FR transients. Right-hand side: Corresponding FFT amplitudes. Solid lines: Gaussian fits.*

recorded at low crystal temperature ($T = 10\,\mathrm{K}$) and – to achieve satisfying frequency resolution, cf. data analysis below – with a comparatively high magnetic-field magnitude of $B = 2.1\,\mathrm{T}$. The transients recorded for $\alpha_2 = 118^\circ$ and $\alpha_3 = 140^\circ$ are indicative of a frequency beating, whereas choosing $\alpha = 45^\circ$ results in only one frequency component. The contributing frequency components – or effective g factors – are extracted by applying fast Fourier transformation (FFT) to the transients. The resulting FFT amplitudes are shown in the panels on the right-hand side of figure 5.10. The solid lines are Gaussian fits that reveal the $|g^*|$ (peak position) as well as the corresponding uncertainty Δg^* (half-width-half-maximum, or HWHM). Confirming the qualitative description above, in general, the transients from sample A1 contain two frequency components. The positions of the respective peaks in the FFT amplitude shift upon changing the magnetic-field orientation (as is seen comparing the middle and lower panel of figure 5.10). For particular orientations, only one peak is present (upper panel). For sample B, the situation is comparable in the sense that the FR transients are composed of more than one frequency component and that the components shift upon varying the orientation of the magnetic field within the sample plane.

Exemplary FR transients recorded with $\boldsymbol{B}$ oriented along $[1,-1,0]$ corresponding to $\alpha_1 = 0°$, as well as for $\alpha_2 = 15°$ and $\alpha_3 = 30°$, are depicted in this sequence in the upper, mid and lower panel on the left-hand side of figure 5.11. The respective FFT amplitudes are shown in the panels on the right-hand side. The transients for sample B are recorded under the same conditions as those for

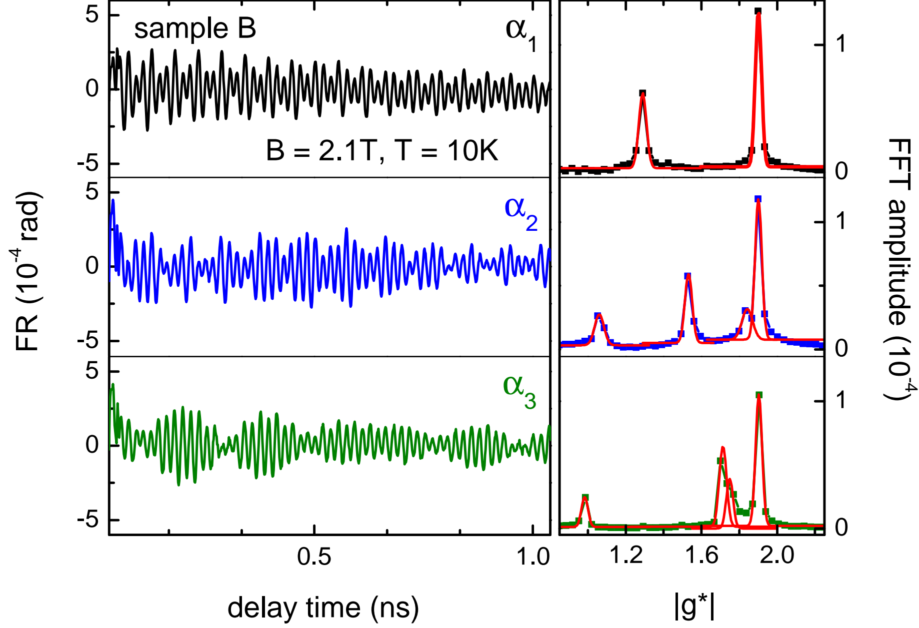

Figure 5.11 *Electron spin signature from sample B for three different orientations of $B = 2.1\,\mathrm{T}$ in the sample plane at $T = 10\,\mathrm{K}$. Left-hand side: FR transients. Right-hand side: Corresponding FFT amplitudes. Solid lines: Gaussian fits.*

sample A1 (that is, specifically, $T = 10\,\mathrm{K}$, $B = 2.1\,\mathrm{T}$). In contrast to the situation for sample A1 with either one or two frequency components, the electron spin signals from sample B displays two to four frequency components. For a detailed understanding of the observed angular dependences, it is instructive to recall the ellipsoidal shape of the surfaces of constant energy in the L-valleys (cf. section 2.1). In accordance with the corresponding Landé tensor, spin precession in the ith L-valley is characterised by [Rot60]

$$(g_i^*)^2 = g_l^2 \cos^2(\theta_i) + g_t^2 \sin^2(\theta_i)\,, \tag{5.1}$$

where θ_i denotes the orientation of $\mathbf{B}$ with respect to the principal axis of the ith ellipsoid of constant energy with $i = 1\ldots4$. g_l and g_t are the independent components of the L-valley Landé tensor. The angles θ_i are related to α by the following geometric considerations. (In the following, the results are listed, the derivation is given in appendix B.) The orientation of the surfaces of constant energy with respect to the sample surface and the magnetic-field orientation is illustrated in figure 5.12 for $\langle 100\rangle$- and for $\langle 111\rangle$-oriented Ge. Obviously, for $\langle 100\rangle$-oriented Ge, the four

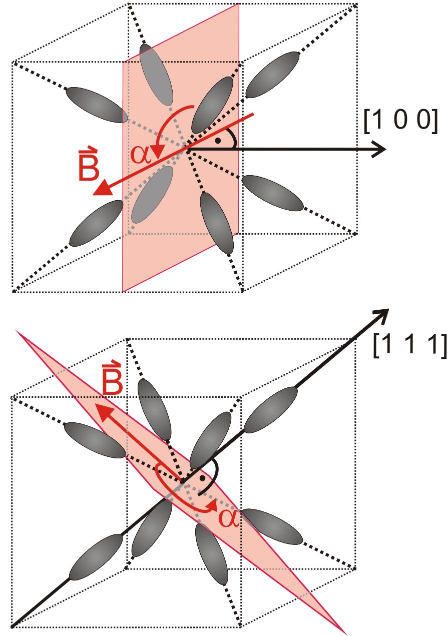

FIGURE 5.12 *Surfaces of constant energy in Ge. The in-plane magnetic-field orientation is indicated for samples A1 and A2, surface normal* $[1,0,0]$ *(upper panel) and for sample B, surface normal* $[1,1,1]$ *(lower panel).*

equivalent conduction band valleys at the L-point result in up to two distinguishable frequency components. These frequency components depend on the angle α included by the magnetic field and directions of high symmetry within the sample surface. The corresponding θ_i in equation (5.1) are

$$\begin{aligned}\cos(\theta_1) &= \frac{2}{\sqrt{6}}\cos(\alpha) \\ \cos(\theta_2) &= -\frac{2}{\sqrt{6}}\sin(\alpha)\end{aligned} \tag{5.2}$$

where $\alpha = 0$ means that the magnetic field is oriented along a $[0,1,1]$-direction in the sample plane. If the surface is oriented normal to $[1,1,1]$, at most four frequency components are expected to contribute to the FR signal:

$$\begin{aligned}\cos(\theta_1) &= 0 \\ \cos(\theta_2) &= \frac{2}{\sqrt{6}}\cos(\alpha) - \frac{2}{3\sqrt{2}}\sin(\alpha) \\ \cos(\theta_3) &= \frac{4}{3\sqrt{2}}\sin(\alpha) \\ \cos(\theta_4) &= \frac{2}{\sqrt{6}}\cos(\alpha) + \frac{2}{3\sqrt{2}}\sin(\alpha)\,.\end{aligned} \tag{5.3}$$

In equation (5.3), α is measured relative to $[1\bar{1}0]$. Figures 5.13 and 5.14 give a comprehensive presentation of the extracted frequency components for samples A1 and B, respectively. The data points from the FR transients shown in figures 5.10 and 5.11 are denoted by the respective angles α_1 to α_3. The data is fitted with equations (5.1), (5.2) and (5.3). Each g_i^* with $i = 1,2$ for sample A1 and $i = 1...4$ for sample B is fitted individually. The hereby deduced independent elements of the $\boldsymbol{g^*}$ tensor are $g_l = 0.81 \pm 0.03$ and $g_t = 1.90 \pm 0.02$ (sample A1), and $g_l = 0.83 \pm 0.01$ and $g_t = 1.90 \pm 0.01$ (sample B). The errors contain a statistical contribution propagated from the individual fits' uncertainties, as well as the systematic uncertainty in the magnetic-field magnitude (cf. section 3.2). A similar analysis is done for sample A2. As is discussed in detail in the next section 5.3.2, the electron spin coherence times are in general shorter in sample A2 than those in samples A1 and B, owing to the higher doping concentration in sample A2. It is nevertheless possible to extract the frequency components for the same angular range as for sample A1. The data is shown in figure 5.15 together with the matching theoretical relationships. Owing to the reduced coherence times in sample A2, the uncertainties of the individual g_i are bigger than those from samples A1 and B. The experimental data is well reproduced by equation (5.1) with $g_l = 0.77 \pm 0.03$ and $g_t = 1.91 \pm 0.02$. Table 5.2 summarises the independent components of the effective g tensor for L-valley electrons for all three samples. The g_l and g_t deduced for the comparatively moderately doped samples A1 and B agree well within uncertainty limits, and similar values are found for the stonger doped sample A2. The tensor elements are close to results of $g_l = 0.828 \pm 0.003$ and $g_t = 1.915 \pm 0.001$ from spin resonance measurements at liquid helium temperature [Hal75, and comparable values reported in references therein]. These measurements address donor-bound electrons, whose wavefunctions are known to be well described in a hydrogen model including energy contributions from the crystal environment (that specifically are the crystal potential $V(\mathbf{r})$ and the spin-orbit interaction $\mathscr{H}_{SO}$, cf. section 2.1). The electrons are in a pure singlet state when bound to typical shallow donors (As, P, Sb) in Ge [Pon66], so that the wavefunction is a linear combination of the four equivalent L-valleys, and the effective g tensor becomes isotropic with the diagonal elements [Rot59]

$$\bar{g} = \frac{1}{3}g_l + \frac{2}{3}g_t. \tag{5.4}$$

sample	g_l	g_t
A1	0.81 ± 0.03	1.90 ± 0.02
B	0.83 ± 0.01	1.90 ± 0.01
A2	0.77 ± 0.03	1.91 ± 0.02

TABLE 5.2 *Components of the L-valley Landé tensor as extracted from FR transients recorded at $T = 10\,\mathrm{K}$ and $B = 2.1\,\mathrm{T}$, except for sample A2 at $\alpha = 45°$ and $135°$, where $B = 0.7\,\mathrm{T}$ is used.*

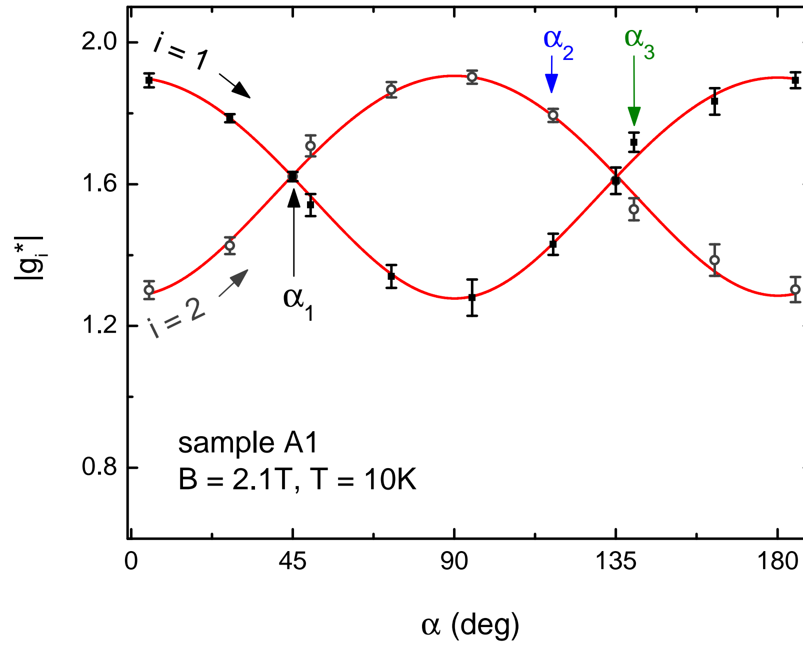

Figure 5.13 *g^* anisotropy for sample A1. g_i^*, $i = 1,2$ are extracted from FR transients in $B = 2.1\,\mathrm{T}$ at $T = 10\,\mathrm{K}$. The solid lines are fits according to equations (5.1) and (5.2).*

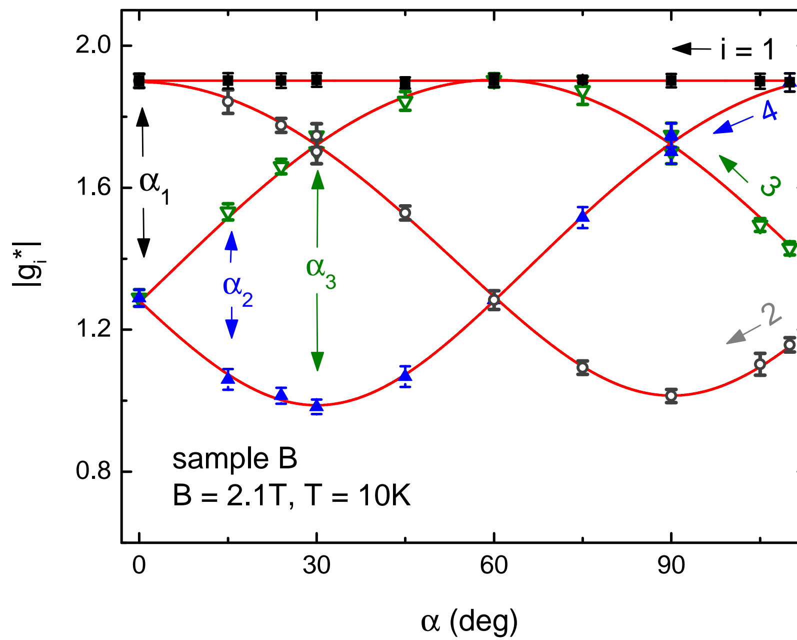

Figure 5.14 *g^* anisotropy for sample B. g_i^*, $i = 1..4$ are extracted from FR transients in $B = 2.1\,\mathrm{T}$ at $T = 10\,\mathrm{K}$. The solid lines are fits to equations (5.1) and (5.3).*

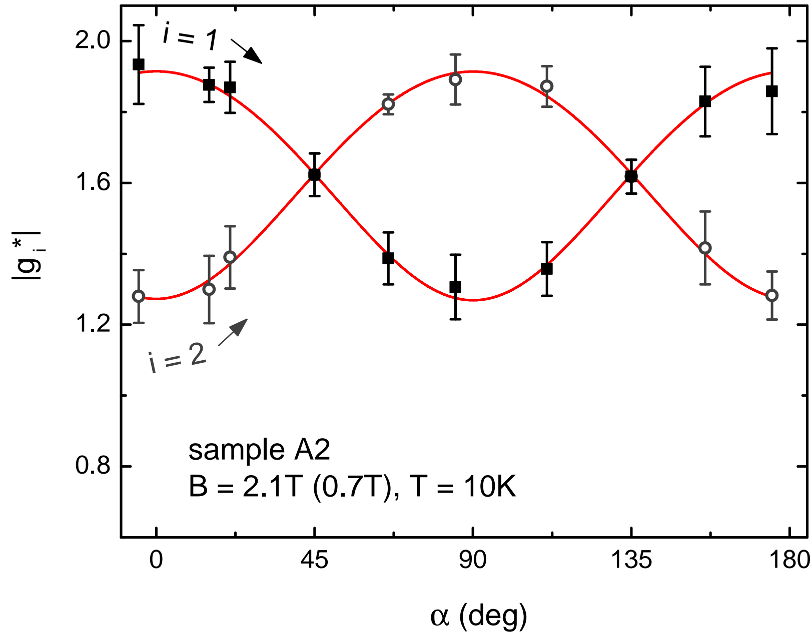

FIGURE 5.15 *g^* anisotropy for sample A2. g_i^*, $i = 1,2$ are extracted from FR transients at $T = 10\,\mathrm{K}$ in $B = 2.1\,\mathrm{T}$ or – for $\alpha = 45°$ and $135°$ – $B = 0.7\,\mathrm{T}$. The solid lines are fits to equations (5.1) and (5.2).*

Thus, a single Larmor frequency is observed, that is independent of the magnetic-field orientation with respect to the crystal main axes [Wil64]. The individual tensor elements can, however, be determined applying strain to the sample, since the application of strain results in repopulation of the L-valleys. Especially under large compressive strain in the [111]-direction, donor-bound electrons predominantly populate one valley [Wil64]. For electrons bound to Sb donors localised in the vicinity of intentionally roughened ⟨110⟩-surfaces, up to four spin resonance peaks stemming from the different L-valleys are observed [Pon66, Hal75]. (According to the referred publications, the efficiency of strain-induced valley repopulation depends on the energy separation between the singlet and triplet donor state. For Sb donors this so-called valley-orbit splitting is small enough – approximately $0.5\,\mathrm{meV}$, which is an order of magnitude less than for As or P donors – that the magnitude of strain induced by surface imperfections is sufficient to locally populate different valleys.) In contrast to spin resonance measurements relying on electrons associated with donors, in the present study, the L-valley Landé tensor is accessed via itinerant electrons due to the following reasons. First, the samples are optical grade wafers. In the spin resonance investigations referred to above, signatures from each single L-valley are explicitly not observed from comparatively smooth surfaces. Second, the excitation conditions – approximately $10^{16}\,\mathrm{cm}^{-3}$ electrons are induced with excess energies of $\sim 100\,\mathrm{meV}$ – are strong compared to the gentle conditions at which spin coherence associated with optically induced donor-bound electrons is observed in direct-gap materials (cf. [Kik98] and section 4.2.2). In particular, n_{opt} is three orders of magni-

tude higher than the donor concentration in samples A1 and B. Third, no indication of electron capture into donor states is seen in the FR transients (as e.g. phase-shifted signal components, cf. section 4.2.2).

5.3.2 Temperature dependences of Landé tensor and spin coherence

The influence of crystal temperature on the decay time of the electron spin signals is investigated for magnetic-field orientations resulting in preferably few frequency components to simplify data analysis. For samples A1 and A2, $\alpha = 45°$ is chosen, resulting in one precession frequency according to the g^* anisotropy depicted in figures 5.13 and 5.15. FR transients from sample A1 in a magnetic field of $B = 0.7\,\mathrm{T}$ are shown in figure 5.16 for various crystal temperatures between 10 K and 200 K. A similar set of FR transients is depicted in figure 5.17 for sample B. The transients for sample B are recorded with $\alpha = 60°$ and hence contain two frequency components (cf. g^* anisotropy for sample B, figure 5.14). Comparable signal amplitudes were achieved using the same pump fluence at all temperatures. Although the central pulse energy is below the direct bandgap over the whole temperature range, at $T = 200\,\mathrm{K}$, 2.4% of the spectral coverage excess the direct bandgap. Thus the density of optically induced carriers at $T = 200\,\mathrm{K}$ is approximately doubled as compared to $T = 10\,\mathrm{K}$. However, since no marked influence on the decay electron spin coherence is observed when varying the excitation density for such an amount at 10 K, the observed decrease in decay time with increasing temperature can be attributed to the variation in crystal temperature. The simulations of Cheng et al. on optical orientation via indirect optical transitions in silicon [Che11] indeed reveal more efficient electron spin orientation at low temperatures. For photon energies in close proximity to the indirect bandgap, they report $P_e = -25\,\%$ at liquid helium temperature and $P_e = -15\,\%$ at room temperature. Assuming that the orientation and the detection process contribute equally to the signal, this translates to a factor of 3 comparing the theoretically expected FR amplitudes at low temperatures and at room temperature. Such a value is in line with the experimentally observed factor of 2 comparing $T = 10\,\mathrm{K}$ and $T = 200\,\mathrm{K}$. However, the achievable polarisation degree additionally depends on the photon energy. Furthermore, the relative efficiency of spin polarisation and detection possibly change with temperature, since the same pulse energies are used over the whole temperature range while the bandgap depends on temperature. The observed decrease in the initial FR amplitude thus presumably can not be attributed solely to the change in crystal temperature, but results from a mixture of various effects. For further analysis, the transients in figures 5.16 and 5.17 are fitted by exponentially decaying cosine functions

$$FR(t) = \sum_i A_i \times \exp\left(-t/\tau\right) \times \cos\left[(\omega_L)_i \times t\right], \tag{5.5}$$

where A_i are the initial amplitudes of the contributing Larmor frequency components $(\omega_L)_i$. The decay time of the electron spin signal is denoted τ. The transients from sample A1 are reproduced with $i = 1$, while those from sample B are fitted well with $i = 1,2$ up to 80 K and $i = 1$ at 150 K,

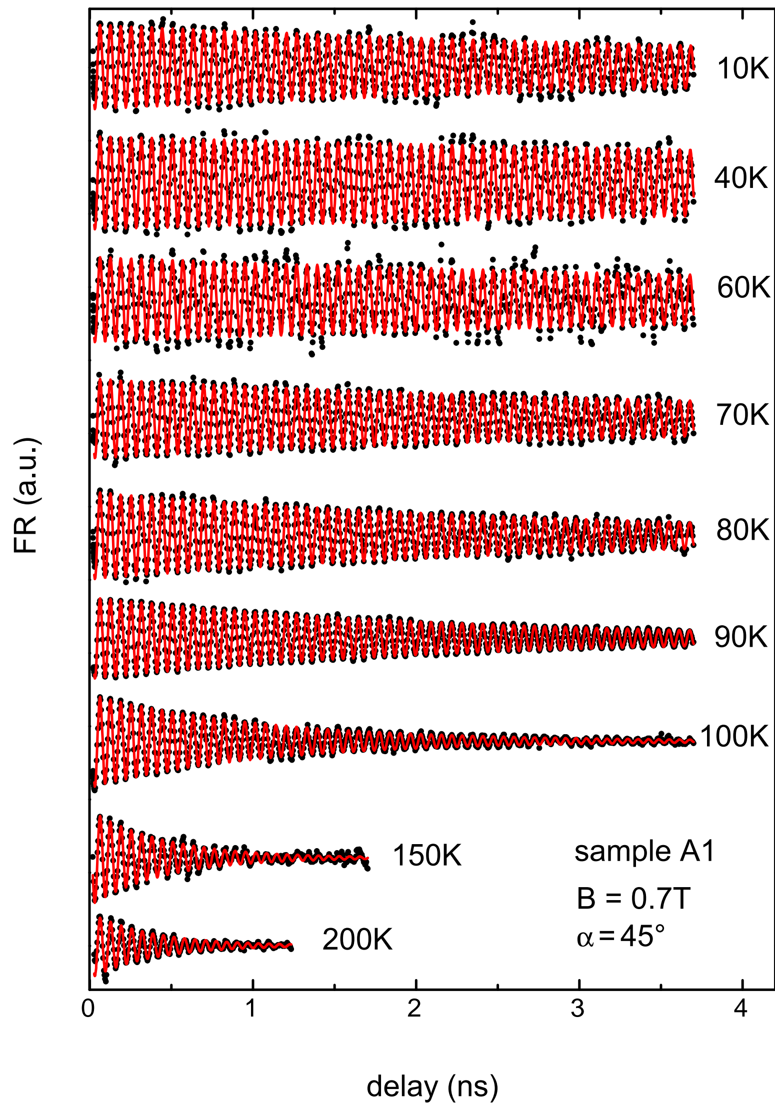

FIGURE 5.16 *FR transients (filled circles) for various temperatures measured from sample A1 in a magnetic field of $B = 0.7\,\mathrm{T}$ with $\alpha = 45°$. The solid lines are fits to the data according to equation (5.5) and $i = 1$.*

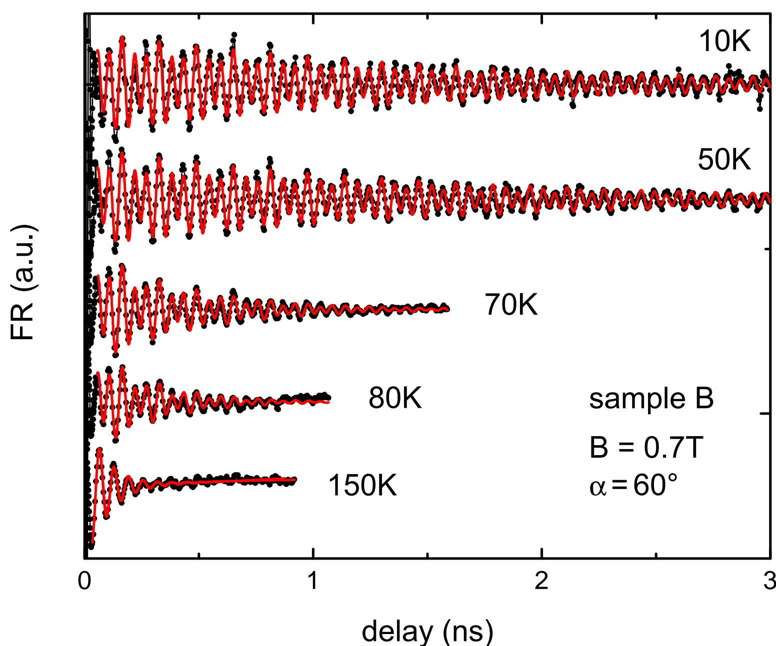

FIGURE 5.17 *FR transients (filled circles) for various temperatures measured from sample B in a magnetic field of $B = 0.7\,\mathrm{T}$ with $\alpha = 60°$. The solid lines are fits to the data according to equation (5.5) and $i = 2$.*

which is the highest temperature investigated for this sample. Note that a universal decay time is assumed for the two frequency components since this is sufficient to achieve good agreement with the data. The respective fits are shown as solid lines together with the FR transients. Additional FR transients from sample A2 for various crystal temperatures with magnetic-field magnitude and orientation with $B = 0.7\,\mathrm{T}$ and $\alpha = 45°$ are analysed in an analogue manner (data not shown). In the following, the extracted effective Landé factors[4] and decay times are discussed subsequently.

Landé tensor Figures 5.18 and 5.19 depict the temperature-dependent $|g_i|$ for sample A1 and sample B, respectively. The error bars in $|g_i|$ for the $\langle 100 \rangle$-oriented sample are (i) the uncertainty resulting from the fitting procedure itself (either indicated by the size of the data points, or coloured according to the data points), and (ii) due to the limited accuracy in α (indicated in grey, $\sim 0.5\,\%$). The effective g factor is practically constant up to $T \leq 100\,\mathrm{K}$. Taking into account the uncertainty in the magnetic-field magnitude, the average value is $|g_1| = |g_2| = 1.61 \pm 0.02$, as is indicated by the solid line. For $T > 100\,\mathrm{K}$, the effective Landé factor decreases, the value found at $T = 200\,\mathrm{K}$ is approximately $98\,\%$ of the constant value at and below $100\,\mathrm{K}$. For sample A2, a similar temperature characteristics is observed with $|g_1| = |g_2| = 1.63 \pm 0.02$ for $T \leq 100\,\mathrm{K}$

[4] In principle, the effective g factors can also be extracted from Fourier analysis as done in section 5.3.1. However, the width of the Fourier peaks is influenced by the decay time of the FR transients and thus such an analysis is inaccurate at elevated temperatures.

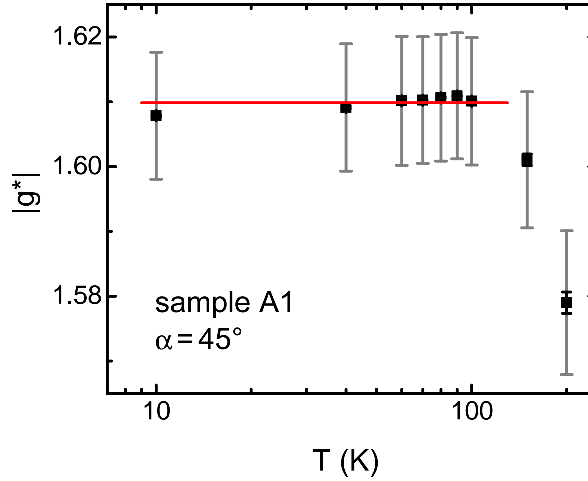

Figure 5.18 *Temperature-dependent effective g factor for sample A1. The respective transients are recorded in $B = 0.7\,\mathrm{T}$ with $\alpha = 45°$ and depicted in figure 5.16. Solid line: constant fit to the data at $T \leq 100\,\mathrm{K}$.*

(data not shown). The somewhat higher value is in agreement with the slightly different tensor elements for samples A1 and A2 (cf. table 5.2). The $|g_i|$ for sample B are depicted in figure 5.19. (Here, the indicated error bars consider both the uncertainties of the fits and the systematic error due to the limited accuracy in α.) As for the $\langle 100 \rangle$-oriented samples, the effective g factors are not markedly changed in the lower temperature range. The average values for $T \leq 80\,\mathrm{K}$ are $|g_1| = |g_2| = 1.89 \pm 0.02$ and $|g_3| = |g_4| = 1.26 \pm 0.02$. The transient at 150 K is fitted well with only one precession frequency corresponding to $g \sim 1.61$. This value is similar to those found in samples A1 and A2. Note that, although the decay time of the signal is reduced to such extent that a beating would hardly be resolved (cf. corresponding transient in figure 5.17), neither of the g_i found at lower temperatures provide an equally good fit to the data. To interpret the observations, it is interesting to compare them to the temperature dependence of the tensor elements predicted by the three band $\boldsymbol{k} \cdot \boldsymbol{p}$-approximation, cf. equations (2.10). In this approximation, g_l and g_t depend on the energy difference of valence and conduction band at the L-point E_L^{cv}, the split-off energy and the L-valley longitudinal and transversal effective masses. In the following estimation, the temperature dependence of E_L^{cv} is assumed to be similar to that of the indirect bandgap. The latter is taken according to [Iof]. The split-off energy is expected to be independent of temperature (cf. section 2.1). The temperature dependence of the effective masses is also assumed to follow that of the indirect bandgap. This is reasonable taking into account corresponding observations in silicon [Gre90]. With these parameters, the temperature-induced change in the effective g factor for samples A1 and A2 with $\alpha = 45°$ is less than 0.1 % up to $T = 50\,\mathrm{K}$. At $T = 150\,\mathrm{K}$, $g_1 = g_2$ is 0.6 % smaller, and at $T = 200\,\mathrm{K}$, $g_1 = g_2$ is 1 % smaller – always compared to the low temperature value. For sample B and $\alpha = 60°$, the theoretical estimate yields temperature-induced changes below 0.1 % in $g_1 = g_2$ as long as the temperature is below 150 K, and in $g_3 = g_4$ for $T \leq 30\,\mathrm{K}$.

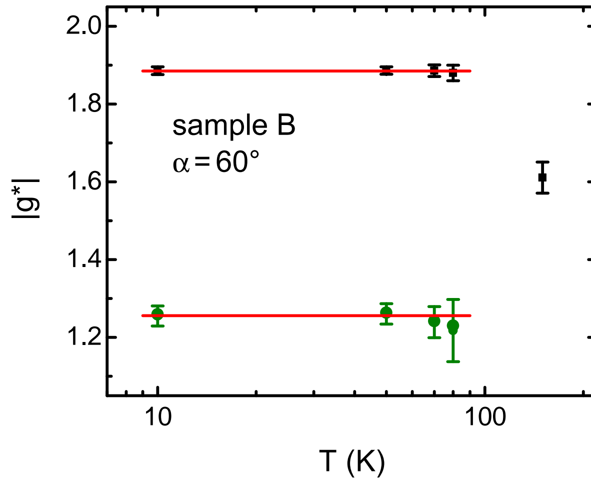

FIGURE 5.19 *Effective g factors extracted from FR transient from sample B at various crystal temperatures. The transients are recorded in $B = 0.7\,\mathrm{T}$ with $\alpha = 60^\circ$ (cf. figure 5.17). Solid line: constant fit to the data at $T \leq 100\,\mathrm{K}$.*

At $T = 150\,\mathrm{K}$, $g_3 = g_4$ is $\sim 98\,\%$ of the low temperature value. The $\boldsymbol{k}\cdot\boldsymbol{p}$-approximation as a result is in line with the trend for the $g_i(T)$ dependence observed in experiment (except the fact that only one frequency component is found in sample B at $T = 150\,\mathrm{K}$). This finding contrasts the results on g^* as a function of temperature in $In_{0.53}Ga_{0.47}As$ (cf. section 4.2.1) and literature results in, e.g., GaAs. In these direct-gap semiconductors, the temperature dependence estimated from $\boldsymbol{k}\cdot\boldsymbol{p}$-theory contradicts the experimentally determined characteristics, and the filling of Landau levels has to be included in an adequate theoretical description [Zaw08]. However, whether the temperature dependence of g^* is sufficiently described by the temperature characteristics of corresponding band parameters is not correlated to the indirect or direct nature of the bandgap. The important point is rather the deviation of the effective Landé factor from the free electron value of $g \sim 2$. As an example, the effective g factor of Γ-valley electrons in the direct-gap material InP is found to vary from $g^* = 1.20$ at $T = 5\,\mathrm{K}$ to $g^* = 1.25$ at $T = 200\,\mathrm{K}$ in accordance with $\boldsymbol{k}\cdot\boldsymbol{p}$-theory. A possible explanation why the FR transient recorded in sample B at $T = 150\,\mathrm{K}$ contains only one frequency component lies in the mechanisms that are responsible for electron spin decoherence. As is laid out in the following sections, electron scattering between two L-valleys leads to dephasing of the spin state of the scattered electron, if the involved valleys are characterised by different g_i. The time scale for intervalley scattering equals the one associated with dephasing due to different g_i at $T = 150\,\mathrm{K}$ ($\tau_L \sim \tau_{phon}(150\,\mathrm{K}) \sim 40\,\mathrm{ps}$ in the notation of section 5.3.3.), while for lower temperatures, the former exceeds the latter. It is therefore possible, that the isotropic effective g factor (5.4) – that explicitly is $\bar{g} = 1.54$ with the present results for g_t and g_l (cf. table 5.2) – is in fact approximated in all samples for $T \geq 150\,\mathrm{K}$.

Decay time Figure 5.20 depicts the decay times of the electron spin signals as a function of the crystal temperature for samples A1 as black squares, A2 as red circles and B as blue triangles. Overall, τ varies from $\sim 100\,\mathrm{ps}$ up to $\sim 10\,\mathrm{ns}$. The longest decay times seen for sample A1 at low temperatures provide a lower limit rather than an exact measure. This is due to the limited delay line of 3.7 ns. In addition, the rate equation model detailed in the following section 5.3.3 points to a strong reduction of the apparent τ by minute misalignments of α. Comparing the temperature dependences for the different samples in a qualitative manner first, four major characteristics become apparent. (i) For all samples, the decay time does not decrease with increasing temperature below $T \sim 60\,\mathrm{K}$. (ii) Comparing the $\langle 100 \rangle$-oriented samples A1 and A2 at low temperatures, the electron spin signal decays faster in the more strongly doped sample: $\tau(A2) \sim 1\,\mathrm{ns}$ as compared to $\tau(A1) > 5\,\mathrm{ns}$. (iii) At elevated temperatures ($T > 60\,\mathrm{K}$), the signals decay faster with increasing temperature and the influence of doping concentration vanishes as follows from the similar decay times for samples A1 and A2. (iv) The decay times for sample B are shorter than those for the comparably doped sample A1 over the whole temperature range. The first three findings are consistent with spin relaxation via the EY mechanism, that is spin relaxation due to spin flips mediated via momentum scattering (cf. section 2.3). As already mentioned, this mechanism is expected to be relevant for conduction band electron spins in Ge, particularly with regard to the lack of DP dephasing in the diamond lattice. A spin flip can in principle occur with intra- as well as with intervalley scattering. However, momentum relaxation in a multi-valley conduction band is dominated by intervalley processes [Yu10]. The unpronounced temperature dependence below $T = 60\,\mathrm{K}$ indicates that impurity scattering dominates momentum relaxation, while the decrease of τ beyond $T = 60\,\mathrm{K}$ is in line with phonon-mediated spin relaxation. The fourth aspect can be understood considering scattering events from a valley with an initial effective g factor g_i to a final state characterised by a different g_f. As is evident from the g^* anisotropy in sample B (cf. figure 5.14), such processes are expected to occur in sample B for any α, and after a scattering event with $g = |g_f - g_i| \neq 0$, the spin state of the electron dephases relative to the spins in both the initial as well as the final valley. In contrast, in sample A1 and A2 with the present orientation of the magnetic field, all valleys are characterised by the same effective g factor, and thus no dephasing is induced by intervalley scattering. The decay times of the electron spin signal at elevated temperatures are therefore longer in samples A1 and A2 as compared to sample B. The impact of scattering with $\Delta g \neq 0$ is consequently also expected in the $\langle 100 \rangle$-oriented samples away from $\alpha = 45^\circ$ as is obvious from the g^* anisotropy for the $\langle 100 \rangle$-oriented samples (cf. figures 5.13 and 5.15). Respective data is discussed in section 5.3.5 below. Before a quantitative analysis of the above findings is conducted in the following sections, it is instructive to classify the present electron spin decay times by a comparison to literature results. In particular, the decay time found in sample A2 at low temperatures as well as the decrease of τ at elevated temperatures is in good agreement with recent results from non-local Hanle measurements in n-type bulk Ge of comparable doping concentration [Zho11]. Also recently, Guite and Venkataraman extracted a comparatively long spin lifetime of $4.6 \pm 1\,\mathrm{ns}$ at $T = 127\,\mathrm{K}$ in Ge with $n_d \sim 5 \times 10^{17}\,\mathrm{cm}^{-3}$ Sb sites [Gui11]. Similar val-

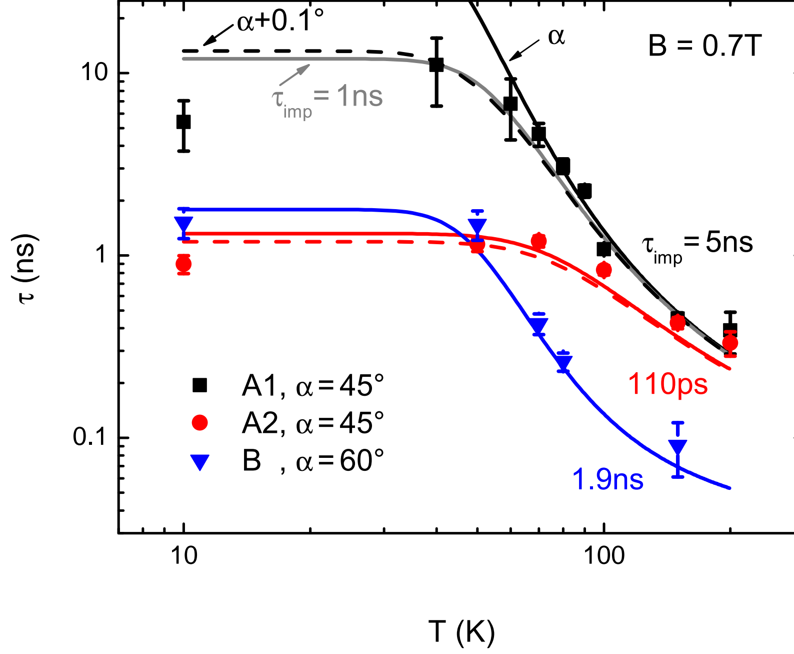

FIGURE 5.20 *Temperature-dependent decay time for samples A1 (black squares), A2 (red circles) and B (blue triangles). The data points are from FR transients in* $B = 0.7\,\text{T}$. *The colour-coded lines are model calculations according to equation (5.7).*

ues can be extracted from electron spin resonance linewidths at $T = 10\,\text{K}$ in more heavily doped material ($n_d \sim 10^{18}\,\text{cm}^{-3}$) [Cha75, Ger70]. Note that these literature values as well as the decay times found in the present experiment actually correspond to T_2^* and are much shorter than the T_1 times extracted from saturating the Zeeman transitions by increasing the microwave power in electron spin resonance measurements. At liquid helium temperature T_1 times as long as $0.1\,\text{ms}$ are reported for isotopically enriched As-doped Ge with $n_d = 2 \times 10^{15}\,\text{cm}^{-3}$ [Wil64]. In natural As-doped Ge, Ghershenzon et al. found T_1 times between $20\,\mu\text{s}$ for $n_d = 3 \times 10^{15}\,\text{cm}^{-3}$ and $1\,\mu\text{s}$ for $n_d \sim 5 \times 10^{16}\,\text{cm}^{-3}$ [Ger70]. In contrast to the coherence times observed in the present investigation, T_1 strongly depends on temperature. As mentioned in the introduction of the present chapter, $T_1 = 10^{-3}\,\text{s}$ is reported for $T = 1.3\,\text{K}$ [Wil64].

5.3.3 A rate equation model for the decay of spin decoherence

The above qualitative analysis of the temperature-dependent decay of electron spin coherence in samples A1, A2 and B indicates that a theoretical modelling of electron spin decoherence has to include impurity- as well as phonon-mediated intervalley scattering with either $\Delta g = 0$ or $\Delta g \neq 0$. The schematic illustration in figure 5.21 applies to samples A1 and A2 as well as to sample B for $\alpha = 60^\circ$ or integer multiples. In these cases, each of the four L-valleys can be attributed to one of two geometrical classes that are characterised by two different effective g factors (in samples A1

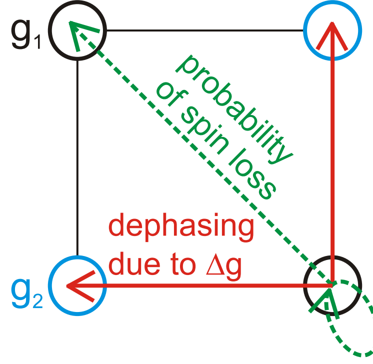

FIGURE 5.21 *Schematic illustration of electron spin decoherence. Scattering between valleys with $g_1 - g_2 = 0$ with a certain probability results in a spin flip according to the EY mechanism. For $g_1 - g_2 \neq 0$, the scattered spin state loses phase coherence with both the spins in the initial and the final valley.*

and A2 $g_1 = g_2$ for $\alpha = 45°$). Scattering from an arbitrary initial valley – the lower right one in the illustration – with the same probability results in a final state characterised by $g_f = g_i$ or $g_f \neq g_i$. This implies, that the probability for scattering within the initial valley is the same as for scattering into one of the other valleys. The scattering processes are furthermore assumed to be independent, so that the overall scattering rate is the sum over the rates for the contributing scattering processes. Scattering processes into equivalent valleys ($\Delta g = 0$) are modelled by an intervalley scattering time of τ_{inter} and a probability c_{loss}^{-1} of a spin flip per scattering event. As a result, the decoherence rate for such processes is

$$\tau_{loss} = c_{loss} \times \tau_{inter}/2,$$

where the factor of 2 accounts for the negative contribution of a flipped spin to the FR signal. For scattering with $\Delta g \neq 0$, a particular spin acquires a phase difference of $\pi/2$ relative to the remaining ensemble within

$$\tau_L = \frac{\pi/2}{(\Delta g \mu_B B)/\hbar} \tag{5.6}$$

after the scattering event. Consequently, an estimate for the related decoherence time is

$$\tau_{decoh} = \tau_{inter} + \tau_L.$$

Note that this model for decoherence requires both a scattering process and some time of precession with an altered effective g factor so that decoherence is characterised by the slower of the two time constants. Taken together, the electron spin signal decays within

$$\tau^{-1} = \tau_{decoh}^{-1} + \tau_{loss}^{-1}. \tag{5.7}$$

The above model neglects carrier recombination. This is a good approximation since the corresponding time scale is of the order of $1\,\mu$s [Cho77] and thus exceeds the longest τ detected in the

present study by two orders of magnitude. The temperature dependence of τ is determined by the temperature dependence of intervalley scattering. The latter is modelled as being composed of impurity- and phonon-mediated processes according to

$$\tau_{inter}^{-1} = \tau_{imp}^{-1} + \tau_{phon}^{-1}.$$

τ_{imp} is assumed to be independent of temperature. In contrast, according to Weinreich et al. [Wei59], the temperature dependence of the phonon contribution is

$$\tau_{phon} = \frac{1}{2w_2} \exp\left(\frac{\Theta}{T}\right)$$

with $w_2 = 10^{11\pm0.3}\,\mathrm{s}^{-1}$ and $\theta = 315\,\mathrm{K} \pm 10\%$ as extracted in the referred publication from experimental data for As-doped Ge. Table 5.3 summarises the values for τ_{imp} and c_{loss} needed to well reproduce the temperature characteristics of τ for samples A1, A2 and B in figure 5.20, together with the possible ranges. (For the model curves in figure 5.20, $c_{loss} = 24.5$ is used.) To begin with c_{loss}, the extracted values correspond to a probability $c_{loss}^{-1} = (4-7)\ \%$ for a spin flip per intervalley scattering event. This value is three orders of magnitude larger than previous findings for spin decoherence mediated by core-potential – or intervalley – Elliott scattering in degenerately doped material [Cha75]. The deviation might originate from additional decoherence channels inherent to the optically induced electron population in the present experimental configuration, such as electron-electron or electron-hole scattering. In addition, spin precession in an external magnetic field results in loss of phase coherence if the effective g factor depends on the carrier momentum, as is reported for electron spins in III-V materials [Bro04, and references therein]. The relevance of this mechanism depends on the carrier energy spread, as well as on the relation between carrier energy and g^* and possibly dephases the spin ensemble within one valley. A considerable contribution of this mechanism to the overall decay of the electron spin signal would lead to an overestimation of c_{loss} in the present rate equation model. For the extraction of τ_{imp}, one has to consider that minor misalignments of $\boldsymbol{B}$ markedly reduce τ especially for samples A1 and A2 in the vicinity of $\alpha = 45°$ and $\alpha = 135°$ where τ_L diverges, cf. equation (5.6). Model traces for perfect alignment are depicted as solid lines in figure 5.20. For sample A1, the trace with $\tau_{imp} = 1\,\mathrm{ns}$ matches the data over the entire temperature range. In contrast, the curve with $\tau_{imp} = 5\,\mathrm{ns}$ agrees

sample	A1	A2	B
τ_{imp}	$(5\pm3)\,\mathrm{ns}$	$(110\pm50)\,\mathrm{ps}$	$(1.9\pm0.7)\,\mathrm{ns}$
c_{loss}	$14-27$		

TABLE 5.3 *Intervalley scattering times τ_{imp} for impurity mediated processes. c_{loss}^{-1} is the probability of spin loss per intervalley scattering event. The parameters are deduced from best fits of model (5.7) to the data in figure 5.20.*

well only at elevated temperatures but predicts $\tau \sim 60\,\mathrm{ns}$ as the low temperature limit. However, a curve with $\tau_{imp} = 5\,\mathrm{ns}$ and $\Delta\alpha = 0.1^\circ$ (dashed lines) agrees well with the experimental findings for $\tau(T)$. Such a misalignment of α is reasonable due to the following reasons. While $\Delta\alpha > 0.2^\circ$ can be excluded because it alters the temperature dependence markedly in the high temperature range especially for sample A1, perfect orientation is also not very likely: α was fine-aligned in the vicinity of 45° for samples A1 and A2 by maximising τ, but the typical deviation from the crystallographic surface orientation for the samples is $\sim 0.1^\circ$ according to the manufacturer. In addition, possible tilts of the $\langle 100\rangle$ surface with respect to the plane of magnetic-field orientation can not be adjusted in all directions within the cryostat. The experimentally extracted decay times for sample B are fitted best with $\tau_{imp} \sim 2\,\mathrm{ns}$ which is somewhat shorter than the value found for sample A1. Since in sample B for every α valleys of different effective g factor are present, an impact of the magnetic-field orientation on the electron spin decay time is not expected according to the present model and only the model trace for perfect alignment of $\boldsymbol{B}$ is shown in figure 5.20. For the more strongly doped sample A2, a much shorter value of $\tau_{imp} \sim 110\,\mathrm{ps}$ is found and hence the impact of $\Delta\alpha = 0.1$ is less pronounced than in sample A1. The extracted timescales for impurity-mediated intervalley scattering are in line with predictions of $\sim 6\,\mathrm{ns}$ for $n_d = 10^{14}\,\mathrm{cm}^{-3}$ and $\sim 50\,\mathrm{ps}$ for $n_d = 5\times 10^{16}\,\mathrm{cm}^{-3}$ in Sb-doped Ge at $T = 40\,\mathrm{K}$ [Mas64]. The electron spin decay times in all three samples appear to increase with increasing temperature below $T \sim 60\,\mathrm{K}$ which may be attributed to the temperature dependence of τ_{imp}. The latter is not included in the present model, however, a drop of τ_{imp} upon lowering T in the respective temperature range is consistent with literature results [Wei59].

5.3.4 Magnetic field dependence of the decay time

The influence of the magnetic-field magnitude on the decay time of electron spin coherence is very interesting. In particular, the rate equation model (5.7) introduced in the previous section suggests that the electron spin decay time is independent of the magnetic-field magnitude in the $\langle 100\rangle$-oriented samples with $\alpha = 45^\circ$, where τ_L diverges according to equation (5.6). Thus, any magnetic field dependence points towards additional mechanisms of spin decoherence, such as dephasing within one valley due to a momentum-dependent effective g factor. In all other cases, τ is expected to decrease with increasing magnetic-field magnitude. Respective data in sample B with $\alpha = 60^\circ$ is shown in figure 5.22 together with the prediction according to model (5.7) with the parameters extracted from the temperature characteristics of τ (cf. table 5.3). The model calculation depicted as a solid line reproduces the experimental trend. In particular, the decay time at $B = 4.2\,\mathrm{T}$ is expected to be $20\,\%$ less than at $B = 0.05\,\mathrm{T}$ compared to $\sim 25\,\%$ as observed experimentally. However, the agreement should not be overrated keeping in mind the relatively large error bars. In sample A1 with $\alpha = 0^\circ$, where the valleys are also characterised by two different effective g factors (cf. g^* anisotropy in figure 5.13), the τ extracted from FR transients recorded at $B = 0.1\,\mathrm{T}$ to $B = 0.7\,\mathrm{T}$ varies between $0.8\,\mathrm{ns}$ and $1\,\mathrm{ns}$. A trend towards shorter decay

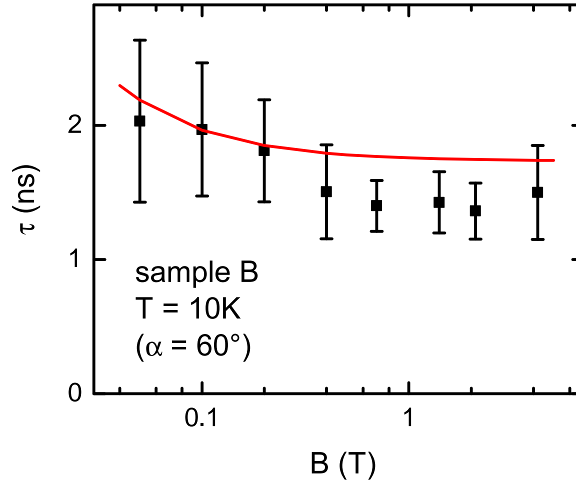

FIGURE 5.22 *Magnetic-field dependent electron spin decay times extracted from FR transients in sample B at $T = 10\,\mathrm{K}$ and with $\alpha = 60°$. The solid line is calculated from rate equation model (5.7) with the parameters given in table 5.3.*

times with increasing B as suggested by model (5.7) can not be read from the experimental data (the decay time at $B = 0.7\,\mathrm{T}$ should be 17 % less than at $B = 0.1\,\mathrm{T}$). As a result, due to the experimental uncertainty, the decrease of τ with increasing magnetic-field magnitude suggested by the rate equation model in configurations with finite τ_L can not be deduced without doubt from the experimental data. Turning the focus to configurations with infinite τ_L, indeed, the decay time in sample A2 is observed to increase with decreasing magnetic-field magnitude. Specifically, the decay time is observed to increase from approximately 1 ns at $B = 0.7\,\mathrm{T}$ up to 4 ns at $B = 0.05\,\mathrm{T}$. Such a trend strongly supports that the additional dephasing mechanism mentioned above indeed contributes to spin relaxation. The observed dependence of τ on the magnetic-field magnitude is as expected for dephasing due to a momentum-dependent effective g factor: the higher the precession frequency, the faster the dephasing of the spin states. As described in the previous section 5.3.3, the existence of such dephasing mechanism can partly explain the relatively high probability for a spin-flip per momentum scattering event deduced from the present data there and in the following section 5.3.5. (In contrast, in sample A1 a constant decay time of $\tau \sim 5\,\mathrm{ns}$ is observed varying the magnetic-field magnitude in the same range. However, this is presumably attributed to the limited delay time of 3.7 ns.)

5.3.5 Crystallographic anisotropy of the decay time

As mentioned in section 5.3.3, the rate equation model (5.7) predicts a dependence of the decay of electron spin coherence on the orientation of the magnetic field within the sample plane for the $\langle 100 \rangle$-oriented samples. In figure 5.23, the electron spin decay times for various orientations of the magnetic field in the sample plane are shown for sample A2. The corresponding FR transients are

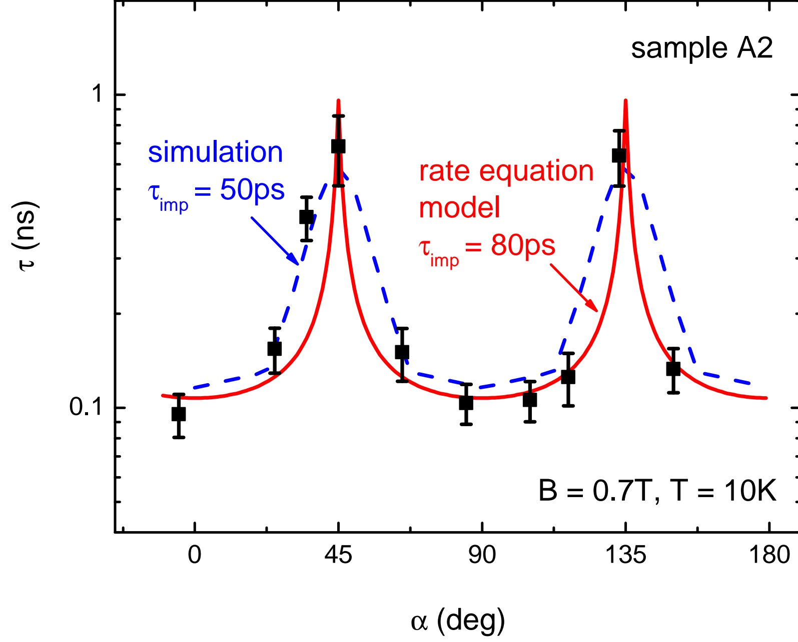

FIGURE 5.23 *Influence of magnetic field orientation on the decay time for sample A2. Squares: decay times extracted from FR transients in $B = 0.7\,\mathrm{T}$ at $T = 10\,\mathrm{K}$. Solid line: model calculation according to equation (5.7). The dashed line is extracted from numerically simulated FR transients (details in the main text).*

recorded at $T = 10\,\mathrm{K}$ and in $B = 0.7\,\mathrm{T}$. The data reveal a marked reduction of the coherence time τ for configurations of different g_1 and g_2 (cf. g^* anisotropy in figure 5.13). In particular, the longest coherence is found for $\alpha = 45°$ and $\alpha = 135°$, where only one frequency component contributes to the signal and, consequently, intervalley scattering can not change the effective g factor. As stated above, such a behaviour is in line with the rate equation model, since τ_L – and thus τ_{decoh} – is determined by Δg which in turn depends on the orientation of the magnetic field. A corresponding model calculation is included as a solid line. The angular dependence of τ is matched with $c_{loss} = 24.5$ – as $\tau(T)$ above – and $\tau_{imp} = 80\,\mathrm{ps}$. In accordance with the low temperature characteristics of intervalley scattering (cf. section 5.3.3), this value is slightly lower than the $\tau_{imp} = 110\,\mathrm{ps}$ extracted in the referred sections from $\tau(T)$ (cf. table 5.3). The dashed line represents the result of a numerical simulation based on the same physical mechanisms that are included in the rate equation model (5.7). The time evolution of an ensemble of 10,000 spin states – this number is large enough to suppress non-physical size effects – is calculated as follows. The simulation starts at $t = 0$ with four equally occupied valleys, two of which are characterised by g_1 and the remaining two by g_2. For each time step Δt, each spin state is scattered into its initial or one of the other valleys with the probability $p_{iv} = 1 - \exp(-\Delta t/\tau_{iv})$. During such a scattering event, the probability of a spin flip is $p_{flip} = 1 - \exp(-\Delta t/(c_{loss} \times \tau_{iv}))$. In addition, during each time step, the phase of each spin state evolves in the external magnetic field according to the currently corresponding

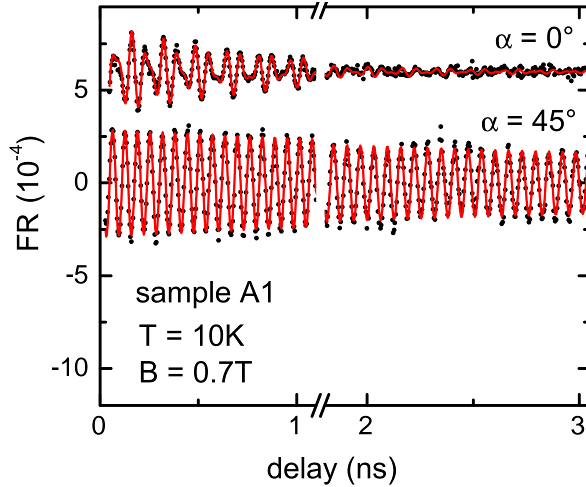

FIGURE 5.24 *Influence of the magnetic-field orientation on the decay time for sample A1. The transient are recorded at $T = 10\,\mathrm{K}$ and $B = 0.7\,\mathrm{T}$ with $\alpha = 0°$ and $\alpha = 45°$. The solid lines are fits according to equation (5.5).*

effective g factor. Integrating over all spin states reveals the projection of the spin polarisation onto the initial polarisation direction and thus a simulated FR transient. The decay times are – as for the experimental transients – extracted by fitting the transients with exponentially damped cosine functions according to equation (5.5) with two contributing frequency components. The experimental data is rather well approximated choosing $c_{loss} = 24.5$ – the same value is used for the rate equation model curve – and a lower impurity scattering time of 50 ps. More interestingly, the simulation indicates less sharp peaks in τ when α approximates 45° or 135°. In contrast to the rate equation model, scattering with $\Delta g = 0$ and $\Delta g \neq 0$ are not treated independently in the numerical simulation. An electron spin state can be scattered back to a valley with $g_{f2} = g_i$ after a scattering event with $g_{f1} \neq g_i$. As a result, decoherence due to scattering with $\Delta g \neq 0$ is motionally narrowed. The fact that both the rate equation model as well as the simulation reproduce the main feature of the angle dependence of τ – namely the peaks at 45° or 135° – further justifies the present picture of electron spin decay. The characteristic angle dependence of τ is also found in sample A1, as is seen from the FR transients in figure 5.24. The transients are recorded at $T = 10\,\mathrm{K}$ in $B = 0.7\,\mathrm{T}$ and are shown together with exponentially decaying cosine fits according to equation (5.5) with $i = 1$ for $\alpha = 45°$ and $i = 2$ for $\alpha = 0°$. Due to the limited delay line of 3.7 ns, the data only allow to infer a lower limit for the ratio of maximal and minimal decay time for this sample, which is a factor of 5. The rate equation model predicts a factor of 12 while the analysis of the simulated FR transients results in a factor of 6. In contrast, the decay time in the $\langle 111 \rangle$-oriented sample B does not significantly depend on the magnetic-field orientation (data not shown). This finding is again in line with the present theory of electron spin decay, as is shown by the following estimation. As a first approximation, dephasing is dominated by the maximum Δg at each α. Hence, the biggest difference is expected comparing (i) $\alpha = (2n) \times 30°$ to (ii)

$\alpha = (2n+1) \times 30°$ with $n \in \mathbb{N}_0$ (cf. g^* anisotropy in figure 5.14). In case (i), $\Delta g = 0.6$ while in case (ii), $\Delta g = 1$. According to the rate equation model (5.7) the difference in the corresponding decay times is $\sim 1\,\%$.

5.4 Summary

The presented time-resolved magneto-optical investigations demonstrate optical orientation and readout of both electron and hole spins in the indirect-gap semiconductor Ge. The most important results on spin-dependent optical response, orientation efficiency and carrier spin dynamics are the following:

Due to the energetic proximity of Γ- and L-valleys, electron and hole spin dynamics are accessible via indirect optical transitions. However, the mechanism of spin-dependent optical response revealing electron spin dynamics is two orders of magnitude weaker than that revealing hole spin dynamics. Excitation predominantly across the indirect bandgap with an excess energy of approximately 0.1 eV results in an electron spin polarisation of 1 %, as is evident from a comparison of the magneto-optical response per photogenerated electron in Ge and III-V semiconductors. The degree of electron spin polarisation does not substantially differ for (i) excitation predominantly across the indirect bandgap with the present excess energy and (ii) excitation across the direct bandgap with excess energies of approximately 0.2 eV and 0.7 eV (again with respect to the indirect bandgap). In particular, such a degree of electron spin polarisation is considerably lower than the value of 50 % that is achieved in typical direct-gap semiconductors as long as the excess energies are beyond the split-off energy. The order of magnitude of the polarisation degree is in accordance with a recent theoretical investigation on optical orientation via phonon-assisted transitions in silicon.

Furthermore, for the first time, long-lived hole spin dynamics is observed in a bulk semiconductor. The absolute value of the hole effective g factor is 5.7 ± 0.2, which is close to a previous spin resonance result for light holes. Hole spin coherence is preserved for 100 ps at low excitation densities and temperatures of approximately 10 K in agreement with recent theoretical results. Elevated excitation conditions and temperatures strongly reduce the hole spin coherence time.

In addition, time-resolved magneto-optical spectroscopy provides direct access to the L-valley Landé tensor via optically induced (itinerant) electrons. The independent tensor elements are $g_t = 1.9$ and $g_l = 0.8$, in agreement with previous spin resonance results for donor-bound electrons. The comprehensive analysis of electron spin dynamics additionally reveals remarkably robust coherence of optically oriented electron spins. It specifically is lost within ~ 100 ps to ~ 10 ns depending on temperature, doping concentration and orientation of the external magnetic field with respect to the L-valley ellipsoids of constant energy. The characteristics of the electron spin decay time are explained in a rate equation model that takes into account a spin flip probability of $(4-7)$ % associated with intervalley scattering, as well as decoherence due to scattering between valleys of different effective Landé factor.

6 Comparative summary and outlook

The present work provides a comparative magneto-optical pump-probe analysis of carrier spin dynamics in direct- and indirect-gap bulk semiconductors. It is well-known that electron spin dynamics in direct-gap materials is accessible via optical transitions at the fundamental bandgap. In the present work, GaSb and $In_{0.53}Ga_{0.47}As$ are investigated, for the first time detecting electron spin dynamics in the telecom wavelength band around 1.55 μm. Although the measurement technique has not been applied to these materials before, it was used to study electron spin dynamics in many other direct-gap semiconductors, specifically in the prototypical material GaAs. The present results confirm the current understanding of electron spin dynamics in direct-gap semiconductors. In particular, the impact of spin-orbit coupling on electron spin relaxation becomes evident when comparing room temperature spin relaxation times of 4 ps in GaSb and 30 ps in $In_{0.53}Ga_{0.47}As$ (in comparatively weakly n-doped samples and in absence of an external magnetic field). Thus, in accordance with the dominant (D'yakonov-Perel') relaxation mechanism, stronger spin-orbit coupling shortens the electron spin relaxation time. The present magneto-optical pump-probe measurements in Ge demonstrate carrier spin orientation and readout via indirect optical transitions, and, for the first time, provide a comprehensive analysis of coherent precession of optically induced electron and hole spins in an indirect-gap or group-IV semiconductor. Comparing typical direct-gap semiconductors and Ge, the following differences are noted with regard to orientation and readout of carrier spins, as well as the dynamics of optically induced hole and electron spins.

The efficiency of electron spin orientation in the fundamental conduction band minima (L-valleys) of Ge is considerably smaller than in the fundamental conduction band minimum (Γ-valley) of direct-gap semiconductors at comparable excess energies (that specifically exceed the fundamental bandgap by less than the split-off energy). The electron spin polarisation is $2-3$ orders of magnitude smaller in agreement with recent theoretical investigations on optical orientation via phonon-assisted transitions in silicon [Che11].

In contrast to direct-gap semiconductors, in Ge, hole spins are accessible via interband transitions, as was recently shown for direct optical transitions [Lor09, Lor11]. The present analysis evidences that hole spin dynamics is also accessed via indirect optical transitions due to the energetic proximity of direct- and indirect conduction band minima in Ge. Furthermore, a detailed investigation of hole spin dynamics reveals hole spin coherence times as long as 100 ps at low temperatures and gentle excitation conditions. This value is in agreement with previous theoretical results [Dar05] and, in particular, exceeds theoretically predicted low-temperature hole spin relaxation times in direct-gap semiconductors by two orders of magnitude [Yu05, She10].

The multivalley structure of the fundamental conduction band of Ge is apparent in the coherent Larmor precession of optically induced electron spins. In direct-gap semiconductors one precession frequency is observed, being furthermore independent of the orientation of the in-plane magnetic field. In contrast, the reduced symmetry of the Landé tensor in the L-valleys of Ge results in up to four precession frequencies that depend on the orientation of the magnetic field with respect to the main axes of the crystal. The Landé tensor elements for photogenerated L-valley electrons are in agreement with previous spin resonance results for donor-bound electrons [Rot60, Hal75]. In contrast to electron spin relaxation in direct-gap semiconductors that is driven by the D'yakonov-Perel' mechanism, optically induced electron spins in the L-valleys of Ge loose coherence and/or are relaxed via scattering between valleys of different effective Landé factor and/or Elliott-Yafet-type spin-flip intervalley scattering.

Outlook The possibility to detect carrier spin dynamics via indirect optical transitions opens up interesting possibilities for future magneto-optical pump-probe investigations. Some suggestions are outlined in the following. For germanium, it would be instructive to examine the efficiency of electron spin orientation as a function of excess energy, and to compare the outcome with the principal predictions for indirect optical transitions according to Cheng et al. [Che11]. In particular, transitions just above the bandgap are interesting in view of the comparatively high orientation efficiency associated with such transitions. Another intriguing question is the impact of strain on electron spin precession in the L-valleys. Such investigations might include the reverse process of what was done in electron spin resonance measurements [Hal75, and references therein]. As mentioned in the course of this thesis, the referred investigations utilised strain to lift the energy degeneracy of the L-valleys, and, as a result, to observe the tensor character of the L-valley effective Landé factor from donor-bound electrons. The obvious question in the context of magneto-optical pump-probe investigations is whether sufficient amounts of strain can be achieved to lower one valley in energy to such extent that the optically induced electrons preferably occupy this valley. With this, electron spin precession would be characterised by only one precession frequency. Besides such further investigations in germanium, a magneto-optical pump-probe analysis of carrier spin dynamics in silicon is of interest with emphasis on the coherence of optically induced electron spins. In particular, comparatively long coherence times can be expected from the rate equation model for the decay of electron spin coherence presented in this thesis, in combination with the relatively small difference in the independent elements of the Landé tensor for electrons in the fundamental conduction band minima [Wil61].

A Ohmic heating of $In_{0.53}Ga_{0.47}As$

In section 4.2.1, the temperature dependence of electron spin relaxation time and effective Landé factor around room temperature in n-type $In_{0.53}Ga_{0.47}As$ is discussed. As mentioned, the sample temperature is varied by ohmic heating. To this end, the sample is equipped with alloyed indium contacts and connected to a voltage source (Keithley 2400) via copper spring contacts. Figure A.1 shows the current-voltage characteristic. The linear fit reveals $R = 1.5\,\mathrm{k\Omega}$ for the total

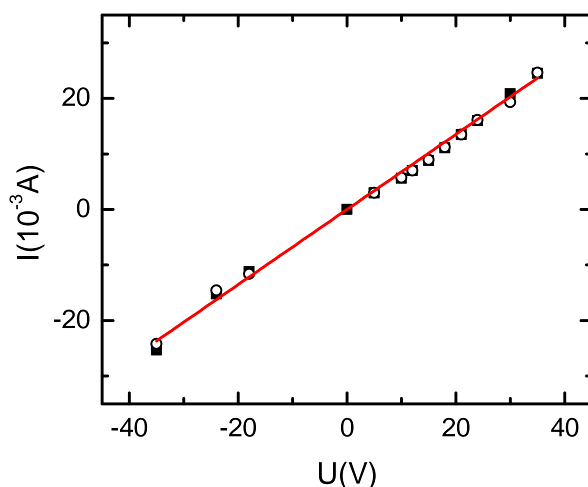

FIGURE A.1 *Current-voltage characteristic of the $In_{0.53}Ga_{0.47}As$ sample. Filled squares and open circles are recorded before and after the respective FR transient, respectively. The line is a linear fit to the data.*

resistance of the series connection of sample resistance and contact resistance. Such a value is reasonable, the sample resistance $R_S = l \times (n_H e \mu_H bd)^{-1} \sim 0.2\,\mathrm{cm} \times (2.4 \times 10^{15}\,\mathrm{cm}^{-3} \times 1.6022 \times 10^{-19}\,\mathrm{C} \times 9000\,\mathrm{cm}^2/\mathrm{Vs} \times 0.2\,\mathrm{cm} \times 3.8 \times 10^{-4}\,\mathrm{cm})^{-1} = 0.7\,\mathrm{k\Omega}$ lies in the same order of magnitude. (Note that resulting from the contact geometry both cross-section bd and length l entail fairly large uncertainties. The remaining parameters are the Hall data listed in table 4.3.) The ohmic character of the current-voltage characteristics is important, since, as a result, the sample temperature is proportional to the square of the applied voltage according to the dissipated power $P_{el} = U^2/R$. The voltage-to-temperature conversion is obtained by comparing the absorption coefficient α calculated from (i) the experimentally determined transmission through the sample and

(ii) the imaginary part of the dielectric function ε''. Approach (i) uses Lambert-Beer's law

$$U_{PD} = U_0 \exp(-\alpha d) \Leftrightarrow \alpha = -\frac{\ln(U_D/U_0)}{d}. \tag{A.1}$$

The detector voltage U_{PD} corresponds to the probe intensity that is transmitted through the sample. U_0 is the intensity of the incident probe light corrected for reflection losses at the sample surface. The detector voltage is measured for each voltage value. Specifically, $U_{PD} = 63\,\text{mV}$ at zero applied voltage. Thus, with $U_0 = 1.3\,\text{V}$, the room temperature absorption coefficient is $\alpha = 7950\,\text{cm}^{-1}$ which is close to the value in [Zie86]. The absorption coefficient is increased by $(10-15)\,\%$ for the highest voltage value of $U = 35\,\text{V}$. In approach (ii), $\alpha = \varepsilon''\omega/(nc)$ is calculated from [Yu10]

$$\varepsilon''(\omega) = 2\left(\frac{e}{m}\right)^2\left(\frac{\sqrt{2\mu}}{\hbar}\right)^3\frac{|P_{cv}|^2}{\omega^2}\sqrt{\hbar\omega - E_g}. \tag{A.2}$$

The refractive index is $n = 3.8$ [Iof] and $\hbar\omega = 0.8\,\text{eV}$ for fibre laser. From the absorption coefficient at $U = 0$ the matrix element for the optical transition $|P_{cv}|^2$ is $1\times10^{-38}\,\text{kg m V}^2$. This is reasonable compared to $|P_{cv}|^2 = 3\times10^{-38}\,\text{kg m V}^2$ for GaAs [Dum63]. $|P_{cv}|^2$ is assumed to be independent of temperature. The temperature dependence of the bandgap is according to [Vur01]. The reduced mass $\mu = (1/m_c + 1/m_v)^{-1}$ is a function of the conduction band effective mass $m_c = 0.043$ and the valence band effective mass of density of states $m_v = 0.47$ [Vur01, the specified m_v is the weighted average of the binary compounds GaAs and InAs]. Its temperature dependence presumably follows the bandgap thermal expansion (cf. section 2.1). Figure A.2 shows the resulting voltage-to-temperature conversion. For the data points, that are shown together with a parabolic

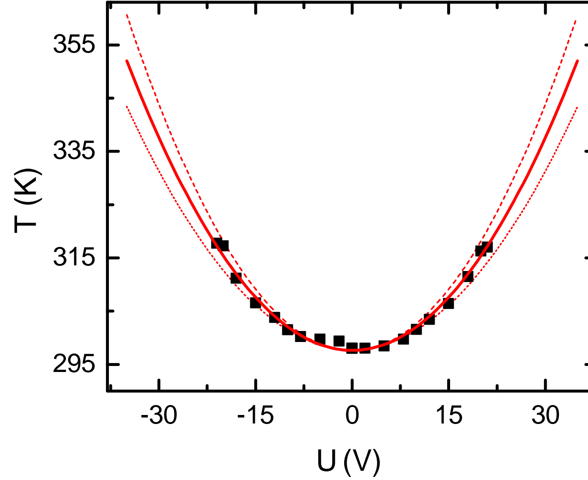

FIGURE A.2 *Voltage-to-temperature conversion according to a comparison of equations (A.1) and (A.2) for different $\mu(T)$, as detailed in the main text.*

fit (solid line), $\mu(T)$ is assumed to decrease linearly with half the gradient of the bandgap temperature characteristics. The dotted and dashed lines assume that the reduced mass does not depend

on temperature, or that $\mu(T)$ follows the overall temperature dependence of the bandgap, respectively. For the $\tau_s(T)$ and $|g^*(T)|$ in section 4.2.1 the conversion indicated by the solid line is used. The specified uncertainty ranges are determined by the dotted and dashed lines.

B Geometrical considerations on the L-valley electron g factors in germanium

Section 5.3.1 discusses the dependences of the apparent Larmor frequencies of L-valley electron spin precession on the in-plane magnetic field orientation in $\langle 100 \rangle$- and $\langle 111 \rangle$-oriented Ge. The angular dependences are evident from the following geometrical considerations. The main axes of the surfaces of constant energy are oriented along

$$\vec{e}_1 = \frac{1}{\sqrt{3}} \begin{pmatrix} 1 \\ 1 \\ 1 \end{pmatrix}; \; \vec{e}_2 = \frac{1}{\sqrt{3}} \begin{pmatrix} 1 \\ -1 \\ 1 \end{pmatrix}; \; \vec{e}_3 = \frac{1}{\sqrt{3}} \begin{pmatrix} 1 \\ 1 \\ -1 \end{pmatrix}; \; \vec{e}_4 = \frac{1}{\sqrt{3}} \begin{pmatrix} 1 \\ -1 \\ -1 \end{pmatrix} \tag{B.1}$$

and $\vec{e}_{5...8}$, that correspond to $\vec{e}_{1...4}$ except for the sign. The magnetic field is rotated within the sample plane spanned by $\vec{a}_1$ and $\vec{a}_2$, that is

$$\vec{B}(\alpha) = \vec{a}_1 \cos\alpha + \vec{a}_2 \sin\alpha. \tag{B.2}$$

The angles θ_i between the principal axes and $\vec{B}$ are defined by

$$\cos\theta_i = \vec{B}(\alpha) \cdot \vec{e}_i. \tag{B.3}$$

In the following, the calculation for $e_{\vec{1...4}}$ is shown explicitly. For symmetry reasons $e_{\vec{5...8}}$ result in the same dependences.

B.1 Surface orientation $\langle 100 \rangle$

The surface is spanned by

$$\vec{a}_1 = \frac{1}{\sqrt{2}} \begin{pmatrix} 0 \\ 1 \\ 1 \end{pmatrix}; \ \vec{a}_2 = \frac{1}{\sqrt{2}} \begin{pmatrix} 0 \\ 1 \\ -1 \end{pmatrix}.$$

With equation (B.1) to (B.3), the angles between the principal axes and the magnetic field orientation are

$$\begin{aligned}
\cos\theta_1 &= \left[\frac{1}{\sqrt{2}} \begin{pmatrix} 0 \\ 1 \\ 1 \end{pmatrix} \cos\alpha + \frac{1}{\sqrt{2}} \begin{pmatrix} 0 \\ 1 \\ -1 \end{pmatrix} \sin\alpha \right] \cdot \frac{1}{\sqrt{3}} \begin{pmatrix} 1 \\ 1 \\ 1 \end{pmatrix} = \\
&= \frac{2}{\sqrt{6}} \cos\alpha, \\
\cos\theta_2 &= \left[\frac{1}{\sqrt{2}} \begin{pmatrix} 0 \\ 1 \\ 1 \end{pmatrix} \cos\alpha + \frac{1}{\sqrt{2}} \begin{pmatrix} 0 \\ 1 \\ -1 \end{pmatrix} \sin\alpha \right] \cdot \frac{1}{\sqrt{3}} \begin{pmatrix} 1 \\ -1 \\ 1 \end{pmatrix} = \\
&= -\frac{2}{\sqrt{6}} \sin\alpha, \\
\cos\theta_3 &= \left[\frac{1}{\sqrt{2}} \begin{pmatrix} 0 \\ 1 \\ 1 \end{pmatrix} \cos\alpha + \frac{1}{\sqrt{2}} \begin{pmatrix} 0 \\ 1 \\ -1 \end{pmatrix} \sin\alpha \right] \cdot \frac{1}{\sqrt{3}} \begin{pmatrix} 1 \\ 1 \\ -1 \end{pmatrix} = \\
&= \frac{2}{\sqrt{6}} \cos\alpha = \cos\theta_1, \\
\cos\theta_4 &= \left[\frac{1}{\sqrt{2}} \begin{pmatrix} 0 \\ 1 \\ 1 \end{pmatrix} \cos\alpha + \frac{1}{\sqrt{2}} \begin{pmatrix} 0 \\ 1 \\ -1 \end{pmatrix} \sin\alpha \right] \cdot \frac{1}{\sqrt{3}} \begin{pmatrix} 1 \\ -1 \\ -1 \end{pmatrix} = \\
&= -\frac{2}{\sqrt{6}} \sin\alpha = \cos\theta_2.
\end{aligned}$$

B.2 Surface orientation $\langle 111 \rangle$

The surface is spanned by

$$\vec{a}_1 = \frac{1}{\sqrt{2}} \begin{pmatrix} 1 \\ -1 \\ 0 \end{pmatrix}; \ \vec{a}_2 = \frac{1}{\sqrt{6}} \begin{pmatrix} 1 \\ 1 \\ -2 \end{pmatrix}$$

and, according to equations (B.1) to (B.3), the θ_i are

$$\begin{aligned} \cos\theta_1 &= \left[\frac{1}{\sqrt{2}} \begin{pmatrix} 1 \\ -1 \\ 0 \end{pmatrix} \cos\alpha + \frac{1}{\sqrt{6}} \begin{pmatrix} 1 \\ 1 \\ -2 \end{pmatrix} \sin\alpha \right] \cdot \frac{1}{\sqrt{3}} \begin{pmatrix} 1 \\ 1 \\ 1 \end{pmatrix} = \\ &= 0, \end{aligned}$$

$$\begin{aligned} \cos\theta_2 &= \left[\frac{1}{\sqrt{2}} \begin{pmatrix} 1 \\ -1 \\ 0 \end{pmatrix} \cos\alpha + \frac{1}{\sqrt{6}} \begin{pmatrix} 1 \\ 1 \\ -2 \end{pmatrix} \sin\alpha \right] \cdot \frac{1}{\sqrt{3}} \begin{pmatrix} 1 \\ -1 \\ 1 \end{pmatrix} = \\ &= \frac{2}{\sqrt{6}} \cos\alpha - \frac{2}{3\sqrt{2}} \sin\alpha, \end{aligned}$$

$$\begin{aligned} \cos\theta_3 &= \left[\frac{1}{\sqrt{2}} \begin{pmatrix} 1 \\ -1 \\ 0 \end{pmatrix} \cos\alpha + \frac{1}{\sqrt{6}} \begin{pmatrix} 1 \\ 1 \\ -2 \end{pmatrix} \sin\alpha \right] \cdot \frac{1}{\sqrt{3}} \begin{pmatrix} 1 \\ 1 \\ -1 \end{pmatrix} = \\ &= \frac{4}{3\sqrt{2}} \sin\alpha, \end{aligned}$$

$$\begin{aligned} \cos\theta_4 &= \left[\frac{1}{\sqrt{2}} \begin{pmatrix} 1 \\ -1 \\ 0 \end{pmatrix} \cos\alpha + \frac{1}{\sqrt{6}} \begin{pmatrix} 1 \\ 1 \\ -2 \end{pmatrix} \sin\alpha \right] \cdot \frac{1}{\sqrt{3}} \begin{pmatrix} 1 \\ -1 \\ -1 \end{pmatrix} = \\ &= \frac{2}{\sqrt{6}} \cos\alpha + \frac{2}{3\sqrt{2}} \sin\alpha. \end{aligned}$$

Bibliography

[Agg70] R. L. Aggarwal, *Stress-modulated magnetoreflectance for the direct transitions* $\Gamma_{25'}^{3/2} \rightarrow \Gamma_{2'}$ *and* $\Gamma_{25'}^{1/2} \rightarrow \Gamma_{2'}$ *in germanium*, Phys. Rev. B **2**, 446 (1970), [DOI].

[All83] R. Allenspach, F. Meier, and D. Pescia, *Experimental symmetry analysis of electronic states by spin-dependent photoemission*, Phys. Rev. Lett. **51**, 2148 (1983), [DOI].

[Aro83] G. E. P. Aronov, A. G. and A. N. Titkov, *Spin relaxation of conduction electrons in p-type III-V compounds*, Sov. Phys. JETP **57**, 680 (1983), [Zh. Eksp. Teor. Fiz. 84, 1170 (1983)].

[Bal85] I. Balslev, *Photoluminescence of germanium near the screening ionization limit of excitons*, J. Lumin. **30**, 162 (1985), [DOI].

[Bar96] A. Baraldi, F. Colonna, C. Ghezzi, R. Magnanini, A. Parisini, L. Tarricone, A. Bosacchi, and S. Franchi, *Electron mobility and physical magnetoresistance in n-type GaSb layers grown by molecular beam epitaxy*, Semicond. Sci. Technol. **11**, 1656 (1996), [DOI].

[Bee95] J. Beerens, C. J. Miner, and N. Puetz, *Electron spin resonance in* $In_{0.53}Ga_{0.47}As$, Semicond. Sci. Technol. **10**, 1233 (1995), [DOI].

[Bir76] A. G. A. Bir, G. L. and G. E. Pikus, *Spin relaxation of electrons due to scattering by holes*, Sov. Phys. JETP **42**, 705 (1976), [Zh. Eksp. Teor. Fiz. 69, 1382 (1975)].

[Blo46] F. Bloch, *Nuclear induction*, Phys. Rev. **70**, 460 (1946), [DOI].

[Bog00] T. F. Boggess, J. T. Olesberg, C. Yu, M. E. Flatté, and W. H. Lau, *Room-temperature electron spin relaxation in bulk InAs*, Appl. Phys. Lett. **77**, 1333 (2000), [DOI].

[Bot11] F. Bottegoni, G. Isella, S. Cecchi, and F. Ciccacci, *Spin polarized photoemission from strained Ge epilayers*, Appl. Phys. Lett. **98**, 242107 (2011), [DOI].

[Bro02] F. X. Bronold, I. Martin, A. Saxena, and D. L. Smith, *Magnetic-field dependence of electron spin relaxation in n-type semiconductors*, Phys. Rev. B **66**, 233206 (2002), [DOI].

[Bro04] F. X. Bronold, A. Saxena, and D. L. Smith, *Semiclassical kinetic theory of electron spin relaxation in semiconductors*, Phys. Rev. B **70**, 245210 (2004), [DOI].

[Bur54] E. Burstein, *Anomalous optical absorption limit in InSb*, Phys. Rev. **93**, 632 (1954), [DOI].

[Cha75] J.-N. Chazalviel, *Spin relaxation of conduction electrons in highly-doped n-type germanium at low temperature*, J. Phys. Chem. Solids **36**, 387 (1975), [DOI].

[Cha06] A. N. Chantis, M. van Schilfgaarde, and T. Kotani, *Ab Initio prediction of conduction band spin splitting in zinc blende semiconductors*, Phys. Rev. Lett. **96**, 086405 (2006), [DOI].

[Che10] J. L. Cheng, M. W. Wu, and J. Fabian, *Theory of the spin relaxation of conduction electrons in silicon*, Phys. Rev. Lett. **104**, 016601 (2010), [DOI].

[Che11] J. L. Cheng, J. Rioux, J. Fabian, and J. E. Sipe, *Theory of optical spin orientation in silicon*, Phys. Rev. B **83**, 165211 (2011), [DOI].

[Chi95] V. Chin, *Electron mobility in GaSb*, Solid State Electron. **38**, 59 (1995), [DOI].

[Cho77] H. h. Chou, G. K. Wong, and B. J. Feldman, *Recombination luminescence from "hot" carriers in electron-hole droplets in stressed Ge*, Phys. Rev. Lett. **39**, 959 (1977), [DOI].

[Cro95] S. Crooker, D. Awschalom, and N. Samarth, *Time-resolved Faraday rotation spectroscopy of spin dynamics in digital magnetic heterostructures*, IEEE J. Select. Topics Quantum Electron. **1**, 1082 (1995), [DOI].

[Dar05] A. Dargys, *Hole spin relaxation: optical deformation potential scattering*, Semicond. Sci. Technol. **20**, 733 (2005), [DOI].

[Dat90] S. Datta and B. Das, *Electronic analog of the electro-optic modulator*, Appl. Phys. Lett. **56**, 665 (1990), [DOI].

[Die07] O. Dier, *Das Materialsystem (AlGaIn)(AsSb): Eigenschaften und Eignung für GaSb-basierte Vertikalresonator-Laserdioden*, Ph.D. thesis, Walter Schottky Institut der Technischen Universität München (2007).

[Du05] M.-H. Du and S. B. Zhang, *DX centers in GaAs and GaSb*, Phys. Rev. B **72**, 075210 (2005), [DOI].

[Dum63] W. P. Dumke, *Optical transitions involving impurities in semiconductors*, Phys. Rev. **132**, 1998 (1963), [DOI].

[D'y72] M. D'yakonov and V. Perel', *Spin relaxation of conduction electrons in noncentrosymmetric semiconductors*, Sov. Phys. Solid State **13**, 3023 (1972), [Fiz. Tverd. Tela 13, 3581 (1971)].

[Dzh02] R. I. Dzhioev, K. V. Kavokin, V. L. Korenev, M. V. Lazarev, B. Y. Meltser, M. N. Stepanova, B. P. Zakharchenya, D. Gammon, and D. S. Katzer, *Low-temperature spin relaxation in n-type GaAs*, Phys. Rev. B **66**, 245204 (2002), [DOI].

[Dzh04] R. I. Dzhioev, K. V. Kavokin, V. L. Korenev, M. V. Lazarev, N. K. Poletaev, B. P. Zakharchenya, E. A. Stinaff, D. Gammon, A. S. Bracker, and M. E. Ware, *Suppression of Dyakonov-Perel spin relaxation in high-mobility n-GaAs*, Phys. Rev. Lett. **93**, 216402 (2004), [DOI].

[Ehr57] H. Ehrenreich, *Electron scattering in InSb*, J. Phys. Chem. Solids **2**, 131 (1957), [DOI].

[Eic04] J. Eichler, L. Dünkel, and B. Eppich, *Die Strahlqualität von Lasern – Wie bestimmt man Beugungsmaßzahl und Strahldurchmesser in der Praxis?*, Laser Technik Journal **1**, 63 (2004), [DOI].

[Ell54] R. J. Elliott, *Theory of the effect of spin-orbit coupling on magnetic resonance in some semiconductors*, Phys. Rev. **96**, 266 (1954), [DOI].

[Ger70] E. M. Gershenzon, N. M. Pevin, and M. S. Fogelson, *Some features of ESR and spin – lattice relaxation of electrons in Ge and InSb with different donor concentrations*, Phys. Status Solidi B **38**, 865 (1970), [DOI].

[Ghe95] C. Ghezzi, R. Magnanini, A. Parisini, B. Rotelli, L. Tarricone, A. Bosacchi, and S. Franchi, *Optical absorption near the fundamental absorption edge in GaSb*, Phys. Rev. B **52**, 1463 (1995), [DOI].

[Gla04] M. M. Glazov and E. L. Ivchenko, *Effect of electron-electron interaction on spin relaxation of charge carriers in semiconductors*, J. Exp. Theor. Phys. **99**, 1279 (2004), [DOI].

[Gla12] M. M. Glazov, *Coherent spin dynamics of electrons and excitons in nanostructures*, Phys. Solid State **54**, 1 (2012), [DOI].

[Gre90] M. A. Green, *Intrinsic concentration, effective densities of states, and effective mass in silicon*, J. Appl. Phys. **67**, 2944 (1990), [DOI].

[Gre09] L. Grenet, M. Jamet, P. Noe, V. Calvo, J.-M. Hartmann, L. E. Nistor, B. Rodmacq, S. Auffret, P. Warin, and Y. Samson, *Spin injection in silicon at zero magnetic field*, Appl. Phys. Lett. **94**, 032502 (2009), [DOI].

[Gui11] C. Guite and V. Venkataraman, *Measurement of electron spin lifetime and optical orientation efficiency in germanium using electrical detection of radio frequency modulated spin polarization*, Phys. Rev. Lett. **107**, 166603 (2011), [DOI].

[Hal75] E. B. Hale, J. R. Dennis, and S.-H. Pan, *Strain effects on the ESR spectrum from antimony donors in germanium*, Phys. Rev. B **12**, 2553 (1975), [DOI].

[Hal99] K. C. Hall, S. W. Leonard, H. M. van Driel, A. R. Kost, E. Selvig, and D. H. Chow, *Subpicosecond spin relaxation in GaAsSb multiple quantum wells*, Appl. Phys. Lett. **75**, 3665 (1999), [DOI].

[Has60] H. Hasegawa, *Spin-lattice relaxation of shallow donor states in Ge and Si through a direct phonon process*, Phys. Rev. **118**, 1523 (1960), [DOI].

[Hau09] C. Hautmann, F. Jaworeck, K. Kashani-Shirazi, M.-C. Amann, and M. Betz, *Temperature and doping dependence of electron spin relaxation in GaSb*, Semicond. Sci. Technol. **24**, 025018 (2009), [DOI].

[Hau11] C. Hautmann, B. Surrer, and M. Betz, *Ultrafast optical orientation and coherent Larmor precession of electron and hole spins in bulk germanium*, Phys. Rev. B **83**, 161203 (2011), [DOI].

[Hau12] C. Hautmann and M. Betz, *Magneto-optical analysis of the effective g tensor and electron spin decoherence in the multivalley conduction band of bulk germanium*, Phys. Rev. B **85**, 121203 (2012), [DOI].

[Hay08] S. E. Hayes, S. Mui, and K. Ramaswamy, *Optically pumped nuclear magnetic resonance of semiconductors*, J. Chem. Phys. **128**, 052203 (2008), [DOI].

[Hen68] J. C. Hensel, *Microwave combined resonances in germanium: g factor of the free hole*, Phys. Rev. Lett. **21**, 983 (1968), [DOI].

[Her71] C. Hermann and G. Lampel, *Measurement of the g factor of conduction electrons by optical detection of spin resonance in p-type semiconductors*, Phys. Rev. Lett. **27**, 373 (1971), [DOI].

[Her77] C. Hermann and C. Weisbuch, *$k \cdot p$ perturbation theory in III-V compounds and alloys: a reexamination*, Phys. Rev. B **15**, 823 (1977), [DOI].

[Hil02] D. J. Hilton and C. L. Tang, *Optical orientation and femtosecond relaxation of spin-polarized holes in GaAs*, Phys. Rev. Lett. **89**, 146601 (2002), [DOI].

[Hoh06] P. E. Hohage, G. Bacher, D. Reuter, and A. D. Wieck, *Coherent spin oscillations in bulk GaAs at room temperature*, Appl. Phys. Lett. **89**, 231101 (2006), [DOI].

[Hu01] X. Hu, R. de Sousa, and S. D. Sarma, *Decoherence and dephasing in spin-based solid state quantum computers* (2001), http://arxiv.org/abs/cond-mat/0108339v2.

[Hu04] W. Hu, Z. Wang, B. Su, Y. Dai, S. Wang, and Y. Zhao, *Gallium antisite defect and residual acceptors in undoped GaSb*, Phys. Lett. A **332**, 286 (2004), [DOI].

[Hüb09] J. Hübner, S. Döhrmann, D. Hägele, and M. Oestreich, *Temperature-dependent electron Landé g factor and the interband matrix element of GaAs*, Phys. Rev. B **79**, 193307 (2009), [DOI].

[Iof] Ioffe Physico-Technical Institute, *Electronic archive – New semiconductor materials. Characteristics and properties*, http://www.ioffe.ru/SVA/NSM/ (called 2012).

[Ivc73] E. Ivchenko, *Spin relaxation of free carriers in a noncentrosymmetric semiconductor in a longitudinal magnetic field*, Sov. Phys. Solid State **15**, 1048 (1973).

[Jia09a] J. H. Jiang and M. W. Wu, *Comment on 'Density dependence of electron-spin polarization and relaxation in intrinsic GaAs at room temperature'*, J. Phys. D: Appl. Phys. **42**, 238001 (2009), [DOI].

[Jia09b] J. H. Jiang and M. W. Wu, *Electron-spin relaxation in bulk III-V semiconductors from a fully microscopic kinetic spin Bloch equation approach*, Phys. Rev. B **79**, 125206 (2009), [DOI].

[Jon07] B. T. Jonker, G. Kioseoglou, A. T. Hanbicki, C. H. Li, and P. E. Thompson, *Electrical spin-injection into silicon from a ferromagnetic metal/tunnel barrier contact*, Nat. Phys. **3**, 542 (2007), [DOI].

[Kav01] K. V. Kavokin, *Anisotropic exchange interaction of localized conduction-band electrons in semiconductors*, Phys. Rev. B **64**, 075305 (2001), [DOI].

[Kik98] J. Kikkawa and D. Awschalom, *Resonant spin amplification in n-type GaAs*, Phys. Rev. Lett. **80**, 4313 (1998), [DOI].

[Kop04] K. Kopitzki, *Einführung in die Festkörperphysik* (2004), ISBN 9783519430834.

[Kow96] B. Kowalski, P. Omling, B. K. Meyer, D. M. Hofmann, V. Härle, F. Scholz, and P. Sobkowicz, *Optically detected spin resonance of conduction band electrons in InGaAs/InP quantum wells*, Semicond. Sci. Technol. **11**, 1416 (1996), [DOI].

[Kra08] M. Krauß, M. Aeschlimann, and H. C. Schneider, *Ultrafast spin dynamics including spin-orbit interaction in semiconductors*, Phys. Rev. Lett. **100**, 256601 (2008), [DOI].

[Kra10] M. Krauß, H. C. Schneider, R. Bratschitsch, Z. Chen, and S. T. Cundiff, *Ultrafast spin dynamics in optically excited bulk GaAs at low temperatures*, Phys. Rev. B **81**, 035213 (2010), [DOI].

[Lam68] G. Lampel, *Nuclear dynamic polarization by optical electronic saturation and optical pumping in semiconductors*, Phys. Rev. Lett. **20**, 491 (1968), [DOI].

[Lau87] P. Lautenschlager, M. Garriga, S. Logothetidis, and M. Cardona, *Interband critical points of GaAs and their temperature dependence*, Phys. Rev. B **35**, 9174 (1987), [DOI].

[Li10] P. Li and H. Dery, *Theory of spin-dependent phonon-assisted optical transitions in silicon*, Phys. Rev. Lett. **105**, 037204 (2010), [DOI].

[Lit06] K. L. Litvinenko, B. N. Murdin, J. Allam, C. R. Pidgeon, T. Zhang, J. J. Harris, L. F. Cohen, D. A. Eustace, and D. W. McComb, *Spin lifetime in InAs epitaxial layers grown on GaAs*, Phys. Rev. B **74**, 075331 (2006), [DOI].

[Lit07] K. L. Litvinenko, L. Nikzad, J. Allam, B. N. Murdin, C. R. Pidgeon, J. J. Harris, T. Zhang, and L. F. Cohen, *Spin lifetime in high quality InSb epitaxial layers grown on GaAs*, J. Appl. Phys. **101**, 083105 (2007), [DOI].

[Lit10] K. L. Litvinenko, M. A. Leontiadou, J. Li, S. K. Clowes, M. T. Emeny, T. Ashley, C. R. Pidgeon, L. F. Cohen, and B. N. Murdin, *Strong dependence of spin dynamics on the orientation of an external magnetic field for InSb and InAs*, Appl. Phys. Lett. **96**, 111107 (2010), [DOI].

[Lor09] E. J. Loren, B. A. Ruzicka, L. K. Werake, H. Zhao, H. M. van Driel, and A. L. Smirl, *Optical injection and detection of ballistic pure spin currents in Ge*, Appl. Phys. Lett. **95**, 092107 (2009), [DOI].

[Lor11] E. J. Loren, J. Rioux, C. Lange, J. E. Sipe, H. M. van Driel, and A. L. Smirl, *Hole spin relaxation and intervalley electron scattering in germanium*, Phys. Rev. B **84**, 214307 (2011), [DOI].

[Lut55] J. M. Luttinger and W. Kohn, *Motion of electrons and holes in perturbed periodic fields*, Phys. Rev. **97**, 869 (1955), [DOI].

[Mac57] G. G. Macfarlane, T. P. McLean, J. E. Quarrington, and V. Roberts, *Fine structure in the absorption-edge spectrum of Ge*, Phys. Rev. **108**, 1377 (1957), [DOI].

[Mar83] M. N. S. Marushchak, V. A. and A. N. Titkov, *Spin relaxation of conduction electrons in moderately doped gallium arsenide crystals*, Sov. Phys. Solid State **25**, 2035 (1983), [Fiz. Tverd. Tela 25, 3537 (1983)].

[Mas64] W. P. Mason and T. B. Bateman, *Ultrasonic wave propagation in doped n-germanium and p-silicon*, Phys. Rev. **134**, A1387 (1964), [DOI].

[Mei84] F. Meier and B. P. Zakharchenya (editors), *Optical Orientation (Modern Problems in Condensed Matter Sciences)*, Elsevier Science Ltd (1984), ISBN 9780444867414.

[Mos58] T. S. Moss and T. D. H. Hawkins, *The infra-red emissivities of indium antimonide and germanium*, Proc. Phys. Soc. **72**, 270 (1958), [DOI].

[Nak99] H. Nakata, N. Shimizu, T. Ohyama, Y. Nonogaki, Y. Fujiwara, and Y. Takeda, *Optically detected far-infrared magnetoabsorption in InGaAs*, Jpn. J. Appl. Phys. **38**, 1868 (1999), [DOI].

[Nas07] F. Nastos, J. Rioux, M. Strimas-Mackey, B. S. Mendoza, and J. E. Sipe, *Full band structure LDA and* $k \cdot p$ *calculations of optical spin-injection*, Phys. Rev. B **76**, 205113 (2007), [DOI].

[Nil73] N. G. Nilsson, *An accurate approximation of the generalized Einstein relation for degenerate semiconductors*, Phys. Status Solidi A **19**, K75 (1973), [DOI].

[Odo06] B. Odom, D. Hanneke, B. D'Urso, and G. Gabrielse, *New measurement of the electron magnetic moment using a one-electron quantum cyclotron*, Phys. Rev. Lett. **97**, 030801 (2006), [DOI].

[Oer08] S. Oertel, J. Hubner, and M. Oestreich, *High temperature electron spin relaxation in bulk GaAs*, Appl. Phys. Lett. **93**, 132112 (2008), [DOI].

[Oes95] M. Oestreich and W. W. Rühle, *Temperature dependence of the electron Landé g factor in GaAs*, Phys. Rev. Lett. **74**, 2315 (1995), [DOI].

[Oes96] M. Oestreich, S. Hallstein, A. P. Heberle, K. Eberl, E. Bauser, and W. W. Rühle, *Temperature and density dependence of the electron Landé g factor in semiconductors*, Phys. Rev. B **53**, 7911 (1996), [DOI].

[Oli81] J. D. Oliver Jr., L. F. Eastman, P. D. Kirchner, and W. J. Schaff, *Electrical characterization and alloy scattering measurements of LPE* $Ga_xIn_{1-x}As/InP$ *for high frequency device applications*, J. Cryst. Growth **54**, 64 (1981), [DOI].

[Pai89] A. Pais, *George Uhlenbeck and the discovery of electron spin*, Phys. Today **42**, 34 (1989), [DOI].

[Pet58] R. Petritz, *Theory of an experiment for measuring the mobility and density of carriers in the space-charge region of a semiconductor surface*, Phys. Rev. **110**, 1254 (1958), [DOI].

[Pon66] R. E. Pontinen and T. M. Sanders, *Electron-spin-resonance experiments on antimony-doped germanium*, Phys. Rev. **152**, 850 (1966), [DOI].

[Poo90] I. Poole, M. E. Lee, I. R. Cleverley, A. R. Peaker, and K. E. Singer, *Deep donors in GaSb grown by molecular beam epitaxy*, Appl. Phys. Lett. **57**, 1645 (1990), [DOI].

[Rio10] J. Rioux and J. E. Sipe, *Optical injection and control in germanium: Thirty-band* $k \cdot p$ *theory*, Phys. Rev. B **81**, 155215 (2010), [DOI].

[Ros88] H. Roskos, B. Rieck, A. Seilmeier, and W. Kaiser, *Cooling of a carrier plasma in germanium investigated with subpicosecond infrared pulses*, Applied Physics Letters **53**, 2406 (1988), [DOI].

[Rot59] L. M. Roth and B. Lax, *g factor of electrons in germanium*, Phys. Rev. Lett. **3**, 217 (1959), [DOI].

[Rot60] L. M. Roth, *g factor and donor spin-lattice relaxation for electrons in germanium and silicon*, Phys. Rev. **118**, 1534 (1960), [DOI].

[Rou06] F. Roux, G. Lampel, Y. Lassailly, and J. Peretti, *Polarized luminescence in silicon*, in *Bulletin of the American Physical Society* (2006), http://meetings.aps.org/link/BAPS.2006.MAR.V20.12.

[Sch95] R. Scholz, *Hole–phonon scattering rates in gallium arsenide*, Journal of Applied Physics **77**, 3219 (1995), [DOI].

[Sei69] R. Seisyan, A. Varfolomeev, and B. P. Zakharchenya, Sov. Phys. Semicond. **2**, 1069 (1969), [Fiz. Tekh. Poluprov. 2, 1276 (1968)].

[Sha89] J. Shah, *Ultrafast studies of carrier relaxation in semiconductors and their microstructures*, Superlattices Microstruct. **6**, 293 (1989), [DOI].

[She09] K. Shen, *A peak in density dependence of electron spin relaxation time in n-type bulk GaAs in metallic regime*, Chin. Phys. Lett. **26**, 067201 (2009), [DOI].

[She10] K. Shen and M. W. Wu, *Hole spin relaxation in intrinsic and p-type bulk GaAs*, Phys. Rev. B **82**, 115205 (2010), [DOI].

[Son02] P. H. Song and K. W. Kim, *Spin relaxation of conduction electrons in bulk III-V semiconductors*, Phys. Rev. B **66**, 035207 (2002), [DOI].

[Spi00] J. Spieler, T. Kippenberg, J. Krauss, P. Kiesel, G. H. Dohler, P. Velling, W. Prost, and F. J. Tegude, *Electro-optical examination of the band structure of ordered InGaAs*, Appl. Phys. Lett. **76**, 88 (2000), [DOI].

[Sug00] Sugano, *Magneto-Optics (Springer Series in Solid-State Sciences)*, Springer, 1st edition (2000), ISBN 9783540659617.

[Ten09] L. H. Teng, K. Chen, J. H. Wen, W. Z. Lin, and T. S. Lai, *Density dependence of electron-spin polarization and relaxation in intrinsic GaAs at room temperature*, J. Phys. D: Appl. Phys. **42**, 135111 (2009), [DOI].

[VdP58] L. J. Van der Pauw, *A method of measuring specific resistivity and Hall effect of discs of arbitrary shape*, Philips. Res. Rep. (1958).

[Vur01] I. Vurgaftman, J. R. Meyer, and L. R. Ram-Mohan, *Band parameters for III-V compound semiconductors and their alloys*, J. Appl. Phys. **89**, 5815 (2001), [DOI].

[Wei59] G. Weinreich, T. M. Sanders, and H. G. White, *Acoustoelectric effect in n-type germanium*, Phys. Rev. **114**, 33 (1959), [DOI].

[Wes07] M. Wesseli and M. Betz, *Analyzing nonequilibrium carrier distributions with spectrally resolved femtosecond Faraday rotation*, Phys. Rev. B **76**, 073201 (2007), [DOI].

[Wil61] D. K. Wilson and G. Feher, *Electron spin resonance experiments on donors in silicon. iii. Investigation of excited states by the application of uniaxial stress and their importance in relaxation processes*, Phys. Rev. **124**, 1068 (1961), [DOI].

[Wil64] D. K. Wilson, *Electron spin resonance experiments on shallow donors in germanium*, Phys. Rev. **134**, A265 (1964), [DOI].

[Wil07] Z. Wilamowski, H. Malissa, F. Schäffler, and W. Jantsch, *g-factor tuning and manipulation of spins by an electric current*, Phys. Rev. Lett. **98**, 187203 (2007), [DOI].

[Win04] R. Winkler and M. Oestreich, *Spinelektronik*, Physik Journal **3**, 39 (2004).

[Wol01] S. A. Wolf, D. D. Awschalom, R. A. Buhrman, J. M. Daughton, S. von Molnár, M. L. Roukes, A. Y. Chtchelkanova, and D. M. Treger, *Spintronics: A spin-based electronics vision for the future*, Science **294**, 1488 (2001), [DOI].

[Wu10] M. Wu, J. Jiang, and M. Weng, *Spin dynamics in semiconductors*, Phys. Rep. **493**, 61 (2010), [DOI].

[Yaf63] Y. Yafet, *g factors and spin-lattice relaxation of conduction electrons*, Solid State Phys. **14**, 1 (1963), [DOI].

[Yu05] Z. G. Yu, S. Krishnamurthy, M. van Schilfgaarde, and N. Newman, *Spin relaxation of electrons and holes in zinc-blende semiconductors*, Phys. Rev. B **71**, 245312 (2005), [DOI].

[Yu10] P. Y. Yu and M. Cardona, *Fundamentals of Semiconductors: Physics and Materials Properties (Graduate Texts in Physics)*, Springer, 4th edition (2010), ISBN 9783642007095.

[Zaw08] W. Zawadzki, P. Pfeffer, R. Bratschitsch, Z. Chen, S. T. Cundiff, B. N. Murdin, and C. R. Pidgeon, *Temperature dependence of the electron spin g factor in GaAs*, Phys. Rev. B **78**, 245203 (2008), [DOI].

[Zho11] Y. Zhou, W. Han, L.-T. Chang, F. Xiu, M. Wang, M. Oehme, I. A. Fischer, J. Schulze, R. K. Kawakami, and K. L. Wang, *Electrical spin injection and transport in germanium*, Phys. Rev. B **84**, 125323 (2011), [DOI].

[Zie86] E. Zielinski, H. Schweizer, K. Streubel, H. Eisele, and G. Weimann, *Excitonic transitions and exciton damping processes in InGaAs/InP*, J. Appl. Phys. **59**, 2196 (1986), [DOI].

[Žut04] I. Žutić and S. D. Sarma, *Spintronics: Fundamentals and applications*, Rev. Mod. Phys. **76**, 323 (2004), [DOI].

Acknowledgements

At this point I would like to thank all the people without whom this work would not have been possible. I am especially grateful to:

Prof. Dr. Dr. h.c. Alfred Laubereau for the opportunity to conduct my PhD studies at his chair at the Technical University Munich, and for his interest in the progress of my work.

Prof. Dr. Markus Betz, first, for the possibility to continue my studies in his group at the Technical University Dortmund. Furthermore, I would like to thank him for exceptional support, constructive and enriching discussions, and for continuously bringing up future prospects throughout my time as a PhD student.

Prof. Dr. Manfred Bayer, **Prof. Dr. Dmitri Yakovlev** and **Dr. Ilya Akimov** for their interest in my research, and for the loan of magnets and cryostats.

Dr. Claudia Ruppert for introducing me to ultrafast spectroscopy, as well as her, **Dr. Markus Zecherle**, **Sebastian Thunich** and **Elmar Sternemann** for the friendly collaboration and constant readiness to discuss arising questions.

Florian Jaworeck and **Bernhard Surrer** for the successful and enjoyable collaboration during their diploma theses.

All members of Prof. Laubereau's group and the groups of Prof. Betz and Prof. Bayer, besides those already mentioned above especially **Dr. Hristo Iglev**, **Dr. Mart Fischer**, **Dr. Jasper Werhahn**, **Hubert Rossmadl**, **Jan Lohrenz** and **Thorben Jostmeier**, for the productive and pleasant working atmosphere.

Prof. Dr. Markus-Christian Amann and **Kaveh Kashani-Shirazi** (†) for the constructive cooperation within the GaSb project, and for provision of samples.

Prof. Dr. Martin Brandt, **Dr. Sebastian Gönnenwein**, **Dr. Hans Hübl** and the other core attendees of the "Walt(h)er Seminar", as well as **Prof. Dr. Dominique Bougeard** and **Dr. Narayan Sircar** for comprehensive discussions. Additionally, Dr. Sebastian Gönnenwein for the loan of the electromagnet and Dr. Narayan Sircar for the supply with germanium wafers.

Wolfgang Dürichen and **Lukas Loidl** for providing prompt and reliable solutions for numerous mechanical problems, **Klaus Wiegers**, **Thomas Stöhr** and **Lars Wieschollek** for excellent technical assistance, **Viktoria Blaschek** and **Michaela Wäscher** for competent support in organisational matters, and all of them for the good time.

Finally, warm thanks goes to my parents **Marianne** and **Edmund** and my sister **Veronika** for their loving support. And last, but not least, to **Matthias**.